Institute for Automation

Department Product Engineering,

Montanuniversität Leoben

Automation and Evaluation of Flash-Thermographic Inspections

MASTER THESIS

Thomas Grandl

Field of Study:
Mechanical Engineering

Supervisors:

PRIV.-DOZ. DR.TECHN. BEATA OSWALD-TRANTA
O.UNIV.-PROF. DIPL.-ING. DR.TECHN. PAUL O'LEARY

March 2017

Institute for Automation
Department Product Engineering
Montanuniversität Leoben
Peter-Tunner Straße 25
8700 Leoben
Austria

W: automation.unileoben.ac.at
E: automation@unileoben.ac.at
T: +43(0)3842/402-5301
F: +43(0)3842/402-5302

Last compiled on Mon 13$^{\text{th}}$ Mar, 2017.
This thesis was typeset using LaTeX.
TeX is a trademark of the American Mathematical Society.

Affidavit

I declare in lieu of oath, that I wrote this thesis and performed the associated research myself, using only literature cited in this volume.

Eidesstattliche Erklärung

Ich erkläre an Eides statt, dass ich diese Arbeit selbstständig verfasst, andere als die angegebenen Quellen und Hilfsmittel nicht benutzt und mich auch sonst keiner unerlaubten Hilfsmittel bedient habe.

Leoben, Mon 13th Mar, 2017   Thomas Grandl

Acknowledgments

I want to thank all the people who accompanied and supported me during my studies. I want to express my special thanks to some of them:

First I want to thank my family, my mother Maria and my father Leopold, who encouraged and enabled me to do this studies. Without their support, both emotional and financial, I would not have been able to master this challenge.

I also want to thank all my colleagues and friends here in Leoben for the shared time, both for the purpose of learning and for the leisure spent together.

Special thanks to my colleagues at the Institute for Automation. I want to thank Roland Schmidt, who helped me to find my way into the field of thermography, Gerold Probst, who supported me in all technical challenges during my research, Paul O'Leary, who helped me to overcome the difficulties in the field of mathematics, and of course my supervisor Beata Oswald-Tranta, who supported me in the best way she could in the course of this work.

Finally, I want to express my special gratitude to Ulrike, who assisted me in difficult hours and who always supported me with all her strength.

Abstract

This thesis addresses the design, construction and software implementation of an active flash thermographic test rig. Thermography belongs to the class of non-destructive material testing methods.

The aim of this work is to implement a flexible test rig which simplifies flash thermographic tests on specific test objectives. This includes the acquisition of a time-series of images during a flash-thermographic process, as well as the analysis of the data image using predefined evaluation methods. To this end a series of standard thermographic computational procedures are implemented and where required extended. The results of these computations are compared for different reference specimens.

Furthermore, functions have been developed which enable the software to automatically detect defects in a specimen in qualitative and quantitative manner. The software therefore applies different image processing techniques on the results of the evaluation methods. This shall be seen as preparation for an automatic and autonomous operation in industrial applications.

IV

Kurzfassung

Diese Arbeit umfasst die Entwicklung, Konstruktion und Softwareimplementierung eines Versuchsstandes zur Durchführung von Blitz-Thermographischen Prüfungen. Die Thermographie ist ein zerstörungsfreies Materialprüfverfahren.

Ziel dieser Arbeit ist die Implementierung eines flexibel einsetzbaren Prüfstands, welcher die Durchführung von Blitz-Thermographischen Prüfungen ermöglicht. Dies umfasst sowohl die Erfassung einer Zeitfolge von Bilddaten im Zuge einer Messung, als auch die Auswertung dieser Bilddaten mit Hilfe von vordefinierten Auswertemethoden. Zu diesem Zweck wurde eine Reihe von Standardverfahren zur Evaluierung von thermographischen Prozessen implementiert und wo notwendig erweitert. Die Ergebnisse solcher Auswertungen von verschiedenen Testkörpern werden miteinander verglichen.

Außerdem wurden Funktionen entwickelt, welche die Software in die Lage versetzen automatisch Fehler in Testkörpern zu bestimmen, sowohl in qualitativer als auch quantitativer Hinsicht. Dazu werden verschiedene Bildverarbeitungstechniken auf die Ergebnisse der Auswertungsmethoden angewandt. Dieser Schritt soll als Vorbereitung eines automatischen und autonomen Betriebs in Industrieanlagen verstanden werden.

Schlagwörter

Contents

1 Introduction

1.1 Thermography

Thermography is a non-destructive material testing method. It uses infrared (IR) cameras to record IR-radiation emitted by originally warm (passive thermography) or artificially heated (active thermography) materials. The recorded data is then processed by a software which uses predefined physical models with analytical equations to determine defects in the tested material. This defect determination can be in a qualitative and/or quantitative way, depending on the specific evaluation method.

Compared to other non-destructive testing methods, the (active) thermography offers some significant advantages. During the testing process no direct contact to the material is required. Also, those processes are completed within very short time intervals (compared to other non-destructive testing methods) since they consist of a usually short heating period and a similar short data computation. In case of successive tests on a test rig, the only handling activities required from an external operator is to exchange the test materials (which is a big advantage compared to e.g. magnetic particle inspection). When thinking of a production line, this testing method can easily be integrated into such a line. Furthermore, the energy which is inserted into the test material is very low and therefore does not increase the material temperature much (often not more than some °C). The material is therefore barely affected by the testing method, compared to other testing methods which use chemicals on the surface of the material or influence it in another kind of way.

All those characteristics make the thermography suitable for industrial usage. The low necessity of human handling operations and the computational evaluation make this testing method predestined for automation. The goal is to develop test rigs which operate fully automatic and autonomous and can be integrated in production lines. Furthermore, the results of these methods are very often representable as images. Thus, even when human examination and decisions are essential, operators are highly supported by the results gained from the automated tests.

1.2 Application for Thermography: CFRP Testing

Carbon Fiber Reinforced Plastics - CFRP - consist of carbon fibers which are embedded into a plastic (or resin, respectively) matrix [22]. The fibers exhibit high stability and carry the load. The matrix can be either thermoset or thermoplast, fixes the fibers in their position and protects them from environmental damage [22].

CFRP materials exhibit high stability at low density, high corrosion resistance, fatigue limit and ability to absorb energy. Those properties (especially the high stability at low density) make them very suitable for applications in aerospace and space industry. The automotive industry uses those materials in increasing quantities [22].

Possible types of defects in CFRPs are delaminations within the material or impact damages. The purpose of this thesis is to investigate the ability of (active) thermographic inspections to detect such defects.

1.3 Outline of this Thesis

First, different non-destructive testing methods and the physical principles which thermography relies on are described in chapter "Basic Principles". Chapter "Experimental Rig" presents the rig and the testing software that have been developed, built and programmed during this thesis. The chapter "Evaluation Methods" explains the mathematical principles which are used to evaluate the recorded data according to the different thermographical methods. Chapter "Data Processing" presents the implementation of the evaluation methods in the software and describes the problems that occurred and their solutions. The "Image Processing" part examines the possibilities to automatically determine defects in the specimens on the basis of resulting data gathered during the data processing step. To demonstrate the developed procedures a number of different samples have been tested and the results are described in chapter "Examples". Finally, chapter "Discussion" summarizes the results and adds an outlook on potentials and possible future developments of the thermography.

2 Basic Principles

2.1 Similar Nondestructive Material Tests

2.1.1 Ultrasonic Material Testing

Sound waves which exhibit a frequency of more than 20kHz are referred to as ultrasonic (US) sound [17]. The border between sound and ultrasonic sound is derived from the maximum frequency a human ear can process. For ultrasonic material testing such high frequencies are desirable since at these high frequencies the sound dispersion within a material does not depend on the geometry of the material.

If the structure of a material is thought of as a matrix of small particles, an ultrasonic wave which travels through this material can be illustrated as compression and elongation of the distances between those particles [17], see figure 2.1.
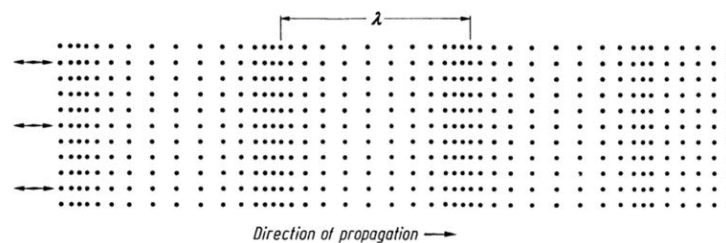
Figure 2.1: Illustration of an ultrasonic wave travelling through a material [17]

In this figure the illustrated wave moves from the left side to the right side due to an excitation on the left side. λ represents the wavelength of this wave. Note that this illustration represents a longitudinal wave, which means that the dispersion direction of the wave is parallel to the direction of elongation and compression. Waves where the directions of those two movements are orthogonal to each other are called transversal waves [17]. However, the principles and processes of the applied testing methods are further described on the example of the longitudinal wave.

When such a wave reaches the rear side of the material or an obstacle (such as a defect like an air pocket) the wave is reflected [17]. When the reflected wave reaches the front surface again it can be detected by appropriate sensors, which generate an electrical signal as an

output. This signal can be processed further using signal processing devices.

Possibilities to detect defects in materials are transit-time methods [17]. One of those methods measures the transit time of a wave through the material and back. A thin specimen will yield a shorter transit time than a thick specimen. Therefore, the transit time above the location of a defect (e.g. an air pocket) within a specimen will show a shorter transit time than the flawless material around the defect. Furthermore, the material parameters can be used to compute the depth of this defect.

To receive appropriate signals a high quality coupling between US-transmitter/US-receiver and the surface of the specimen must be ensured. Therefore, the surface conditions of materials highly affect the US measurements. To increase the quality of the coupling, using a liquid coupling medium between surface and transmitter/receiver is common practice.

The transmitter and receiver usually consist of piezo electric elements. Those elements flex when electrical voltage is applied [16]. Thus, they are able to generate a sonic signal through movement. Since this process is reversible [16], such a piezo electric element can also transform sonic signals into electrical signals and is therefore applicable as receiver as well.

2.1.2 Radiography Testing

Radiography testing is an imaging testing method where a specimen is placed between a radiation source and a detector [11]. The type of radiation can be X-ray or gamma-ray, corresponding to the radiation source. The type of detection mechanism can be a film, Real Time Radiography (RTR), Computed Tomography (CT), Digital Radiography (DR) or Computed Radiography (CR) [11].

The concept of this testing method is that different thicknesses or densities within a specimen will yield different absorption rates of the radiation [29]. The differences in intensity at the rear side of the specimen can be detected and recorded, compare the illustration in figure 2.2.

"Radiographic testing is used extensively on castings and weldments. Radiography is well suited to the testing of semiconductor devices for cracks, broken wires, unsoldered connections, foreign material and misplaced components" [29].

2.1.3 Comparison of Different Testing Methods

Compared to ultrasonic testing, thermography is an imaging method. That means that the output can directly be presented as image (which also applies to radiography), which is very suitable as a support for human judgement. In addition, while ultrasonic testing requires a "scanning" of the specimen surface, thermography investigates the whole specimen at once,
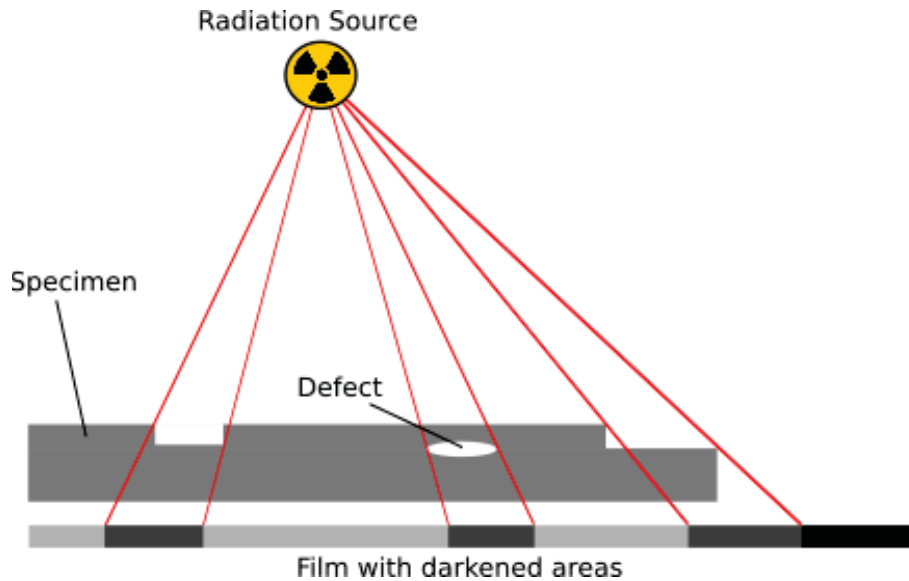
Figure 2.2: Illustration of radiography using a film

which reduces the testing effort and time.

Radiography and thermography are both imaging testing methods and both are automatable, but radiography is very expensive [29]. Furthermore, radiography requires high quality radiation shields and, in case of gamma-rays, the handling of the radiation generator is complex because of the necessity of shielding all the time (even if the device is inactive). A main drawback of radiography, compared to thermography, is the disability to detect delaminations in specimens, because of the small difference in radiation absorption between delaminated and laminated material [29].

2.2 Heat Conduction

There are three different types of heat transfer:

- heat conduction

- infrared radiation

- heat convection

Infrared radiation is described in more detail in the next section. Heat conduction is an important phenomenon in terms of the measurements presented in this work and shall be described more closely in this section. Heat convection has no significance regarding this thesis and is therefore not further discussed.

Heat conduction occurs within a solid material. Energy is transported through this material via thrusts between molecules [13]. Such transport requires differences in molecule

energy and hence a temperature gradient within the material. The heat conduction due to a temperature gradient will balance this gradient until an equilibrium is reached and the heat conduction stops. Such progress is called "non-steady" [13] or "transient". Stationary states of temperature distribution and gradient require an external heat source or heat sink. The problems which are dealt with in this thesis are transient.

A major parameter regarding heat conduction is the thermal conductivity which depends on the material properties. This quantity represents the power, which is transmitted through the material, with respect to the temperature gradient. The transmitted power can be described using the equation [13]

$$P = A\lambda\frac{T_1 - T_2}{l} \tag{2.1}$$

where

$$A \dots \text{cross section through which the heat is transfered}$$
$$\lambda \dots \text{thermal conductivity}$$
$$T_1, T_2 \dots \text{temperatures at different locations within the material}$$
$$l \dots \text{distance between the locations of temperatures } T_1 \text{ and } T_2$$

The unit of the thermal conductivity is $[W/(Km)]$. Note that the thermal conductivity also depends on the temperature of the material (Note also: this is not the same as the dependency of the transmitted power on the temperature gradient!). A selection of materials with their thermal conductivity at certain temperatures is presented in table 2.1.

Material	Temperature [°C]	λ [W/(Km)]
Copper	50	420
Aluminum	100	230
Lead	0	36
Quartz glass	50	1.4

Table 2.1: Thermal conductivity values for a selection of materials [13]

The thermal conductivity is related to another important property in terms of heat conduction: The thermal diffusivity. The relationship between those two quantities is given as [13]

$$\alpha = \frac{\lambda}{\rho c} \tag{2.2}$$

where

$$\alpha \ldots \text{thermal diffusivity}$$
$$\rho \ldots \text{material density}$$
$$c \ldots \text{specific heat capacity}$$

The unit of the thermal diffusivity is $[m^2/s]$. Table 2.2 provides an overview of thermal diffusivity values for a selection of materials which are used in the examples of this thesis.

Category	Material	$\rho \ [kg/m^3]$	$c \ [J/kgK]$	$\lambda \ [W/(Km)]$	$\alpha \ [m^2/s]$
	1.2842	7850	460	30	$8.3079 \cdot 10^{-6}$
	1.2210	7800	460	32	$8.9186 \cdot 10^{-6}$
Steel [12]	1.2550	8000	460	25	$6.7935 \cdot 10^{-6}$
	1.2101	7700	460	30	$8.4698 \cdot 10^{-6}$
	1.2343	7800	460	32.1	$8.9465 \cdot 10^{-6}$
	977-2 PW d33	-	-	-	$0.2 \cdot 10^{-6}$
CFRP [33]	977-2 UD d33	-	-	-	$0.24 \cdot 10^{-6}$
	5320 8HS d33	-	-	-	$0.32 \cdot 10^{-6}$
	yellow	-	-	-	$0.170 \cdot 10^{-6}$
PLA [20]	green	-	-	-	$0.141 \cdot 10^{-6}$
	black	-	-	-	$0.072 \cdot 10^{-6}$

Table 2.2: Thermal diffusivity values for a selection of materials [12, 20, 33]

2.3 Infrared Radiation

This section is based on and structured in the style of [34] with the content of [2] and [8].

The electromagnetic spectrum of radiation reaches from a wave length of less than $10^{-14}m$ up to a wave length of more than 10^6m, [2]. Table 2.3 provides an overview about the classifications of the spectrum according to [8].

The spectrum visible to the human eye (visible light) reaches from a wave length of $380nm$ (violet) up to a wave length of $780nm$ (red). The infrared spectrum starts above the spectrum of visible light and reaches from about $780nm$ up to about $1000\mu m$.

The spectral intensity density of a black body (described subsequently) depends on the wavelength of the radiation and the temperature of the surface. This relationship can be described with Planck's radiation law [2, 8], which is

Electromagnetic spectrum (Wavelength) [m]						
γ-Rays	X-Rays	UV	Visible	IR	Microwaves	Radiowaves
$< 10^{-11}$	10^{-11} -10^{-8}	10^{-8} $-8 \cdot 10^{-7}$	$8 \cdot 10^{-7}$ -10^{-6}	10^{-6} -10^{-3}	10^{-3} $-2 \cdot 10^{-1}$	$> 2 \cdot 10^{-1}$
Infrared spectrum (Wavelength) [m]						
Near-Infrared		Mid-Infrared			Far-Infrared	
$750 \cdot 10^{-9} - 1.5 \cdot 10^{-6}$		$1.5 \cdot 10^{-6} - 20 \cdot 10^{-6}$			$20 \cdot 10^{-6} - 1 \cdot 10^{-3}$	

Table 2.3: Classification overview of the electromagnetic and the infrared spectrum according to [8]

$$W = \frac{2\pi h c^2}{\lambda^5 \left(e^{\frac{h\nu}{kT}} - 1 \right)} \tag{2.3}$$

where

$$W \dots \text{spectral exitance}$$
$$h \dots \text{Planck constant}$$
$$c \dots \text{speed of light}$$
$$\lambda \dots \text{wavelength}$$
$$k \dots \text{Boltzmann constant}$$
$$T \dots \text{temperature}$$
$$\nu \dots \frac{c}{\lambda}$$

in wavelength form. Figure 2.3 illustrates the result of this law for different temperatures.

This figure shows, that the spectral exitance of a certain temperature follows a certain curve with a maximum at a certain wavelength. The location of this maximum (in terms of the wave length) is different for each temperature. The Wien displacement law describes the relationship between temperature and wavelength of the maximum ([2, 8]) as

$$\lambda_{max} = \frac{2897.7}{T} \tag{2.4}$$

and this relationship is represented as gray line in figure 2.3.

The total exitance of a black body can be calculated by integrating the spectral exitance over the wavelengths from $\lambda = 0$ to $\lambda = \infty$. The result of this integration is represented by the Stefan-Boltzmann equation [8, 13]
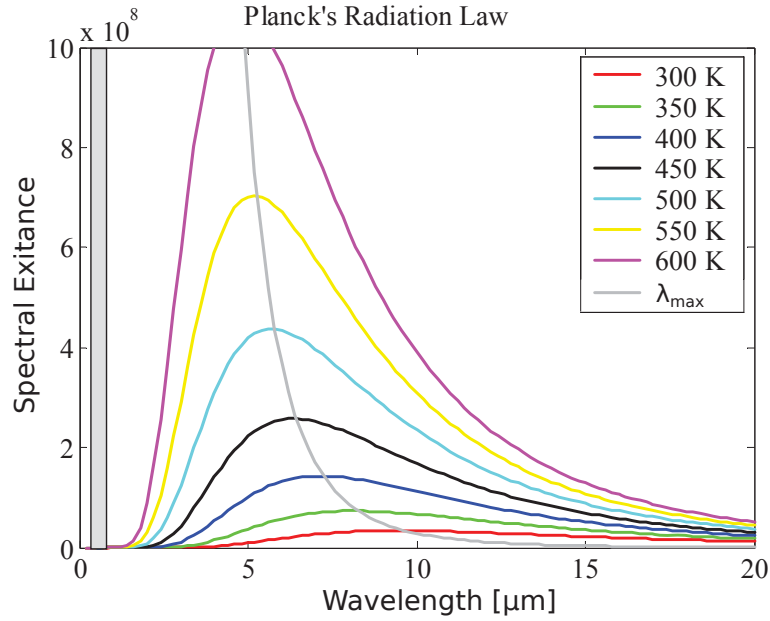
Figure 2.3: Spectral exitance for different temperatures dependent on the wavelength according to Planck's radiation law [2, 8, 34]

$$P = \sigma A T^4 \tag{2.5}$$

where

P ... emission power

σ ... Stefan-Boltzmann constant

A ... emitting surface

The radiation energy emitted by a surface is not the same as the energy absorbed by another surface which is directly irradiated by the first surface. The incident flux is defined by [2, 8]

$$\mathcal{A}(\lambda) + \mathcal{R}(\lambda) + \mathcal{T}(\lambda) = 1 \tag{2.6}$$

where

$$\mathcal{A}(\lambda) \dots \text{spectral absorptance}$$
$$\mathcal{R}(\lambda) \dots \text{spectral reflectance}$$
$$\mathcal{T}(\lambda) \dots \text{spectral transmittance}$$

Those three quantities describe the energy absorbed ($\mathcal{A}(\lambda)$), reflected ($\mathcal{R}(\lambda)$) or transmitted ($\mathcal{T}(\lambda)$) by a surface. Non of these variables can accept a negative value, which means that they will be between zero and one for any real surface. The spectral emissivity $\epsilon(\lambda)$ describes the radiation emitted by the surface and is equal to the absorptance [8]

$$\epsilon(\lambda) = \mathcal{A}(\lambda) \tag{2.7}$$

Different surfaces show different values for those quantities. One of the most important cases is the black body (as mentioned above). A black body does not reflect or transmit any radiation but absorbs all incident radiation - independent of the wavelength - and due to (2.7) it emits the absorbed energy in the spectrum which is significant for the particular temperature [8, 34]. In terms of the above stated quantities this yields

$$\mathcal{R}(\lambda) = \mathcal{T}(\lambda) = 0$$
$$\epsilon(\lambda) = \mathcal{A}(\lambda) = 1$$

Note that the emissivity of a surface depends on its temperature [8]. Since the temperature differences, which occur during the experiments and measurements presented in this work, are usually just a few Kelvin, the changes in emissivity are very small and therefore neglected.

The emissivity of a real surface will always be between zero and one. For good measurement results a high emissivity is desirable. Black paint can increase the emissivity of a surface significantly. Therefore, some specimens tested and presented in this work have been painted in black (described later in chapter 7). Emissivity values for a selection of materials are presented in table 2.4, [8].

2.4 Infrared Cameras

Old models of IR-detection systems used a single sensor and moving prisms or mirrors to scan a 2D image [8]. The prism or mirror is used to guide the radiation from a small part of

Material	Temperature [°C]	Emissivity
Polished aluminium	100	0.05
Polished steel	100	0.07
Oxidized steel	100	0.79
White paper	20	0.93
Lampblack	20	0.95
Polished glass	20	0.94
Human skin	32	0.98

Table 2.4: Emissivity values for a selection of materials [8]

the specimen's surface to the detector. After the sensor recorded the radiation from a small surface section, the prism/mirror moves on to repeat the process on a neighboring section. Through this an arbitrary surface can be scanned.

This technology is obsolete and modern IR-cameras use Focal Plane Arrays (FPA) [2]. In such systems a detector array, which uses much more than only one IR-sensor, is located in the focal plane of a camera system. Through this a 2D image can be recorded by the simultaneous scanning of all sensors. Thus, the detectors can be slower compared to the mechanical scanning systems, but are still able to achieve the same sampling rate. The resolution of hereby gathered images depends on the number of sensors on the detector array. Commonly used detector resolutions are 320×240, 640×480 or 1280×1024 [2].

One drawback of such camera systems are the high costs. Another problem is that the response characteristics of the individual sensors are not identical on the entire detector array [2]. Thus, the value of each pixel has to be corrected. This process is called Non-uniformity correction (NUC). To perform such a correction, a NUC table with correction parameters for every pixel is created by calibration of the sensor on a surface as uniform as possible.

Figure 2.4 provides an overview of different IR-detectors. Note that only the bolometer (microbolometer) and the photonic detectors are interesting for this work and are therefore the only detectors which are described in detail in the following section.

Bolometer detectors consist of resistive elements which change their electrical conductivity with temperature [2]. Through this, incident radiation changes the electrical resistance of the detector. This change can be measured by guiding a bias current through the detector and measuring the output voltage.

For the practicability of such detectors two properties are important [2]:

- For a high speed camera or a high recording frequency respectively, the thermal capacity of the detector has to be as small as possible, so that a change in radiation energy yields a change in temperature as fast as possible.

- For high sensitivity of the camera the detector needs to exhibit a high temperature
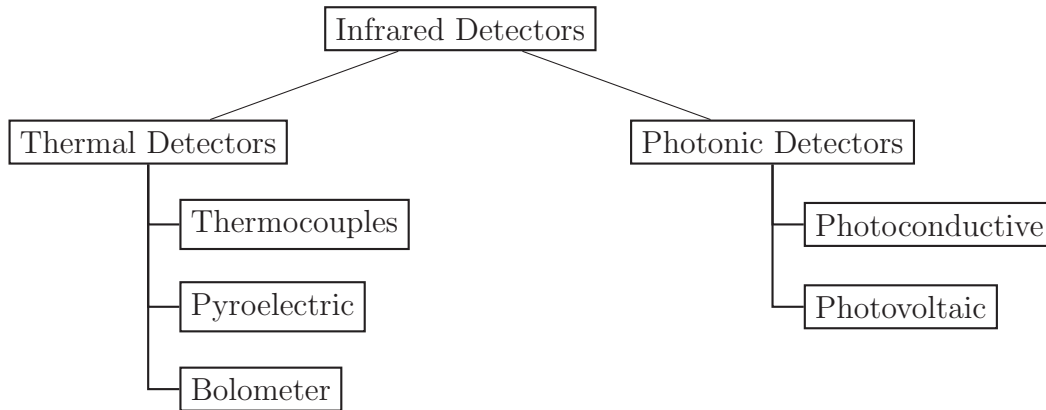
Figure 2.4: Overview of different IR-detectors [2]

coefficient (TCR), so that a change in temperature yields a change in resistance as high as possible.

The elements may consist of e.g. metals, coated with a black absorber or semiconductor materials. Note that semiconductors (such as VO_x) show much higher TCR values (in terms of absolute values) than metals [2].

Compared to the bolometer detectors the photonic detectors do not generate an output due to the energy of incident photons but to the rate of absorption of those photons. The two variants of such sensors are [2]:

- **Photoconductive detectors** change their conductivity due to incident photons. Those photons generate charge carriers in the material, which can be electrons, holes or electron-hole pairs. Typical materials are indium antimonide (InSb), mercury cadmium telluride or lead sulfide/lead selenide.

- **Photovoltaic detectors** generate free charge carriers due to photon absorption. Those charge carriers are separated within the potential of the pn junction. If the two semiconductor layers are not connected through an electrical conductor, a voltage can be measured between those two layers. Typical materials are indium antimonide (InSb), mercury cadmium telluride and platinum silicide.

Microbolometer cameras are less complex than photonic detector cameras because they do not need to be cooled to very low temperatures. This makes them cheaper. On the other hand, photonic detector cameras are faster (which results in a higher recording frequency) and they show higher sensitivity to temperature differences [2]. In the experiments presented in this work, temperature changes, which appear on specimen surfaces and which are important for the measurement evaluation, often take place within very short time intervals. Therefore, the recording frequency needs to be very high. Thus, for the experiments and measurements performed for this work, a photonic detector camera is necessary.

2.5 Thermographic Material Testing Methods

Thermography can be divided into two main classes [3], [2]:

- **Passive thermography:** An IR-camera is used to measure temperature and temperature distribution on a test object. No external energy source is necessary, the temperature of the inspected body is not influenced during the measurement. This method is often used to investigate test objects which show a significantly higher temperature than their surrounding. Applications are for e.g. temperature measurements in production industry, medical examination of human bodies or inspection of sources of heat loss on buildings.

- **Active thermography:** A specimen is excited by an energy source (e.g. US excitation, electro-magnetic induction, flash light) and the thermal response of this specimen is detected with an IR-camera. This method has its main application in non-destructive material testing.

The measurement methods presented in the following chapters of this work use not only the temperature or temperature distribution on specimens to detect anomalies, but also the temporal progress of heating and cooling. To achieve a representative measurement, those specimen have to be stimulated with a well-defined heat source. Thus, only the active thermography is dealt with in this thesis. Furthermore, we use a flash light to excite the specimens.

The following sections present a short introduction to three different thermographic measurement and evaluations methods. The physical and mathematical principles of the used methods are explained in more detail in chapter 4.

2.5.1 Evaluation of Temperature Profiles

A specimen is excited by a pulse-like stimulation [3]. Through this pulse, the surface of the specimen is heated and subsequently this heat conducts through the specimen. The thermal progress on the front and rear side of the specimen can be recorded with an IR-camera. Using appropriate evaluation techniques, those thermal progresses can be represented in analytical form. Afterwards significant information is derived from those mathematical results. This information can be related to physical properties of the specimen, such as thermal diffusivity. Through this, qualitative and quantitative information about defects in a specimen can be gained [3].

2.5.2 Lock-In Thermography

A specimen is excited by a sinusoidal signal [2]. This excitation can be performed using e.g. an inductive or an optical stimulation. The inserted heat conducts through the material as wave, similar to the technique described above. Because of the sinusoidal stimulation, this heat conduction will take the form of stationary waves (corresponding to the stimulation signal). The waves will be reflected at the opposite side of the specimen and are measurable at the front side (which is the excited surface) again. The measured data is transformed using a Fourier transformation. This yields, among some other information, the phase shift between excitatory signal and the measured signal. If the heat wave is now reflected on a defect within the specimen, this phase shift will exhibit different values compared to the phase shift of the heat waves reflected at the rear side of the specimen. Thus, defects can be detected by computation of the measurement signal's phase shift. To penetrate different depths, different stimulation frequencies have to be used consecutively [2].

2.5.3 Pulsed Phase Thermography - PPT

The PPT combines characteristics of both the evaluation of temperature profiles and the Lock-In technique ([2], [14]). It again uses a short pulse, which is much quicker than the Lock-In method. Again, the thermal response on the surface is recorded and the data is transformed using a Fourier transformation. Thus, the pulse signal is divided into a number of sinusoidal signals. Similar to the Lock-In technique, the phase shift of each sinusoidal component can be computed and therefore a result can be gained which is similar to the Lock-In technique but requires much less time.

3 Experimental Rig

3.1 Overall Setup

A schema of the overall experimental rig is illustrated in figure 3.1.
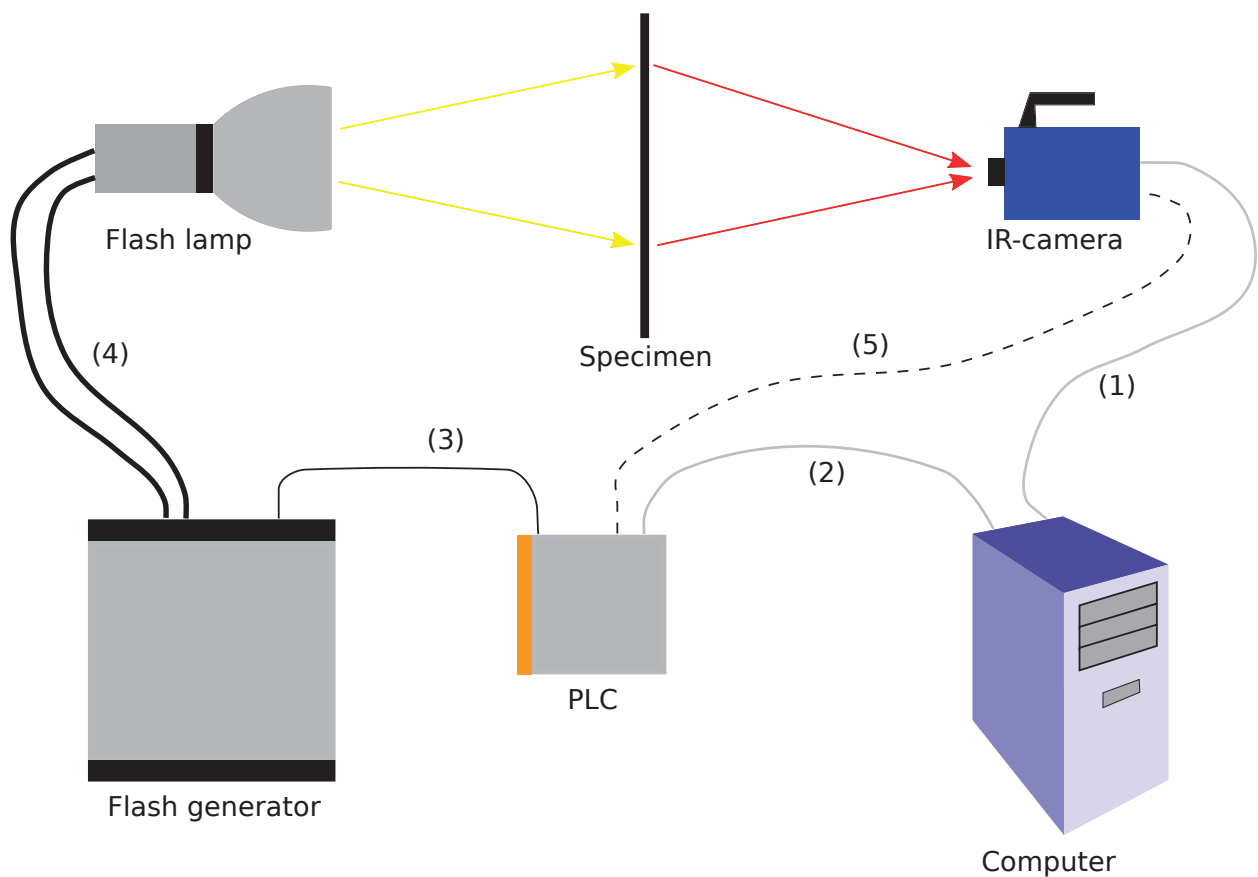

Figure 3.1: Schema of the experimental rig for a measurement in transmission mode

This test setup demonstrates a measurement in "transmission mode". A measurement where IR-camera and flash lamp are positioned on the same side of the specimen is called a measurement in "reflection mode" and illustrated in figure 3.2.

The user operates the computer which runs the measurement software. This computer is connected to the IR-camera via Ethernet (Gigabit Ethernet, "GigE") cable (1). Through this connection the measurement software receives the recorded data from the camera. The
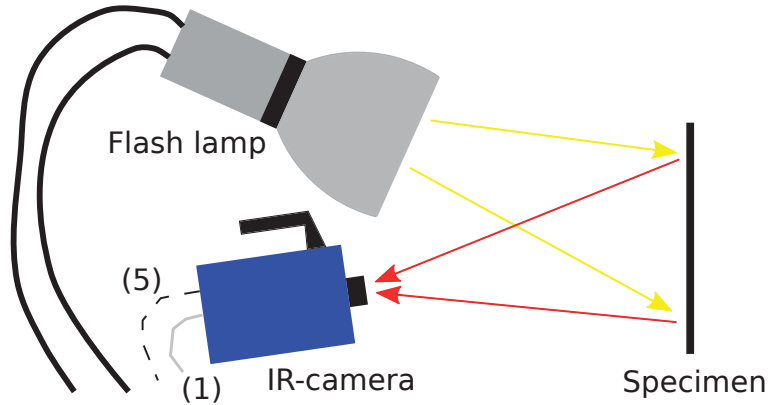
Figure 3.2: Setup for a measurement in reflection mode

data gathering is done by C routines (written by Prof. Oswald-Tranta) based on the Software Development Kit (SDK) library, delivered with the camera. Those routines read the recorded image frames from the camera, buffer the data in the RAM of the PC until the measurement is completed and then write it to the HDD. The format in which the records are stored is a FLIR standard called "ptw". The computer is also connected to the Programmable Logic Controller (PLC) via Ethernet cable (2). After receiving a command for a flash triggering from the computer (from the measurement software, respectively), the PLC triggers the flash generator via a 2-phase cable (3). This flash generator triggers the flash by feeding the flash lamp with a high but short current pulse via the power cables (4). The PLC is additionally connected to the camera via a 2-phase cable (5). This connection enables a direct flash detection through lock-in (see later, section 5.1.4), but is optional.

The following sections describe all parts of the setup. Figure 3.3 illustrates the communication between the different parts of the rig.
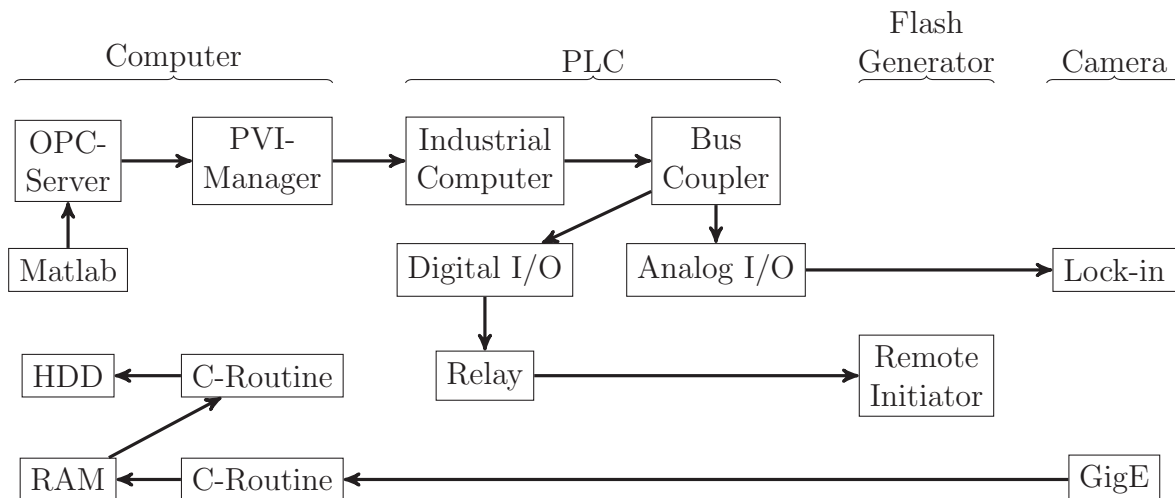

Figure 3.3: Communication between the different parts of the rig

Figure 3.4 illustrates the actual implementation of the experimental rig. "ROBOTUNITS" beam modules with a cross section of $40mm \times 40mm$ and various lengths have been used to create a frame which mounts all components. The whole frame can be covered by a curtain made from Mollitan (also known as Molton), which is a thick and tight cotton mesh. This curtain can be lowered before a measurement and is supposed to block all radiation (especially in the IR-spectrum) from outside the rig during the measurement. The glass plate in front of the flash lamp and the light shade are supposed to reduce disturbing IR-radiation from the flash lamp to the IR-camera. This is discussed in detail in chapter 5.1.

3.2 Computer

The computer used for the measurements is a personal computer with Microsoft Windows 7 operating system. The following software is necessary for the execution and evaluation of the measurements:

- The numerical computational program MATLAB (32 bit), which is used for providing a graphical user interface (GUI) for the measurement control as well as for the data evaluation - this self-made software is described in section 3.6 in more detail. A OPC toolbox is added to this program to enable communication to a OPC server.

- The OPC (Open Platform Communications) server software from "B&R" which implements an OPC server on the system. This server enables the communication to MATLAB (via OPC) and forwards the communication to the PVI manager.

- The PVI manager is also a B&R product and enables the communication between the computer and the PLC via a B&R intern communication protocol.

- The C routines which receive the recorded frames from the camera and save them to the RAM/HDD.

Since the image processing task can be computationally intensive, the computer is equipped with high-performance components which are:

- Intel Core i5-3470 processor

- 16GB of RAM

- 120GB Solid State Disk for fast storage access due to big data file handling
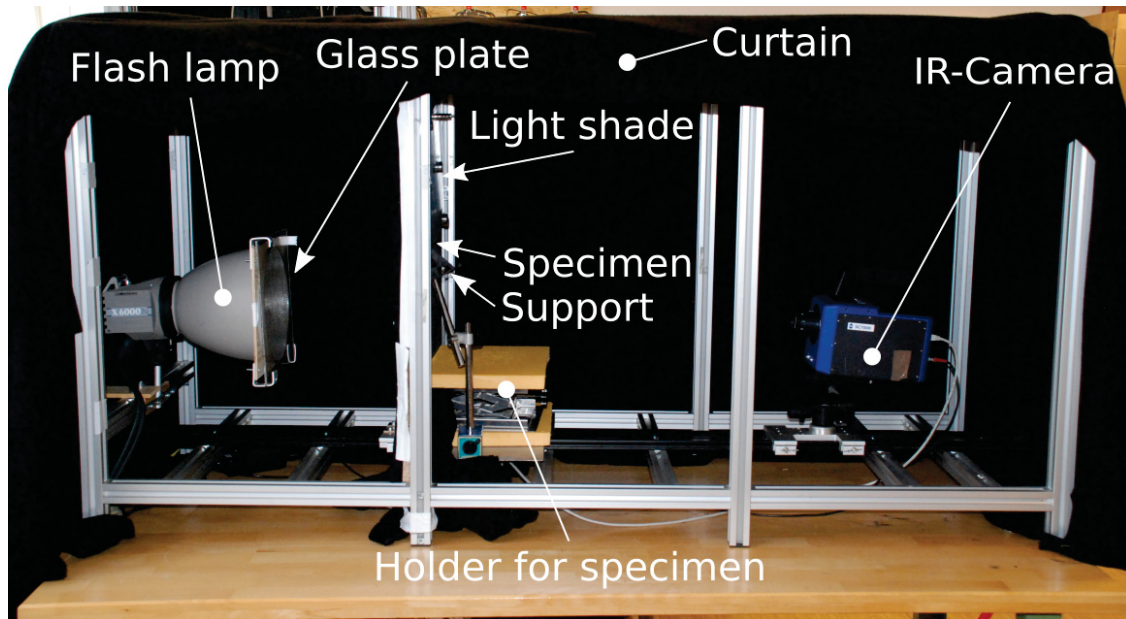
(a) Transmission Mode
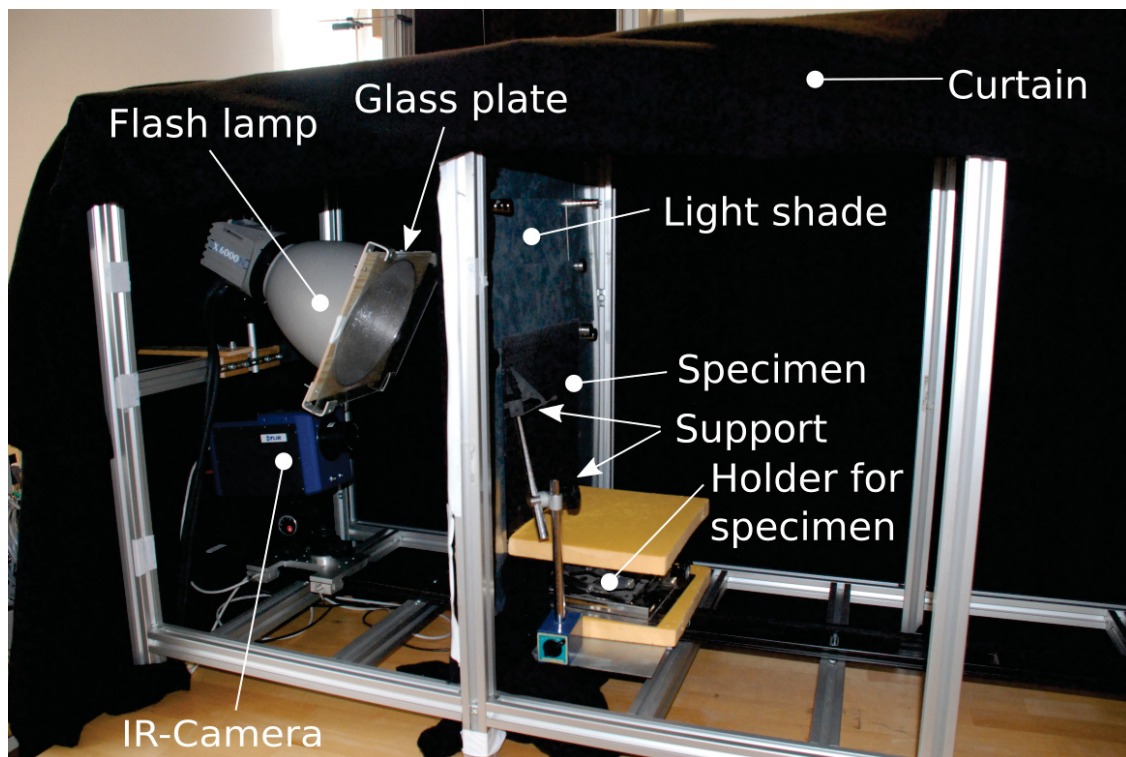
(b) Reflection Mode

Figure 3.4: Actual implementation of the experimental rig. Note that the light shade has no
          relevance in reflection mode (figure (b)). However, it was inserted before taking
          the picture, because it is better visible than in figure (a) and is therefore suited
          to illustrate the usage of the light shade in transmission mode.

3.3 Programmable Logic Controller (PLC)

The PLC was assembled and enabled by Gerold Probst from the Institute for Automation. It consists of an industrial personal computer which runs a PLC operating system. The computer is a B&R APC620 and the operating system the B&R Automation Runtime. This run time implements a PLC and therefore turns the computer into a PLC. The industrial personal computer is connected to a digital and analog input/output (I/O) interface through a bus coupler. This coupler consists of a B&R LS189, connected to the PCI interface of the APC620, and a BR 9300, which is connected to the I/O module. The two parts of the bus coupler are connected to each other via a X2X link. The analog output is able to emit 0-10V and the digital output switches between 0V and 24V and is connected to the relay. The lock-in signal for the camera is fed by the analog output which is set from 0V to 3V for one second when the flash generator is triggered. The relay, which triggers the flash generator via the remote initiator, is fed by the digital output. This digital output is set from 0V to 24V when the relay needs to trigger the flash generator and thus the relay shortens the remote initiator of the flash generator.

3.4 Infrared Camera

The used IR-camera is a FLIR Titanium SC7500 MB. Table 3.1 provides a basic information overview of this camera type [15].

FLIR Titanium SC7500 MB	
Detector	Indium Antimonide (InSb)
Spectral Range	MW
Detector Response [μm]	1.5-5.1
Resolution [Pixels]	320x256
Integration Time [μs]	3 - 10000
Full Frame Rate [Hz]	1 - 380
NETD @ 25°C [mK]	< 25
Standard Temperature Range [°C]	5 - 300

Table 3.1: IR-camera specifications

The interface to connect the IR-camera to a computer is a GigE connection. Two lenses are available for this camera:

- Focus: 25mm; Field-of-view (FOV): 22°x17°

- Focus: 50mm; Field-of-view (FOV): 11°x8.8°

3.5 Flash Light System

The flash light system consists of a generator and a flash lamp. Basic specifications of the generator ([37]) are summarized in table 3.2.

Elinchrom Classic 6000	
Provided energy [J]	6000
Recharging time [s]	5.5
Flash duration $t_{0.5}$ max [s]	1/1150
Synchron voltage [V]	12
Dimensions [cm]	49 x 14 x 43
Weight [kg]	17

Table 3.2: Generator specifications

The flash lamp is an Elinchrom Twin X 6000 N which is capable of generating a flash light with an energy of 6000J. It was used together with a H.P. reflector (diameter of 26cm, angle of radiation of 48°).

The generator has a remote initiator which enables the PLC to trigger a flash via a 2-phase cable. It is connected to the flash lamp by two power cables. The usage of both cables at once cuts the recharging time in half (Note: the given value in table 3.2 is the one when using both cables).

The duration of the flash pulse or the progress of the light output, respectively, is very important. An ideal flash light pulse would be of no temporal extent and therefore infinitely short. However, a real flash lamp generates radiation for a certain time duration and with changing amplitude, compare [24]. Figure 3.5 illustrates the progress of such an output for a real flash lamp.

An important property of this progress is the time duration after which the amplitude of the flash light has decreased to 50%. This time duration is named $t_{0.5}$ and represents a characteristic value for a flash lamp ($t_{0.1}$ is defined in the same way). This parameter is given in table 3.2.

Note that there are ways to reduce the length of the pulse by stopping the discharge current through the flash lamp by the usage of specific electrical circuits. One of those is described and patented in [25].

3.6 Measurement Software

As stated before, the measurement software was written in MATLAB (except for the C routines for image gathering). Therefore, the GUIDE (graphical user interface design envi-
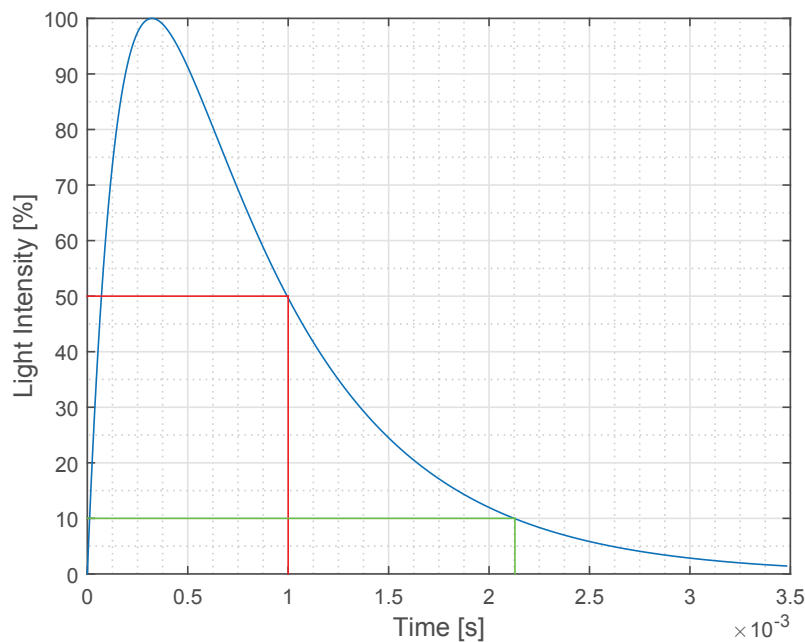
Figure 3.5: Progress of a real flash pulse [24]. The plotted marks represent $t_{0.5}$ (red) and $t_{0.1}$ (green).

ronment) toolbox was used to create a GUI. The main component of the developed software (the main "window" respectively) is illustrated in figure 3.6.

The individual panels of this main GUI are described in the following section.

- **Connection Settings:** This panel includes two buttons which enable and disable the connection to the camera and the PLC.

- **Live Frame Panel:** To enable a live stream from the camera (e.g. to focus the lens or to adjust the specimen) the following tools are in this panel:

  - **Start/Stop Live Frame:** This button activates the live frame in the corresponding window (as demonstrated in figure 3.6).

  - **Max Size...:** This button opens a new enlarged window with a live stream. This helps the user to focus the lens.

  - **Camera Settings...:** This button opens a new window which contains all changeable camera settings. Those are:

    * Frequency

    * Integration time

    * Execution of a NUC (non-uniform calibration)

    * Window width and height
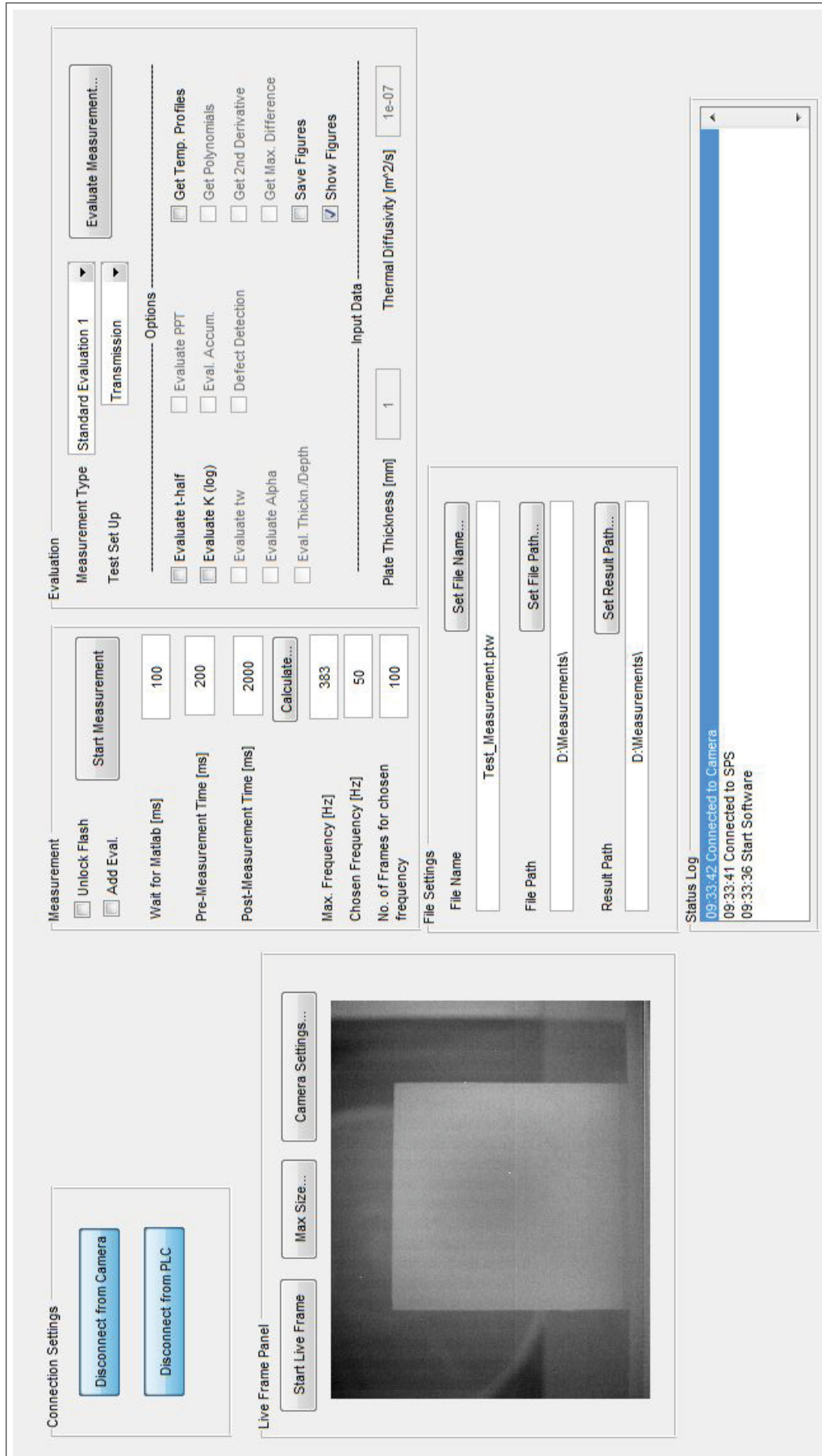
Figure 3.6: Main GUI of the developed measurement software in MATLAB

  * Window position (if the selected width and height are smaller than full resolution)

   – **Live Frame:** The live frame displays the chosen camera window with the chosen frequency.

- **Measurement:** The measurement panel contains all necessary information and options for the measurement execution. The corresponding parameters are predefined at software start using arbitrarily chosen values.

   – **Unlock Flash:** As a precaution this check box must be checked by the user before a measurement (which includes a flash triggering) is executed. This is to prevent the user from unintended flash triggering. After every measurement, the check box is automatically unchecked again.

   – **Add Eval.:** If this check box is not checked, a measurement is executed and the result is saved. If it is checked, an evaluation according to the settings (see evaluation panel) is carried out directly after the measurement (compare figure 3.8).

   – **Start Measurement:** This button starts the measurement (as long as the "Unlock Flash" check box is checked) with the defined settings. During the measurement the software displays a progress bar which informs the user about the remaining measurement time. The user can cancel a measurement with the cancel button directly on the wait bar window.

   – **Wait for Matlab [ms]:** As soon as MATLAB gathers images form the camera during a measurement, it is locked in a loop. It is not possible, to start the recording and then trigger the flash generator (if both tasks are executed by MATLAB). Therefore, the software sends a flash trigger to the PLC and then starts the image gathering. The PLC triggers the flash a defined time span after the command from MATLAB. This defined time span must be long enough for the software to start the image gathering after it commanded the trigger but before the flash is actually triggered by the PLC. The time span can be set with the here described option.

   – **Pre-Measurement Time [ms]:** During the Pre-Measurement Time, images are recorded before the flash light to receive the initial temperature of the specimen (T_0). Note: The PLC sums up both time intervals before the measurement ("Wait for Matlab" and "Pre-Measurement Time") and triggers the flash after this total time delay.
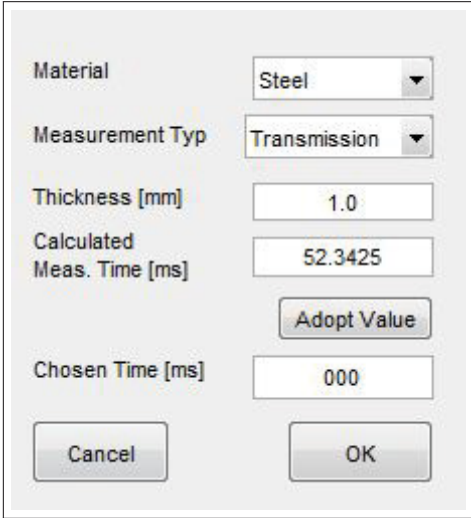
– **Post-Measurement Time [ms]:** This is the time span which shall be recorded after the flash light. The total time to be recorded is therefore the sum of "Wait for Matlab", "Pre-Measurement Time" and "Post-Measurement Time".

– **Calculate...:** Specimens of different materials and in different thicknesses need different recording times to ensure that the record contains enough information to carry out an evaluation. A guide value can be provided by the implementation of the record length estimation presented in section 4.5. The button opens a new dialog which is illustrated in figure 3.7. The user needs to specify material, measurement mode and thickness of the specimen. The calculated value can then be adopted using the corresponding button or the user enters a value and proceeds to the main GUI with OK. This chosen value is automatically inserted into the "Post-Measurement Time" field.

– **Frequency:** The fields "Max. Frequency [Hz]", "Chosen Frequency [Hz]" and "No. of Frames for chosen frequency" can not be edited. Those values result from the camera settings and measurement settings. They provide a calculation of the resulting data file size ("No. of Frames for chosen frequency"). This is important since the 32 bit version of MATLAB can not process files of more than (approximately) one GB. Therefore, the number of frames (or images, respectively) need to be kept below a certain limit related to the chosen resolution. If the required number of frames exceeds this limit, the "No. of Frames for chosen frequency" field turns red to inform the user about this problem.

- **File Settings:** With the file settings panel the user is able to choose the location on the hard disk where the measurement files and the results shall be saved. The data can be changed with the corresponding buttons.

  – **File Name:** The name of the data file which stores the complete measurement. The software adds an index at the end of this name. Thus, if the user executes multiple measurements with the same name, an old data file will not be replaced by a new one. They will be stored in the processed order including the particular index.

  – **File Path:** The directory in which the data files are to be saved.

  – **Result Path:** The directory in which the results of the evaluations are to be saved. The software uses the file name of the data file (plus some indexes, depending on the chosen evaluations) as name for the result files (all results are saved as PDF). The initial value of the path is predefined.

- **Status Log:** The system informs the user about important steps during the software

handling. Those status notifications are displayed in the status log together with the time of occurrence in the according order (newest notifications at the top of the log).

- **Evaluation:** The evaluation panel contains all properties which influence the evaluation of a data file. Note that some options are disabled. This is because the software automatically disables options which can not be used together with other selected options.

  - **Measurement Type:** Figure 3.6 shows the type option "Standard Evaluation 1". This evaluates the data files and returns the results as presented in the following chapters of this work. If a number of measurements of a specific type are to be carried out and which focus on the investigation of specific phenomena, the software offers the possibility to expand the evaluation methods. This expansion can use different subroutines, which were developed for the standard evaluation, and combine them to a completely new evaluation which focuses on the desired properties of the measurement. Those customized evaluations can also provide a preparation of the results which exactly suite the specific task.

  - **Test Set Up:** This option specifies the measurement mode in transmission or reflection. Depending on this choice, different menu items in the "Options" field are enabled or disabled.

  - **Evaluate Measurement...:** The user is asked to choose one or more data files on the hard drive to evaluate. The evaluation starts and works off the list of data files as soon as the user confirms the selection.

  - **Options:** The "Options" list enables the user to specify the desired evaluation information. The specific options are:

    * **Evaluate t-half:** $t_{1/2}$ evaluation for measurements in transmission mode according to Parker's method described in section 4.2.1.

    * **Evaluate K (log):** Evaluation of the slope K for measurements in transmission mode according to the logarithmic method described in section 4.2.2.

    * **Evaluate Alpha:** Computation of the thermal diffusivity depending on the chosen evaluation method ($t_{1/2}$, K or t_w evaluation, compare sections 4.2.1, 4.2.2 and 4.3). The result is presented as image where every pixel represents the computed value on this point of the specimen surface. Additionally, the average value of the whole image is calculated and returned as text in the result image (in the head line). The thickness of the specimen needs to be known (see "Input Data" field).

* **Evaluate Thickness/Depth:** Computation of the thickness of the specimen or the depth of a defect depending on the chosen evaluation method ($t_{1/2}$, K or t_w evaluation, compare sections 4.2.1, 4.2.2 and 4.3). The result is presented as image where every pixel represents the computed value on this point of the specimen surface. The thermal diffusivity of the specimen needs to be known (see "Input Data" field).

* **Evaluate tw:** t_w evaluation for measurements in reflection mode according to section 4.3.

* **Evaluate PPT:** For reflection mode measurements a PPT evaluation is available, which performs such an evaluation according to chapter 4.4 and 5.4. During the evaluation, the user is asked to enter the number of frequencies to be evaluated, beginning from the lowest available frequency. As result, the number of phase shift images which has been specified by the user is returned and displayed.

* **Eval. Accum:** The evaluation of the accumulated images is available when the "Evaluate PPT" option is enabled. Using this option, the Difference Accumulation and the Value Accumulation (see chapter 5.4) are computed and displayed.

* **Defect Detection:** This option is available when either "Evaluate t-half", "Evaluate tw" or "Evaluate PPT" is enabled. The results of the chosen upstream computations (in case of reflection mode both possible evaluation modes, "Evaluate tw" and "Evaluate PPT", can be selected at once) are used in the image processing described in chapter 6. In case of the usage of a PPT result for the defect detection, the user is interactively asked to choose one of the received phase images for further processing. If the option "Eval. Accum" is selected, the Difference Accumulation image is additionally used for the defect detection (thus two resulting images from the defect detection are computed). The end results are returned and displayed.

* **Get Temp. Profiles:** If this option is enabled, the evaluation returns the temperature profiles of selected points of the camera window (see section 5.5). Note: This option returns different results for transmission and reflection measurements (logarithmic representation of profiles in reflection mode).

* **Get Polynomials:** Returns the fitted polynomials (see section 5.5) instead of the raw data. Note: This option is available only for measurements in reflection mode.

* **Get 2nd Derivative:** Returns the second derivative of the fitted polynomials (see section 5.5). Note: This option is available only for measurements in reflection mode.

* **Get Max. Difference:** Returns the second derivative of the fitted polynomials at the maximum difference (see section 5.5). Note: This option is available only for measurements in reflection mode.

* **Save Figures:** The evaluation returns the results on various graphs and images, depending on the selected options. Through the option "Save Figures", the software saves all result figures with different indexes (depending on the selected options) in the result directory, specified by the "Result Path" in the "File Settings" panel (see above).

* **Show Figures:** The evaluation of a high number of data files yields an even higher number of result figures. If the user wants to evaluate multiple data files, but wants the results just to be saved in the results directory, the user can disable the "Show Figures" option (Note: this option is enabled by default).

− **Input Data:** The "Input Data" field enables the user to make a numerical input. This can be necessary for the evaluation, depending on the selected option. If thermal diffusivity or thickness/depth need to be evaluated, the software needs the complementary input. Note: The computation of one of those properties excludes the other one. Therefore, the input fields are disabled in the according way.

Figure 3.7: Dialog for record length estimation

Figure 3.8 illustrates the process of measuring and evaluating respectively. As soon as the software started, the user is interactively asked to choose a directory and file name for the records to be saved. After the main GUI is loaded successfully, the following procedure depends on if the user wants to execute a measurement or an evaluation.

Measurement

If the user wants to perform a measurement, the first steps are to connect the computer to the camera and the PLC. Next, the camera settings are to be set. Those are frequency, window size and window position. Afterwards the user needs to position the specimen correctly in front of the camera and focus the camera lens. As soon as the hardware is set, the measurement parameters, which are pre and post measurement times (by usage of the record length estimation tool if necessary) can be entered. At this point the user can press the start button and the measurement is executed. If the option "Add Eval." is selected, the recorded file is directly evaluated after the measurement. Note: If the evaluation is added directly, the user needs to set all evaluation settings before the measurement starts!

Evaluation

To perform the evaluation of a recorded file, the user first selects the measurement type (e.g. the "Standard Evaluation 1") and the measurement mode (transmission or reflection). Next, the options are to select and the necessary input data has to be provided. After those inputs the user can press the start button which starts the evaluation procedure in the specified way. If the user selected multiple files, the system evaluates all those files in a row. Note that the software uses the same settings for all data files in case of multiple selections!
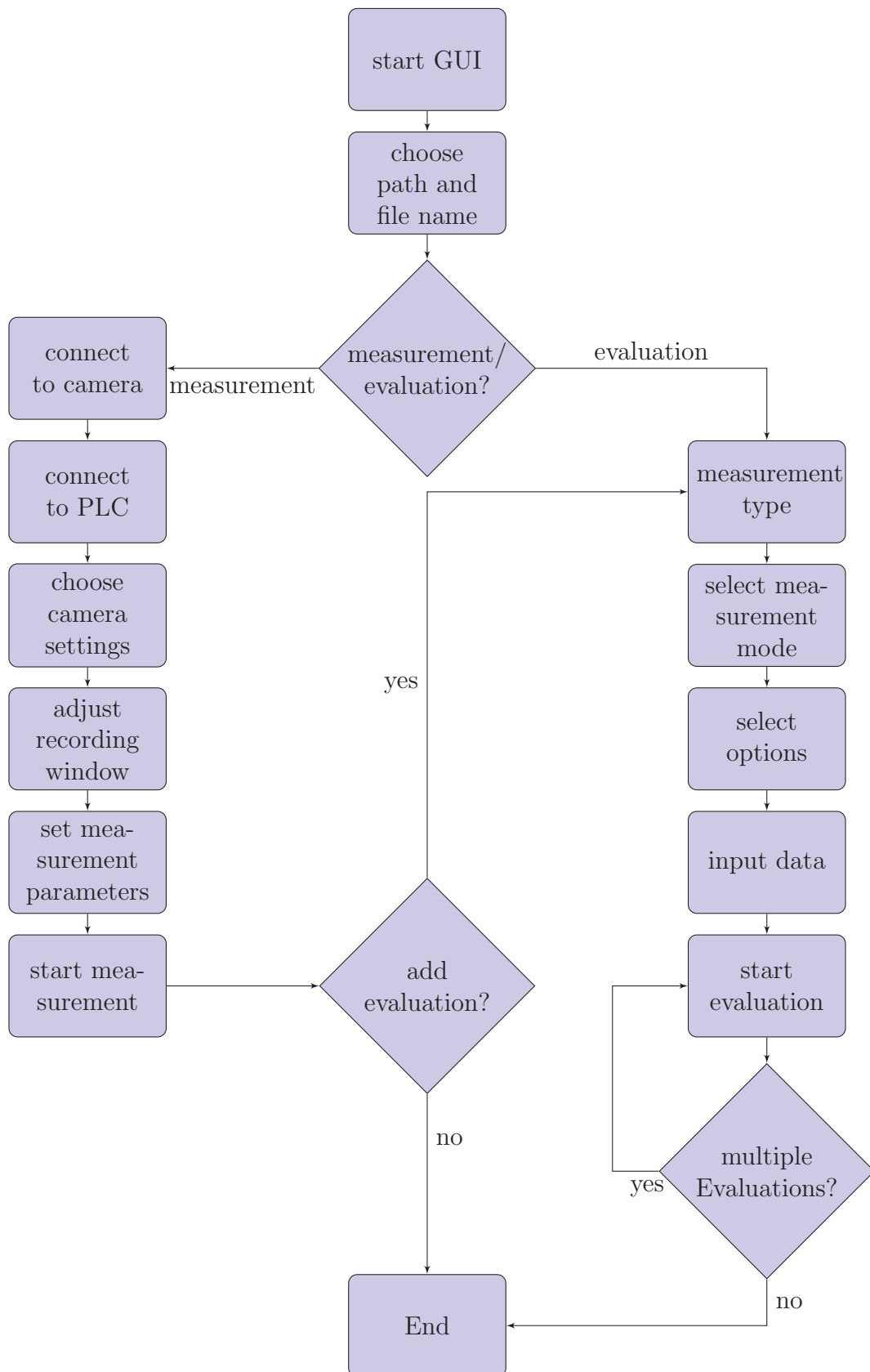
Figure 3.8: Flow chart of a measurement/evaluation

4 Evaluation Methods

4.1 Heat Flow Model

In the course of a measurement, a specimen is excited by a flash light. The radiation energy of the flash light is absorbed by the excited surface, therefore it is heated up (this very short heating duration is assumed to be instantaneous). This excited surface is hereafter referred to as "front surface". The heat gradient within the specimen causes the heat to diffuse through the material. This causes the temperature on the front surface to decrease. This decreasing process can be detected with an IR-camera when performing a measurement in reflection mode. Due to the heat diffusion, the temperature on the opposite surface of the specimen - hereafter referred to as "rear surface" - increases. This temperature increase can also be detected with the IR camera when performing a measurement in transmission mode.

The heat flow through the material can be modeled using Parker's method [18]. This model makes the following assumptions:

- The heating of the surface happens instantaneously

- An infinite body along x- and y-axis (no influence of rims)

- Adiabatic specimens, meaning no heat radiation or convection to or from the environment, except for the heating pulse

Parker's model describes the temperature increase on the rear surface and the temperature decrease on the front surface with the equations [18]

$$T_{model}(z = L, t) = \frac{Q}{\rho c L} \left[1 + 2 \sum_{n=1}^{\infty} (-1)^n \exp \left(\frac{-n^2 \pi^2}{L^2} \alpha t \right) \right] \tag{4.1a}$$

$$T_{model}(z = 0, t) = \frac{Q}{\rho c L} \left[1 + 2 \sum_{n=1}^{\infty} \exp \left(\frac{-n^2 \pi^2}{L^2} \alpha t \right) \right] \tag{4.1b}$$

where

$$Q \ldots \text{deposited energy}$$
$$\rho \ldots \text{density}$$
$$c \ldots \text{heat capacity}$$
$$L \ldots \text{specimen thickness}$$
$$\alpha \ldots \text{thermal diffusivity}$$
$$t \ldots \text{time after excitation}$$

The end temperature which appears after all dynamic processes (processes are considered as dynamic as long as there is a temperature gradient within the material) is given through [2]

$$T_{end} = \frac{Q}{\rho c L} \tag{4.2}$$

Two dimensionless parameters are defined [18]:

$$V(z, t) = \frac{T_{model}(z, t)}{T_{max}} \tag{4.3a}$$

$$\omega = \frac{\pi^2 \alpha t}{L^2} \tag{4.3b}$$

where $T_{\max}$ represents the maximum temperature on the rear surface and the end temperature (minimum temperature) on the front surface. This value equals T_{end}. The combination of (4.1a) and (4.1b) respectively, (4.3a) and (4.3b) yields [18]

$$V(L, t) = 1 + 2 \sum_{n=1}^{\infty} (-1)^n \exp\left(-n^2 \omega\right) \tag{4.4a}$$

$$V(0, t) = 1 + 2 \sum_{n=1}^{\infty} \exp\left(-n^2 \omega\right) \tag{4.4b}$$

where (4.4a) describes the temperature increase on the rear surface in transmission mode and (4.4b) describes the temperature decrease on the front surface in reflection mode.

Figure 4.1 illustrates the temperature profiles for both measurement modes derived from this model. Note: In reality the temperature decreases after it reached the maximum temperature in transmission mode (compare figure 4.1(a)) and after the (temporary) minimum

temperature in reflection mode. This is due to the violation of the assumption of an adia-batic specimen. It transfers heat energy to the environment till it reaches the surrounding temperature. This deviation from the model effects only specific further measurements. The following evaluation methods do not need data after reaching the temperature peak in trans-mission mode and the temporary minimum temperature in reflection mode and thus most measurements can be evaluated by neglecting this deviation from the model. However, it does influence some later described measurements, compare therefore chapter 7.

(a) Transmission Mode   (b) Reflection Mode
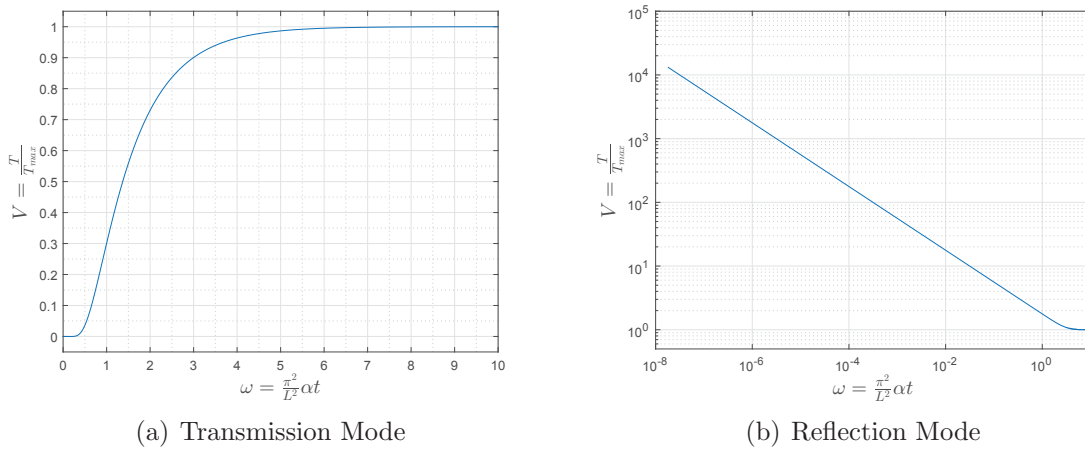
Figure 4.1: Temperature profiles on rear and front surface for transmission and reflection mode.

4.2 Measurement in Transmission Mode

4.2.1 Significant Temperature Increase - $t_{1/2}$

Parker [18] suggests to measure the time duration between the excitation and reaching half of the total temperature increase. This point in time - hereafter referred to as $t_{1/2}$ - is illustrated for the analytical model with normalized parameter in figure 4.2.

In the model, $t_{1/2}$ is equivalent to $\omega = 1.37$. Since the parameters are all normalized, this value can be considered as a constant. Note: This value slightly differs from the constant stated by Parker in [18] which is $\omega = 1.38$, but the computed (MATLAB computation) models used for this work all yield an ω-value of 1.37. Therefore, for all further considerations $\omega(t_{1/2}) = 1.37$.

Using equation (4.3b) and the derived constant $\omega(t_{1/2}) = 1.37$, the thermal diffusivity can be calculated as

$$\alpha = \frac{1.37 L^2}{\pi^2 t_{1/2}} \tag{4.5}$$
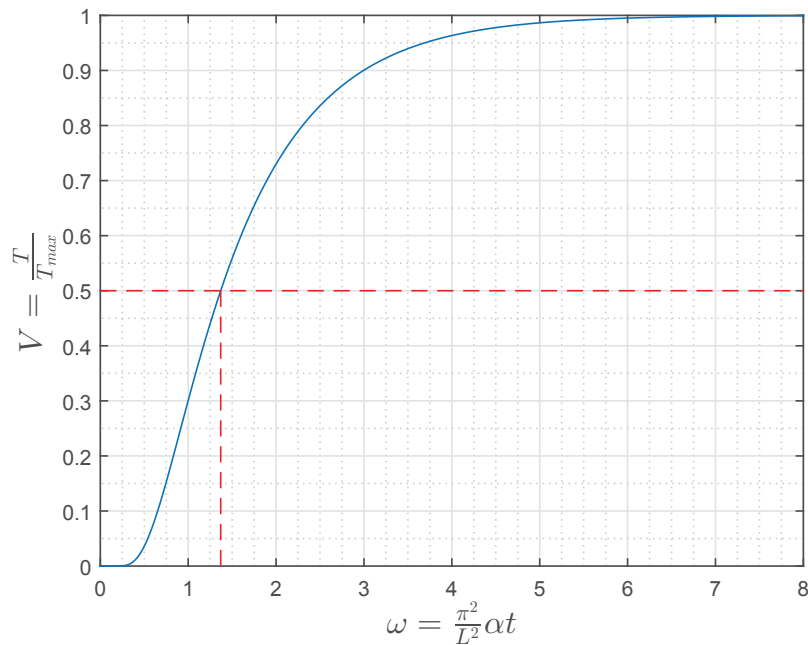
Figure 4.2: Determination of $t_{1/2}$ for the analytical model in transmission mode.

With this relationship it is possible to calculate the thermal diffusivity (or the thickness if the thermal diffusivity is known, respectively) of a material by determining $t_{1/2}$ in transmission mode.

4.2.2 Logarithmic Transformation

A main drawback of Parker's method presented in chapter 4.2.1 is the difficulty to determine the maximum temperature increase, the temperature $T_{\max}$ as well as the corresponding point in time $t_{\max}$. This problem is illustrated in figure 4.3.

Even if the temperature profile is averaged over a certain number of points on the surface and smoothed afterwards, distinct values can not be derived from the data. Even more serious is the fact that the preconditions from the model are violated in a real measurement, since heat energy is dissipated to the environment *during* the record. Thus, T_{max}, which should be reached due to the model, the parameters and the measurement condition, can not be reached in reality. This distorts the results.

To eliminate this disadvantage a different method to calculate the thermal diffusivity was suggested by [28] and applied by [9]. The following considerations are based on the procedure presented by [9].

For the logarithmic representation, the temperature profile is transformed to [9]

$$T_{log} = log \left[\frac{T(L,t) - T_0}{T_{max} - T_0} \right] + \frac{1}{2} log(t) \tag{4.6}$$
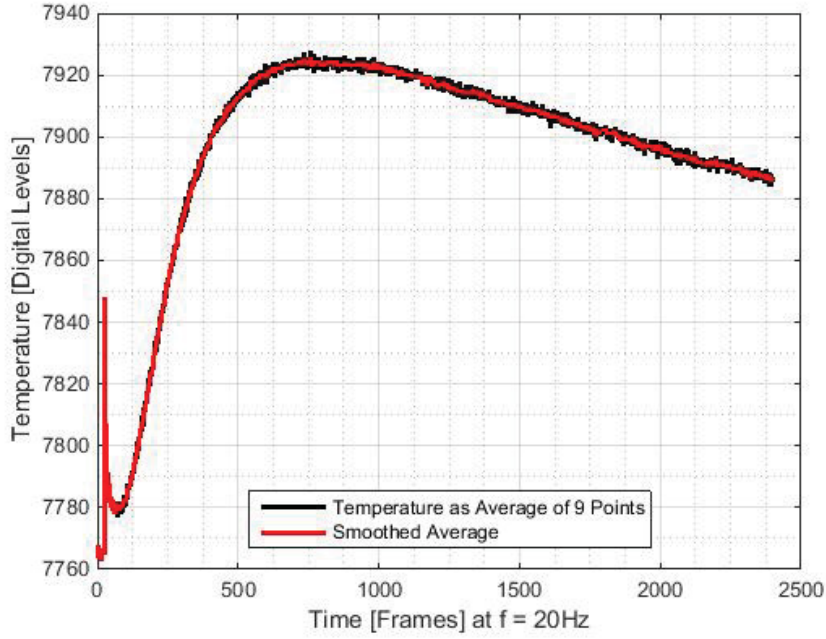
Figure 4.3: Temperature profile on the rear surface of a specimen in reality (CFRP Specimen of 4.5mm thickness, compare chapter 7.5). There is no distinct T_{max} or t_{max} recognizable.

versus $1/t$. T_0 denotes the initial surface temperature of the specimen before the flash stimulation. The normalization of the temperature (within the square bracket) considers $T(L,t)$ as absolute temperature values of a surface in contrast to T_{model} of equation (4.1a). Therefore $T(L,t)$ is normalized according to the model (compare figure 4.1(a)).

Applied on the model this transformation yields a linearization of the temperature gradient. This is illustrated in figure 4.4. Note that the linearization does not apply for values of $1/t \geq 2.5$ $^1/_s$ (approximately). This excludes just a small number of values which are represented by $t \leq 0.4$ s in the original data space (compare the vertical marks in figure 4.4). Hence, the linearization conforms with most of (and subsequently the most important part of) the data points of the measured data. Note that those numerical values represent the parameters used for the simulation. They will differ for different kinds of specimens and measurements. However, those parts of the data will always account for the same portion of the record, independent of the actual parameters.

Instead of determining a certain point in time, this approach uses the slope of the line to compute the thermal diffusivity. Using this slope the thermal diffusivity can be calculated as [9]

$$\alpha = -\frac{L^2}{4K} \tag{4.7}$$

where

$$\alpha \ldots \text{thermal diffusivity}$$

$$L \ldots \text{sample thickness}$$

$$K \ldots \text{slope of the linearized transformation}$$

(a) Original data from the model   (b) Transformed data
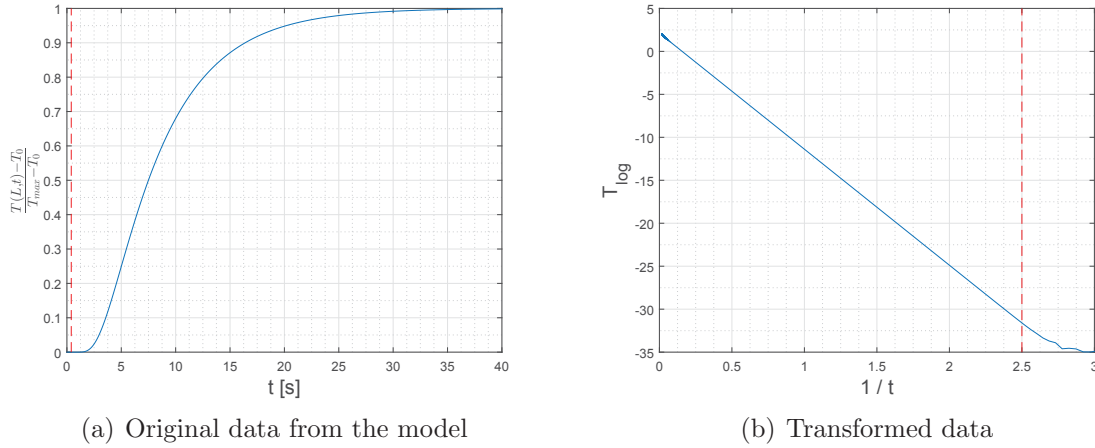
Figure 4.4: Logarithmic transformation of the model. The red dotted lines represent the limit value. The values outside the lower or upper limit can not be used for the computation $(t \leq 0.4\ s)$

This relationship is derived in [2], where we use the physical model of [35] and represent this model by an equation in dependence on [35], which is

$$T(z = L, t) = \frac{Q}{\lambda} \cdot \sqrt{\frac{\alpha}{\pi t}} \cdot 2 \cdot \sum_{n=0}^{\infty} \exp\left(\frac{-L^2 \cdot (2n+1)^2}{4\alpha t}\right) \tag{4.8}$$

where

$$\lambda \ldots \text{thermal conductivity}$$

If we neglect all terms of the sum except for the first one, we receive an equation which is still a practical approach and looks like

$$T(z = L, t) = \frac{Q}{\lambda} \cdot \sqrt{\frac{\alpha}{\pi t}} \cdot 2 \cdot exp\left(\frac{-L^2}{4\alpha t}\right) \tag{4.9}$$

Multiplying by $\sqrt{t}$ and applying the logarithm we receive

$$\log\left(T(z = L, t) \cdot \sqrt{t}\right) = \log\left(2 \cdot \frac{Q}{\lambda} \cdot \sqrt{\frac{\alpha}{\pi}}\right) - \frac{L^2}{4\alpha t} \tag{4.10}$$

which can be transformed to

$$T_{log} = \log\left(T(z = L, t)\right) + \frac{1}{2} \cdot \log(t) = \log\left(2 \cdot \frac{Q}{\lambda} \cdot \sqrt{\frac{\alpha}{\pi}}\right) - \frac{L^2}{4\alpha} \cdot \frac{1}{t}, \tag{4.11}$$

where $T(z = L, t)$ refers to an already normalized temperature profile (compare equation (4.6)). This result can be equated with equation (4.6) and explains the linear shape of the transformed data in form of

$$y = kx + d \tag{4.12}$$

In this linear equation the three components can be expressed as

$$d = \log\left(2 \cdot \frac{Q}{\lambda} \cdot \sqrt{\frac{\alpha}{\pi}}\right) \tag{4.13a}$$

$$k = -\frac{L^2}{4\alpha} \tag{4.13b}$$

$$x = \frac{1}{t} \tag{4.13c}$$

Note that k will be denominated "K" for consistency with the stated methods and x is also the x-axis of the transformed representation. The slope therm K can now easily be transformed to

$$\alpha = -\frac{L^2}{4K} \tag{4.14}$$

which is equal to the result of the stated method, equation (4.7).

As seen in equation (4.6), the maximum temperature is still required to perform the normalization of the temperature gradient. This means an error in the determination of T_{max} still has an influence on the transformed temperature profile, but this influence manifests as a shift of the line along the y-axis while the slope remains the same. In consequence, T_{max} needs to be measured to calculate α, but it does not affect the result. The relationship between different T_{max} and the transformed data is illustrated in figure 4.5.

4.2.3 Comparison of the Two Methods

The two methods described in the previous sections are tested on their robustness against varying minimum and maximum temperatures. Those variances occur during real measure-
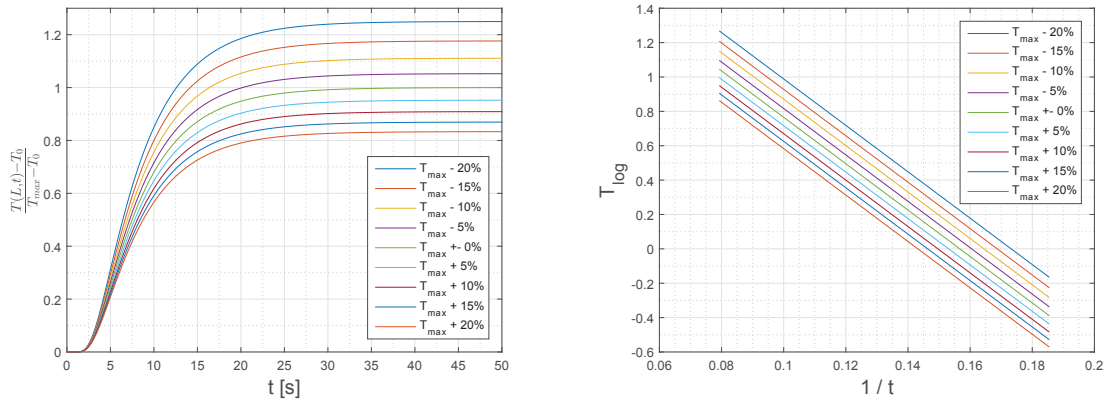
(a) Influence of a T_{max} variation on the original data

(b) Influence of a T_{max} variation on the transformed data

Figure 4.5: Comparison of the Influence of a T_{max} variation on the data before and after the transformation.

ments because of errors in measurement due to noise and because of the violation of the adiabatic preconditions (heat dissipation in real measurements).

The comparison of the two methods is presented in figure 4.6. First of all it is to notice, that both methods reconstruct the thermal diffusivity very well when T_{max} and T_0 are known exactly.
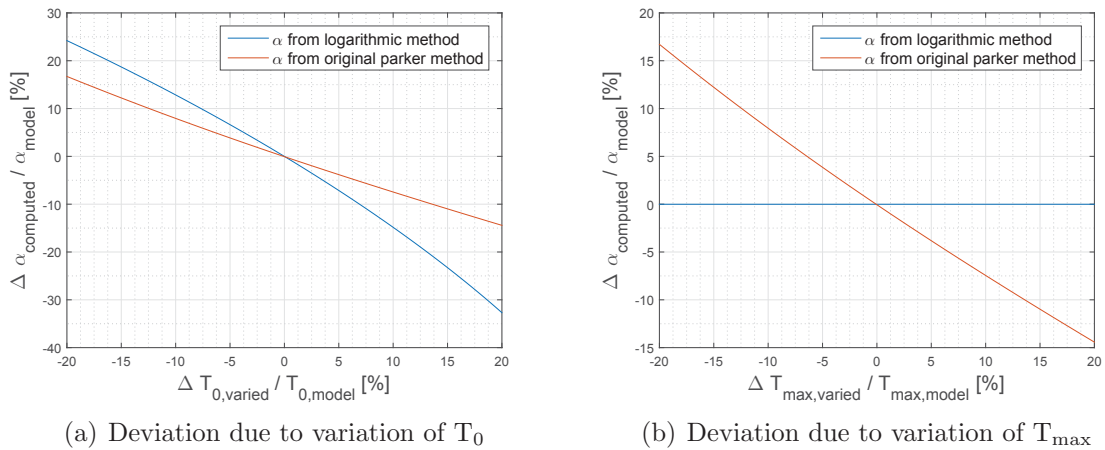
(a) Deviation due to variation of T_0

(b) Deviation due to variation of T_{max}

Figure 4.6: Comparison of the two evaluation methods. (a): Variation of T_0 from 80% to 120% of the actual T_0 in the model. (b): Variation of T_{max} from 80% to 120% of the actual T_{max} in the model.

From the previous sections it was to expect that an error in the T_{max} determination has no influence on the computation using the logarithmic method. In contrast to this method, the original Parker's method yields a calculation error depending on the size of the measurement error.

An error in the T_0 measurement yields deviation in the thermal diffusivity for both methods, although the logarithmic method is more sensitive to such an error. Aberrations of T_0 should not be very high since the temperature on the surface before the flash light is constant and the noise can be cleared by averaging.

Thus, the logarithmic method seems to be more suitable for determining the thermal diffusivity of a specimen. For a comparison of the two methods on real specimens see chapter 7.2.

4.3 Measurement in Reflection Mode - TSR

The method presented in this section is highly geared to the approaches presented in [26] and patented in [23].

The temperature on the front surface decreases till it reaches a (temporarily) constant "plateau" (according to [18]). This behavior can be seen in figure 4.1(b). This figure shows, that the temperature converges to the end temperature in a curve. Through this, no distinct point in time where the temperature stops decreasing is determinable, as it is in the transmission measurement. Therefore, the relevant point in time t_w is defined as the intersection of the linear part of the temperature decrease and the constant end temperature, see figure 4.7.
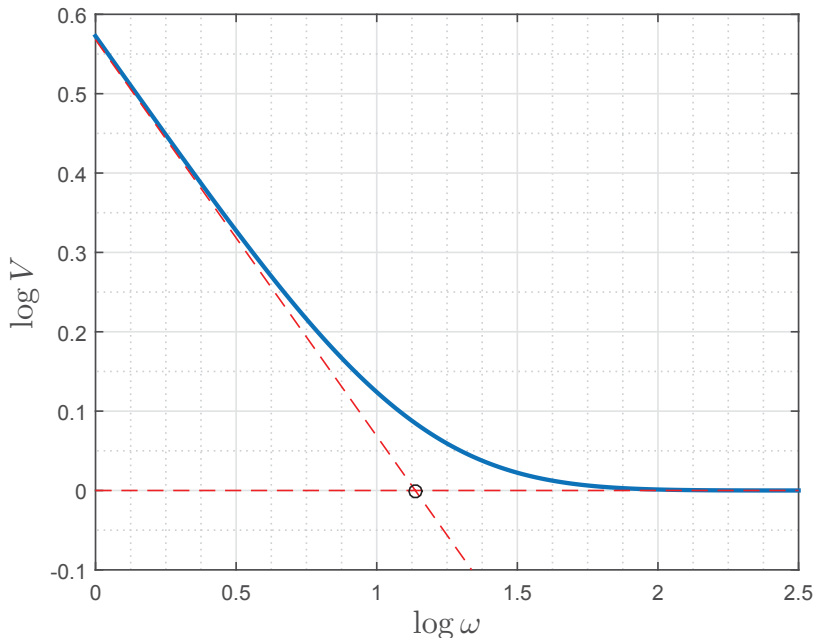
Figure 4.7: Definition of t_w

To describe this relation mathematically ([2]) we use the first part of equation (4.8), which

is

$$T_{SB} = \frac{Q}{\lambda} \cdot \sqrt{\frac{\alpha}{\pi t}} \tag{4.15}$$

This equation describes the temperature decrease in a semi-infinite body ("SB") and therefore represents the decreasing line in figure 4.7.

The end temperature is described by the equation (4.2). By using the relation from equation (2.2) we can transform equation (4.2) into the form

$$T_{end} = \frac{Q}{\lambda} \cdot \frac{\alpha}{L} \tag{4.16}$$

To compute the point of intersection we use the equations (4.15) and (4.16) as

$$T_{end} = T_{SB} \tag{4.17a}$$

$$\frac{Q}{\lambda} \cdot \frac{\alpha}{L} = \frac{Q}{\lambda} \cdot \sqrt{\frac{\alpha}{\pi t}} \tag{4.17b}$$

and transform this result into

$$t_w = \frac{L^2}{\alpha \pi} \tag{4.18}$$

This point of intersection coincides very well with the maximum curvature of the temperature profile. Figure 4.8 illustrates the derivatives of the profile of the model (figure 4.7), together with the defined t_w. This relationship will be used to determine t_w within temperature profiles of measured data (and will be explained in detail in section 5.3.2).

(a) 1st derivative   (b) 2nd derivative
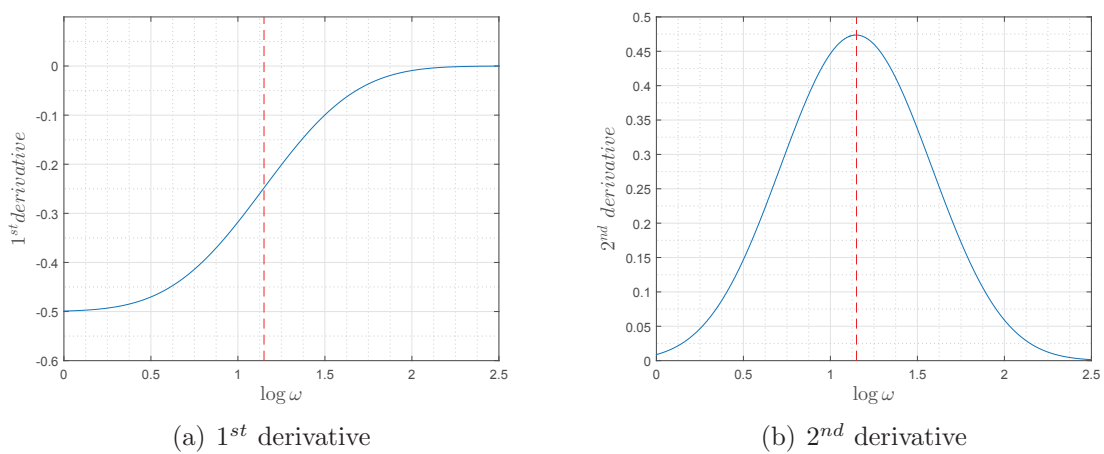
Figure 4.8: Derivatives of the temperature profile of the model. The red dotted line represents t_w as defined previously (compare figure 4.7 and equation (4.18)).

As soon as t_w is determined, the thermal diffusivity or the thickness of the material can be calculated as

$$\alpha = \frac{L^2}{t_w \cdot \pi} \tag{4.19a}$$

$$L = \sqrt{t_w \alpha \pi} \tag{4.19b}$$

Note that the significant time value in transmission mode $t_{1/2}$ is related to t_w by a constant factor as [5]

$$t_w = \frac{\pi}{1.37} t_{1/2} \approx 2.27 t_{1/2} \tag{4.20}$$

If a defect with finite lateral extension, which influences the thermal diffusivity, is located within the material, the temperature profile of a point on the surface above this defect differs from the model described, see figure 4.9. This figure shows the temperature profile of points on the surface of a simulated specimen, whereat every solid line represents the temperature profile of a pixel above a defect.
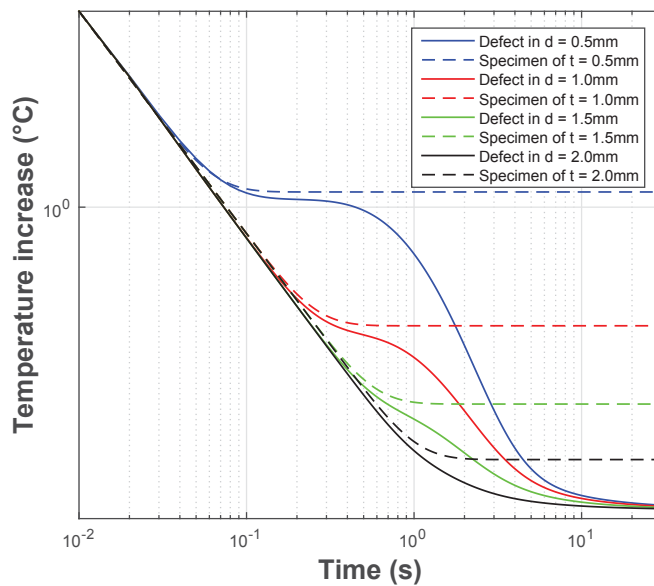
Figure 4.9: Example of a number of temperature profiles of pixels over defects in different depths [5]. The profiles in this example have been derived in an ANSYS simulation computing a specimen of 2.5mm thickness with cylindrical defects of a diameter of 10mm in different depths. The dashed lines represent a theoretical function of specimen of certain thickness with infinite extension.

When the heat diffuses through the material and reaches the defect, it accumulates in

front of the defect, just as it does at the rear surface of the specimen. Therefore, the curve bends up and forms a plateau. Since the heat flows through and around the defect after a while, the temperature profile declines again and forms another decrease. As soon as the heat reaches the rear surface of the material, the temperature profile merges with the profile of a flawless surface point to a constant plateau. Note that the temperature at this "constant" plateau decreases as well because of non adiabatic environmental conditions. In case of very short records with high frequency the influence of this decrease on the data is very small. In case of very long records the influence on the result is relatively high and must therefore be considered. This problem is investigated in more detail in the following chapters.

The effect, which causes the heat to accumulate in front of the defect is the same effect which leads to the temperature plateau at the rear surface of the material. Consequential the equation to calculate the thickness of the material can be used to compute the depth of the defect, if t_{w} at the corresponding plateau is determined. Using equation (4.19b) the defect depth then yields

$$d_{defect} = \sqrt{t_{w,defect}\alpha\pi} \tag{4.21}$$

4.4 Measurement in Reflection Mode - PPT

The PPT evaluation is described in dependence on [38]. Equivalent to the reflection measurement using the TSR technique, in PPT a thermal pulse is applied to the specimen - in our case by using a flash light. According to [19] every (periodical) signal can be represented by the sum of sinusoidal signals. Thus, the thermal pulse can be fractionized into sinusoidal waves of different frequencies. According to [38] the frequencies which can be obtained from the analysis are defined by

$$f_n = \frac{n}{N\Delta} \tag{4.22}$$

where

$$N \text{ ... Number of thermal images, } N = t_{Record} \cdot f_{Record}$$

$$\Delta \text{ ... interval between thermal images, } \Delta = \frac{1}{f_{Record}}$$

$$n \text{ ... } 0,1,...,\frac{N}{2} \text{ since the Fourier transformation yields a}$$

positive and negative spectrum

The following (artificially modelled) examples are supposed to illustrate those relationships (in dependence on [14]). All those cases use the same boundary conditions, which are

$$t_{Record} = 10s$$

$$f_{Record} = 100Hz$$

$$\Delta = \frac{1}{f_{Record}} = \frac{1}{100} = 0.01$$

$$N = t_{Record} \cdot f_{Record} = 10s \cdot 100Hz = 1000$$

$$n = 0, 1, ..., 500$$

$$f_n = \frac{n}{N\Delta} = \frac{0, 1, ..., 500}{1000 \cdot 0.01} = 0, 0.1, ..., 50Hz$$

Note that these frequencies occur in the positive and negative spectrum.

The composition of amplitudes of those frequency components highly depends on the length of the thermal pulse. Figure 4.10(a) illustrates a thermal pulse of infinite short duration. This represents an ideal Dirac pulse.

(a) Pulse in time domain   (b) Pulse in frequency domain
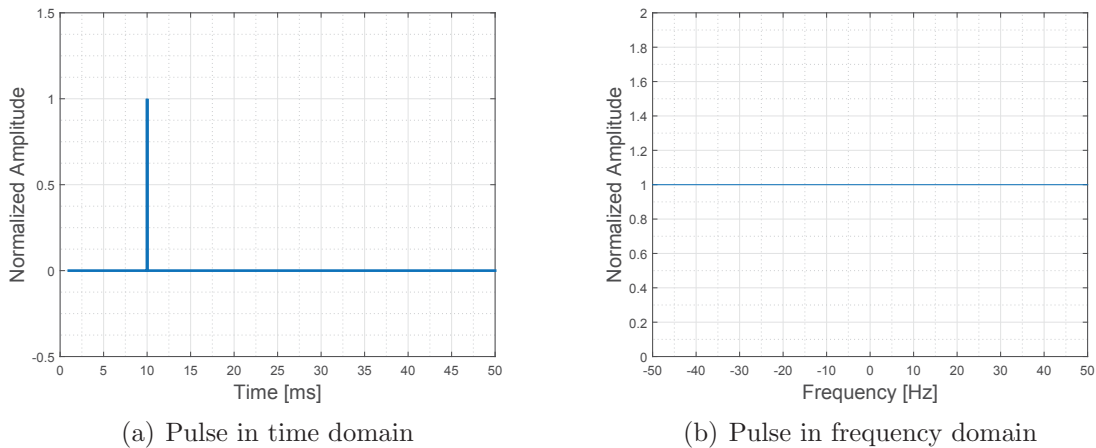
Figure 4.10: Ideal thermal pulse of infinite short duration for a measurement duration of 10s and a recording frequency of 100Hz.

Such a pulse can now be fractionized using a Fourier analysis. This is done using MATLAB's *fft* function. This function computes a Fast Fourier transformation of a given signal.

As figure 4.10(b) illustrates, such an ideal Dirac pulse yields the same amplitude for every frequency contained in the frequency spectrum of the Fourier analysis. As mentioned previously, the thermal pulse resulting from the flash light is not of infinite short time and consequently does not correspond with an ideal Dirac pulse (compare therefore section 3.5).

Thus, the result of the Fourier analysis will look differently. Figure 4.11 illustrates two non ideal thermal pulses of different time duration.

The following statements can be derived from this figure:

The amplitudes of the specific frequencies vary with the pulse duration. Longer pulses yield higher amplitudes, especially for low frequencies. This corresponds with a higher energy input into the specimen by a longer pulse. Higher amplitudes are desirable because the higher energy will increase the signal-to-noise ratio. Furthermore, high energy is needed for the thermal waves to move through the entire specimen and therefore to detect deep defects. Thus, since highest amplitudes can be expected at low frequencies, focus will be laid on those frequency components.

4.5 Record Length Estimation

If one wants to perform a measurement and an evaluation according to the approach presented in this work, one needs to choose the record length for the IR-camera long enough so that the important data is recorded, while one wants to hold this record length as short as possible to reduce file size and computational effort for the evaluation.

To estimate the ideal record length, a virtual heat flow end according to the analytical model was defined as

$$\omega_{RecordEnd,Transmission} = 6 \tag{4.23a}$$

$$\omega_{RecordEnd,Reflection} = 13.6 \tag{4.23b}$$

for transmission and reflection mode, respectively. Note that those values have been chosen with respect to the relation described in equation (4.20).

At those points in time the temperature increase in transmission mode is about 99.5% of the total increase and the temperature decrease in reflection mode is basically completed (end temperature is reached). This correlation is illustrated in figure 4.12.

Since ω is a dimensionless parameter, the actual recording time can be computed using equation (4.3b) and the specimen parameters α and L as

$$t_{RecordEnd} = \frac{\omega_{RecordEnd} L^2}{\pi^2 \alpha} \tag{4.24}$$

For the two different modes, this yields
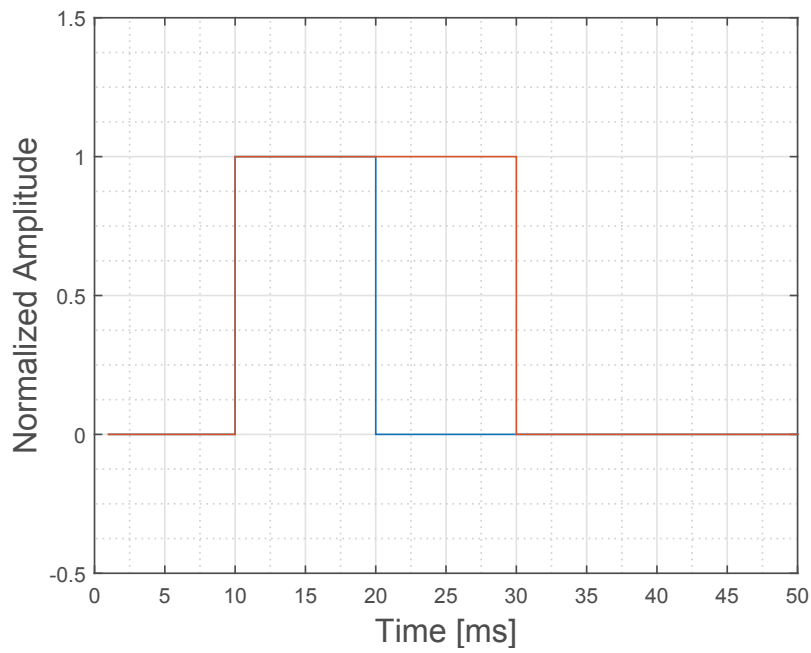
(a) Pulse in time domain
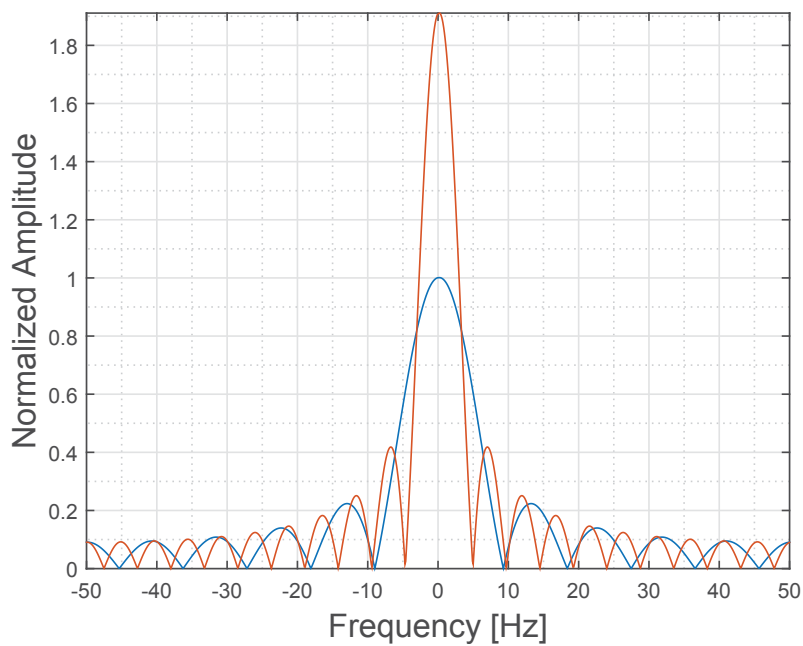
(b) Pulse in frequency domain. Note: The amplitude of the longer pulse is normalized with respect to the amplitude of the short pulse to demonstrate the amplitude ratio of different pulse durations.

Figure 4.11: Non-ideal (real) thermal pulses with a duration of 10ms and 20ms, a measurement duration of 10s and a recording frequency of 100Hz.

(a) Transmission Mode   (b) Reflection Mode
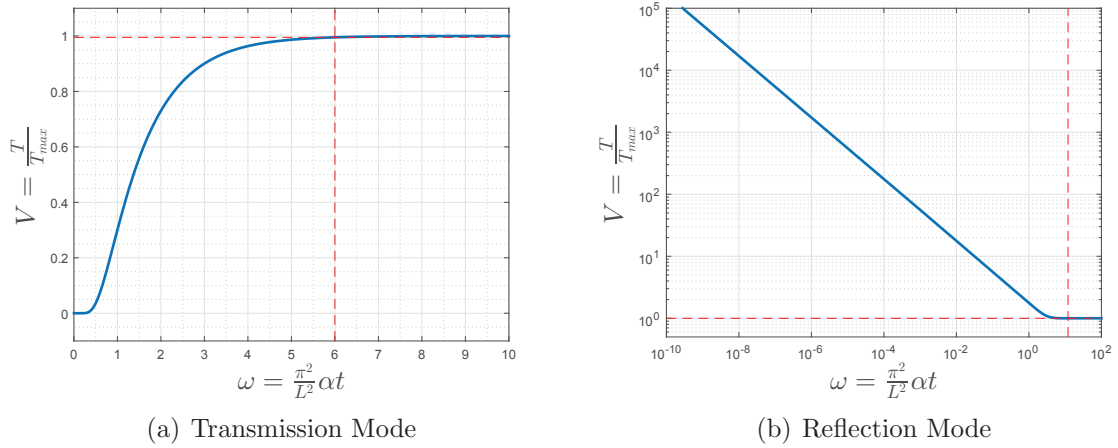
Figure 4.12: Estimation of the ideal record length.

$$t_{Transmission} = \frac{6L^2}{\pi^2 \alpha} \tag{4.25a}$$

$$t_{Reflection} = \frac{13.6L^2}{\pi^2 \alpha} \tag{4.25b}$$

Table 4.1 provides an overview of some examples for required recording duration depending on material and thickness.

Material	$\alpha \; [m^2/s]$	Thickness $[mm]$	$t_{Transmission} \; [s]$	$t_{Reflection} \; [s]$
		1	0.0715	0.162
Steel	$8.4966 \cdot 10^{-6}$	4	1.14	2.60
		10	7.15	16.2
		1	0.500	1.14
CFRP	$1.2153 \cdot 10^{-6}$	4	8.00	18.2
		10	50.0	114
		1	0.00540	0.0122
Copper	$1.1249 \cdot 10^{-4}$	4	0.0864	0.196
		10	0.540	1.22
		1	0.00495	0.0112
Aluminum	$1.2271 \cdot 10^{-4}$	4	0.0792	0.179
		10	0.495	1.12
PLA - Polylactic Acid		1	4.82	11.0
(3D Printer Plastic)	$1.26 \cdot 10^{-7}$	4	77.2	175
		10	482	1095

Table 4.1: Examples of required recording duration for different materials with different thickness.

5 Data Processing

5.1 Influence of the Flash

5.1.1 Problems of Flash Thermography

The flash light contains high energy and therefore the camera sensor is saturated by IR light from the flash lamp, reflecting surfaces in the surrounding of the specimen or reflections on the specimen itself. The saturation yields a corruption of the camera sensor output for a certain time span. Using data with such a corruption in the evaluations yields corrupted results. Therefore, t_{Flash} as well as the point in time when the influence of the flash is fully abated - t_{EoF} (**E**nd **o**f **F**lash) - need to be determined to ensure a proper evaluation. The procedures to handle this determination are presented in the following sections.

Furthermore, flash thermographic inspections are afflicted with some specific problems according to [36]:

- The results of a thermographic evaluation can be highly affected by the position of the flash lamp with respect to the specimen.

- "The heating from a single lamp will be non-uniform, peaking at the center" [36]. This problem could in fact be observed in numerous measurements executed for this work. [36] suggest to use multiple flash lamps (two or more). However, the used experimental rig was limited to only one flash lamp and a heating as uniform as possible was gained through proper positioning of the sample with respect to the flash lamp (especially the distance between flash lamp and specimen).

- Parts of the lamp tend to emit IR light for a significant time span after the actual flash light (lamp after glow). This emitted light can be detected by the camera directly or through reflections, which accordingly yields corruption of the data and the evaluation result. According to [36] this is problematical especially for specimen with very short thermal response times, such as thin metal parts. This problem was very well observed during the experiments and will be addressed later in the text. It can partially be reduced using the techniques for shortening the influence of the flash, presented section 5.1.3.

- "The optical characteristics of the surface of the material or its coating heavily impact the results of the inspection. Many materials for example are translucent, i.e. light is absorbed in them over a range of depths (and consequently the heat source obtained by flash excitation is not confined to the surface; it is distributed over a range of depths), but their optical absorption coefficients are not readily available." [36]

5.1.2 Localizing Flash in the Record

To start the evaluation, t_{Flash} has to be localized within the recorded temperature response. Therefore, the temperature profile of a number of pixels, which are selected automatically (no user input necessary) and distributed equally in the middle of the camera window (black marks in the example in figure 5.3), are extracted from the record. The average of those profiles is computed and used for further processing. Tests have been conducted, where, instead of a small number of pixels, a range of about 20×20 pixels in the middle of the record frame have been used for calculating the average value. The influence of this approach on the t_{Flash} determination turned out to be marginal, the mentioned small number of pixels proved to be sufficient to localize t_{Flash}. An example of such an averaged temperature profile is shown in figure 5.1(a) (Note that this example was taken from a measurement in transmission mode. However, the procedure for the flash detection in reflection mode is the same). The gradient of this profile is computed (see figure 5.1(b)) and t_{Flash} is localized as the maximum value in the gradient, since the flash saturates the camera sensors entirely in a matter of millisecond. This extremely quick intensity gain yields a very high gradient which marks the flash.
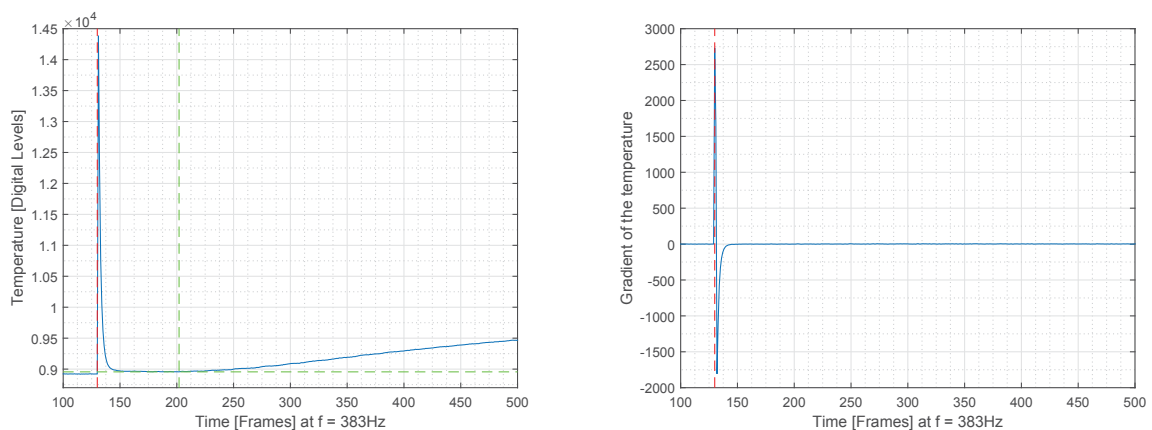
(a) Temperature profile, flash (t_{Flash}) (red) and end of influence (t_{EoF}) (only for transmission measurements, green) marked.

(b) Gradient of temperature profile, flash (t_{Flash}) marked

Figure 5.1: Determination of t_{Flash} and t_{EoF} (in transmission mode) within the data.

5.1.3 End of Flash Influence

The impact of the camera detector saturation shall be explained for the case of a transmission measurement (although problems also arise in case of reflection measurements): The time span including the significant data from t_{Flash} to t_{max} is partially overlapped by detector saturation through the flash light from t_{Flash} to t_{EoF}. Since the time span from t_{Flash} to t_{max} decreases with thinner specimens while the saturation from t_{Flash} to t_{EoF} remains constant, the data evaluation becomes more difficult with thinner samples (time profiles of specimen of different thickness are illustrated in the example in figure 5.4). This specific problem is investigated further in section 5.2.1.

To reduce the overlapping and increase the analyzable time span two approaches were figured out:

- Glass plates in front of the flash lamp block radiation in the IR-spectrum (compare figure 3.4), while they are still permeable for radiation in visible spectra. Through this, the infrared light, which saturates the camera sensor during the flash, can be reduced. Additionally, such a modification also reduces influences of the after glow effect.

- In case of transmission measurements, the camera can be shielded from the IR-radiation of the flash light by means of a light shade around the specimen (compare figure 3.4). Such a light shade was designed and tested. The overlapped time span could thus be reduced from several hundreds of milliseconds (highly depending on the observed pixel) down to 20-30ms.

Furthermore, t_{EoF} can be determined in two ways:

- **Global determination:** A number of pixels (some pixels spread across the record frame or a range of pixels in the middle of the frame) are extracted from the record and averaged. t_{EoF} is then computed for this averaged temperature profile and used for every pixel in the record.

- **Local determination:** t_{EoF} is computed for every single temperature profile of every pixel in the record. Thus, different t_{EoF} values for different pixels are possible.

5.1.4 Using Lock-in Signal for Flash Detection

For better flash detection the test rig was modified. The PLC was connected to the camera on its "Lock-in" port. The control applies a constant voltage to this port. When triggering the flash generator by pulling the voltage on the generator input to ground, it also sets the voltage on the cameras Lock-in port to a higher (but still constant) voltage. The camera

records this voltage together with every image frame during the record. t_{Flash} is therefore determinable as the highest gradient of this voltage profile. The advantage of this method of flash detection is that the above-named evaluation step can be omitted and replaced by a significant simpler algorithm. Figure 5.2 shows a lock-in signal profile compared to the related averaged temperature profile for a measurement in reflection mode.
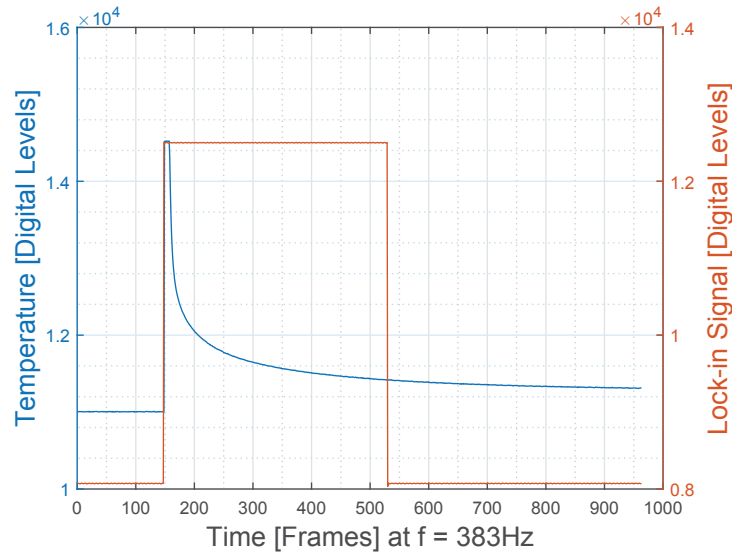
Figure 5.2: Lock-in signal for flash detection. Note that the computed t_{Flash} occurs at frame 149 while the flash signal from the lock-in occurs at frame 148.

However, experiments showed that the lock-in signal does not entirely correlate with the actual recorded temperature profile. The gradient peaks of lock-in and the temperature are slightly out of alignment. This deviation does not exceed one image frame for most measurements. The shift only occurs at higher recording frequencies, at lower frequencies the signals (the peaks in the gradient of temperature and lock-in signal respectively) align for most measurements. Those shifts can be related to the reaction time of the system parts PLC - relay - flash generator - flash and is basically not capable of being influenced.

Since the correct t_{Flash} determination is an important requirement for the correct computation of significant times in the record, those shifts yield deviations in the results. For example, at a recording frequency of 383Hz, a shift of one frame would result in a deviation 2.6ms. For specimens with a high thermal diffusivity, this shift represents a significant measurement error. Those shifts do almost not occur at lower frequencies, but if they do, the measurement error is way higher (for example: one frame at a frequency of 10Hz would yield an error of 100ms).

Thus, the method of flash detection using a lock-in signal was considered to be not sufficiently accurate. The determination is performed by the procedure described in the previous section.

5.2 Measurement in Transmission Mode

5.2.1 Local End of Flash Determination

The localization of t_{EoF} is done by localizing the minimum temperature in the (smoothed) temperature profile between t_{Flash} and the end of the record, compare figure 5.1(a). t_{EoF} was originally determined by a global evaluation. This is suitable for most of the measurements but problems can occur in boundary areas or if the investigated specimen consist of very different thicknesses or thermal diffusivities. This problem becomes evident in the case of the CFRP specimen used for the experiments described later in chapter 7.1.

To demonstrate this, figure 5.3 shows the mentioned specimen. Points on the surface are marked which have been used for a global t_{EoF} determination (black points) as well as one point for each layer combination.
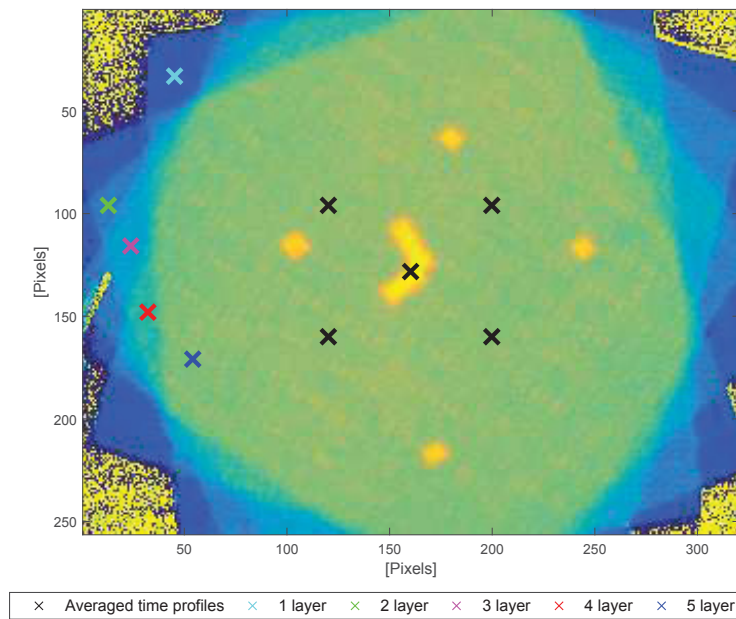
Figure 5.3: CFRP specimen: The marked points are chosen over different layers to extract the time profile of those pixels from the record.

The time profiles according to the chosen points are plotted in figure 5.4 (in the particular colors according to figure 5.3). The solid lines represent the time profiles, the vertical dashed lines represent the end of the flash influence t_{EoF}. It is obvious, that the point in time determined from the averaged time profile can not be used for every single pixel. For example: The time profile for 1 layer reaches the maximum temperature before the evaluated t_{EoF} of the averaged pixels; The time profile for 2 layers exceeds at least half of its temperature

increase before the averaged t_{EoF}.
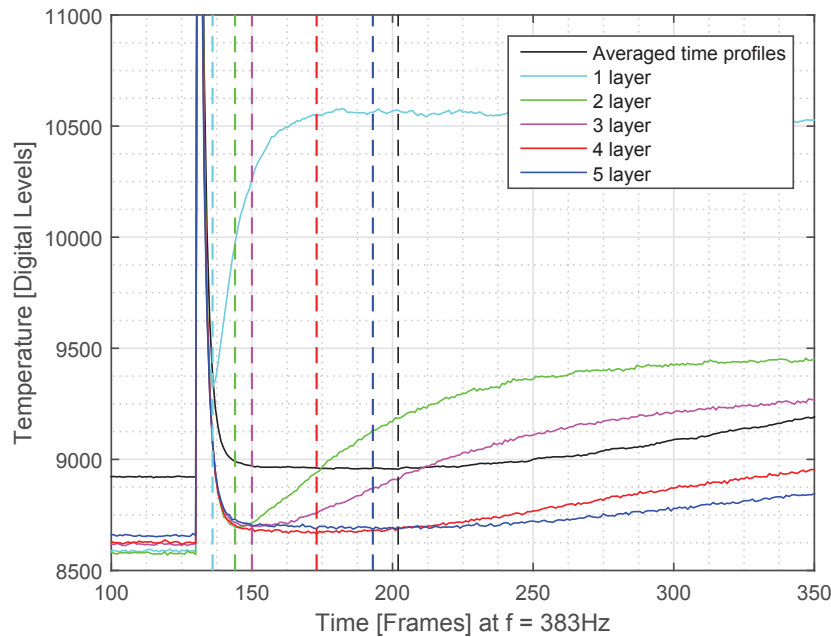
Figure 5.4: Time profiles of the chosen points above different number of layers.

Therefore, the procedure was adapted so that t_{EoF} is computed locally.

Note: Despite this modification, t_{Flash} is still determined for the whole record and not just for each pixel separately. This is necessary to get a global time stamp for the flash to reference measured time values of every pixel to the same level.

5.2.2 Parker's Method

The evaluation according to Parker's method described in chapter 4.2.1 is executed in the time domain for every pixel separately. The result of this evaluation ($t_{1/2}$ for every pixel) is then stored in two-dimensional matrices where every entry represents the computed value for the particular pixel. This result can then be illustrated as a picture.

First, the significant temperatures within the time profile need to be determined. Those temperatures are:

- **T_0:** The start temperature is calculated as mean value of all temperatures between the beginning of the record and t_{Flash}.

- **T_{max}:** To find the maximum temperature, the time profile is extracted from t_{EoF} to the end of the record and smoothed using MATLAB's *smooth* function [39]. This function computes a moving average with a span of five by default. T_{max} is then determined as the maximum of the smoothed extraction.

- **T$_{1/2}$:** The significant temperature increase is simply calculated as half of the increase between T$_0$ and T$_{max}$.

An example of the extraction of such boundary values is given on a real measurement result in figure 5.5.
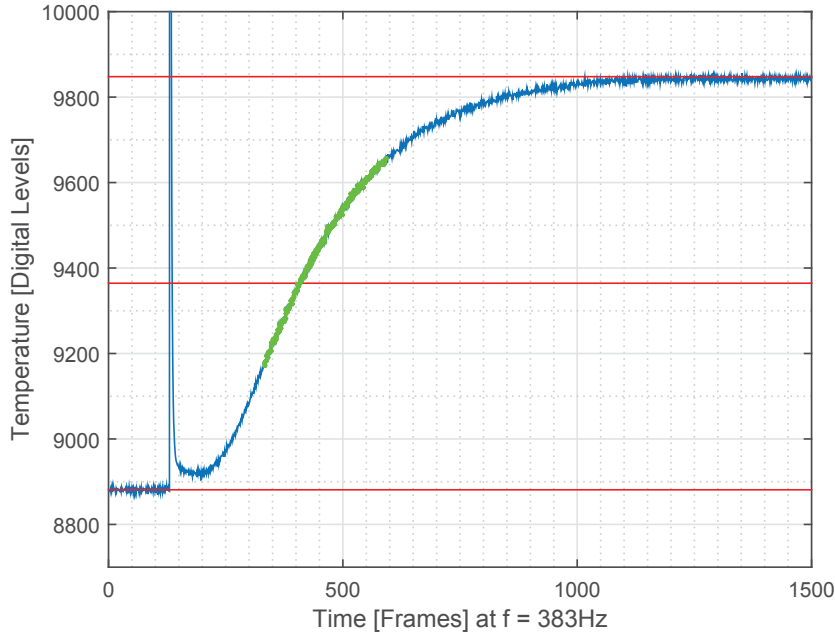
Figure 5.5: Example of the data preparation for Parker's method: Significant temperatures as red lines and the extracted data points for further computation as green dots (between approx. 9200 and 9700 digital levels). This data was gathered from a measurement of a steel plate of 8.6mm thickness (specimen described in chapter 7.2).

Since we want to find a data point within the temperature increase, we neglect data before and after the relevant increase period. Additionally, by using only data points of a steady increase, the polynomial fitting and therefore the time determination becomes more stable. Thus, a part of the data points which includes the significant data, is extracted from the temperature profile. A reasonable range for this data extraction was found to be 30% of $\Delta T = T_{max} - T_0$ to 80% of ΔT. This approach was adopted from [9], where it is used within a logarithmic evaluation (described in the following section). This extracted range compared to the actual data is illustrated in figure 5.5.

A polynomial of degree 4 is fitted to the extracted data points (compare figure 5.6). This polynomial is then evaluated at the temperature T$_{1/2}$ which yields the significant point in time t$_{1/2}$.

Since the polynomial is fitted only to a small section of the data, the result must be referred to t_{Flash}. Through this the measured times agree with the analytical model from chapter
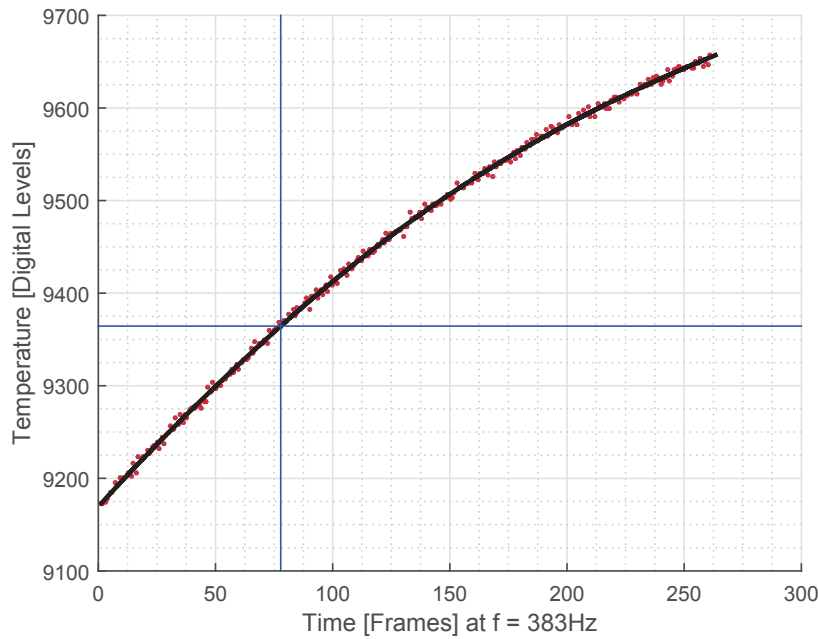
Figure 5.6: Example of the $t_{1/2}$ evaluation in the extracted data range: Data points as red dots, fitted polynomial as black line and $T_{1/2}$ and $t_{1/2}$ as blue lines. Time space is shifted compared to the original data because of the range extraction.

4.1. Additionally, to avoid outliers due to bad data (for example in the border area of the camera window which only shows the surrounding area, not the specimen itself), upper and lower limits for $t_{1/2}$ are defined. Those limits are t_{Flash} as lower limit and t_{max} as upper limit (since $t_{1/2}$ can not lie outside of these limits).

There are two different parameters which can be computed using the calculated $t_{1/2}$. Those are

- **Thickness L** of the specimen or different thickness levels of different areas of the specimen, assuming a known and homogeneous thermal diffusivity or

- **Thermal diffusivity α** of the specimen or different α values of different areas of the specimen, assuming a known and homogeneous thickness.

Those values are calculated using the relationship represented by equation (4.5) as

$$L = \sqrt{\frac{\alpha \pi^2 t_{1/2}}{1.37}} \tag{5.1a}$$

$$\alpha = \frac{1.37 L^2}{\pi^2 t_{1/2}} \tag{5.1b}$$

5.2.3 Logarithmic Method

This section is based on the approach presented in [9]. The principle of the evaluation according to the logarithmic method is very similar to the one used for the Parker's method. Again, the temperature profile of every pixel is processed separately, T_0 and T_{max} are determined in the same manner and a range between 30% and 80% of ΔT is extracted [9]. Calculations on the simulated data from chapter 4.1 revealed, that a change in this range influences the stability of this evaluation in terms of T_{min} variations, compare chapter 4.2.3 and figure 4.6(a). Furthermore, increasing the extraction range increases the error in figure 4.6(a), while a smaller range yields a smaller error compared to Parker's method. Since a range from 30% to 80% is relatively large, we probably don't need to increase this range at any time. Thus, changing (reducing) the size of the range will only decrease the error.

The extracted data is transformed as described in chapter 4.2.2 using equation (4.6). The transformed data range is illustrated in figure 5.7.
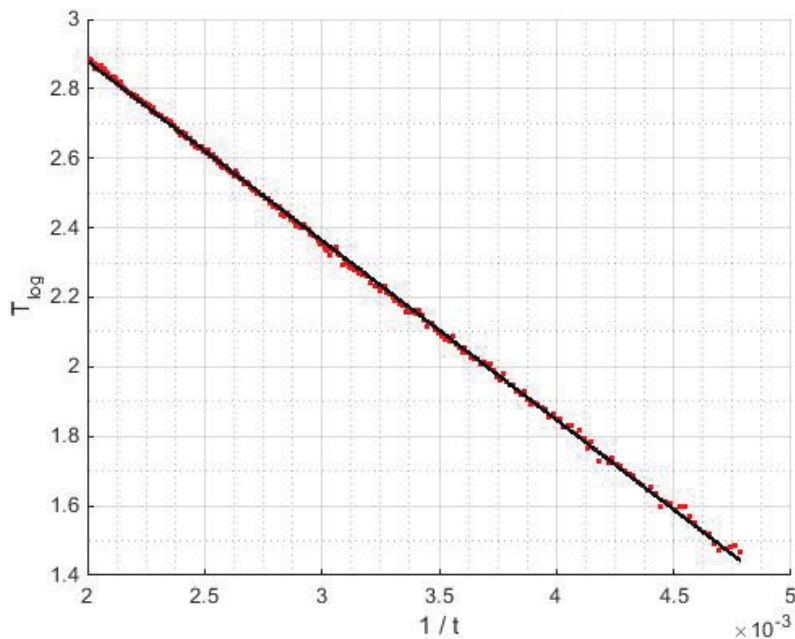
Figure 5.7: Example of the slope evaluation of the transformed data: Data points as red dots, fitted regression as black line.

A linear regression is fitted to the transformed data using MATLAB's *regression* function [39]. This yields the slope K for the line. Using this slope we can calculate the thickness L or the thermal diffusivity α of the specimen (as shown in the previous section 5.2.2), depending on the given parameters. Using equation (4.7) we can compute those values as [9]

$$L = \sqrt{-4\alpha K} \tag{5.2a}$$

$$\alpha = -\frac{L^2}{4K} \tag{5.2b}$$

5.3 Measurement in Reflection Mode - TSR

5.3.1 End of Flash Determination

In reflection mode the temperature decrease of the surface needs to be measured. Due to this, the approach to find t_{EoF} differs from the method presented in chapter 5.2.1, since the decreasing temperature of the surface and the shrinkage of the flash influence overlap while those effects in transmission mode are contrariwise. A minimum in the temperature profile does not mark the end of the influence.

The chosen procedure is to subtract the initial temperature from the whole temperature profile first as well as to omit all data before t_{Flash}. Subsequently, the profile is transformed into double logarithmic space (compare therefore section 4.3). Figure 5.8(a) shows this transformed temperature profile. The camera saturation due to the flash light is very well visible at the left end of the profile. To find t_{EoF}, the gradient of the temperature profile is computed, see figure 5.8(b). As demonstrated in figure 4.8(a) in the previous chapter, this gradient (or the first derivative, respectively) should start at a value of -0.5. However, figure 5.8(a) illustrates, that the gradient is lower than -0.5 directly after the full camera saturation and successively rises to this expected value. The reason for this could be the abating flash light. Furthermore, the logarithmic scaling is very sensitive to the chosen or determined t_{Flash}. Variations in this value will shift the data along the x-axis of the plot and, due to the logarithmic scaling, highly influence the gradient at the begin of the profile. Thus, the point in time when the gradient reaches -0.5 needs to be found to determine t_{EoF}.

The algorithm finds the most negative value within the gradient to start the search for the first point in time when the gradient exceeds a specified limit k_{EoF}. Although this limit should be -0.5, the value was chosen as -1, since noise in the data can distort the gradient to values less than -0.5, although the influence of the flash is already abated. The red lines in figure 5.8(a) and figure 5.8(b) illustrate this point in time and represent therefore the determined t_{EoF}. Note that the noise at the end of the temperature profile yields high noise in the gradient (compare figure 5.8(b)) which impedes the determination of the most negative value in the gradient. Therefore, only data to a certain point in time is used to determine this most negative value. This point in time was chosen as 0.5 seconds, since this time span should be long enough for the flash influence to abate but short enough to exclude the high

gradient values due to noise. This point in time is represented by the black dotted line in figure 5.8(b).

(a) Temperature profile

(b) Gradient of the temperature profile
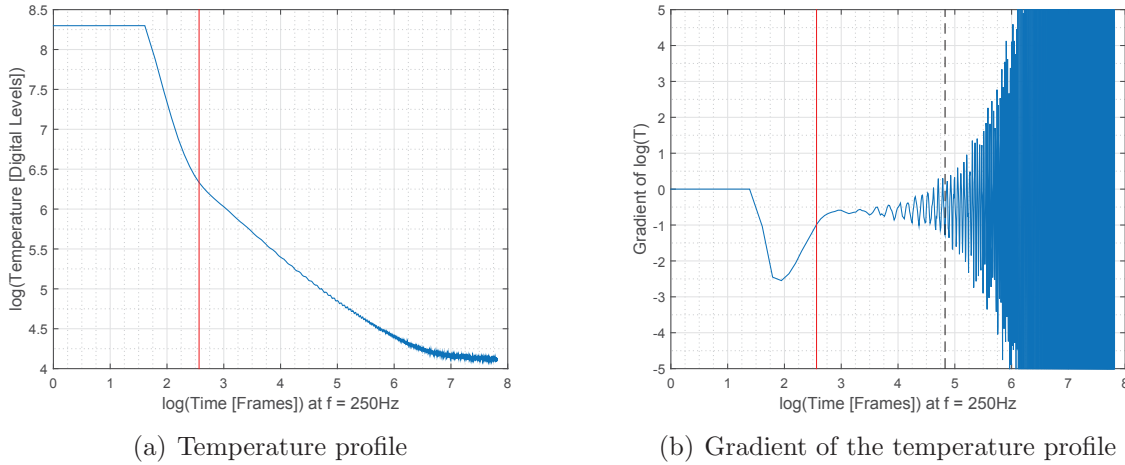
Figure 5.8: Example of a t_{EoF} determination: The black dashed line represent the time span which is used for determination, the red solid line represents the determined t_{EoF}

Two different methods of polynomial fitting are presented in the following sections. The first one computes all polynomials and t_w values locally, while the second one uses a global computation approach. Thus, also the t_{EoF} determination is executed locally in case of the first method and globally in case of the second one. To reduce noise within the data, the gradients of the temperature profiles are smoothed in both cases. In case of local determination the profile is smoothed along the time axis using MATLAB's *smooth* function, in case of global determination t_{EoF} is determined in a temperature profile which is averaged from 20×20 profiles in the middle of the recording window. This can yield different results for t_{EoF}, which will be presented in detail later.

5.3.2 Determining t_w through polynomial fitting

The method presented in this section is highly geared to the approaches presented in [26] and patented in [23].

To localize this defined point in time, a polynomial of degree n_{poly} is fitted to the temperature profile in double logarithmic scale. Alike the t_{EoF} determination, the initial temperature is subtracted from the data. Furthermore, only data after t_{EoF} is considered for the following computations and evaluations. The fitted polynomial can subsequently be differentiated to find the maximum in the second derivative. The polynomial fitting is also necessary to handle measurement data with noise, otherwise it could not be derived (compare [23] and [4]).

The result of this approach highly depends on the chosen degree n_{poly} of the fitted polynomial. Figure 5.9 illustrates the original temperature profile (from the model) and the second derivative of polynomials of different degree fitted to the temperature profile.

Those results indicate that a polynomial of degree $n_{poly} = 8$ approximates the intersection point best. However, a big disadvantage of the usage of a polynomial of such high degree is that it is very unstable, which means that the high degree yields multiple maxima in the derivatives. This complicates the maximum detection of the second derivative. On the other hand, we need a certain minimum as a polynomial degree to represent data of a certain form. Sloppy speaking, we need one additional degree for every straight line within the data. If one considers figure 4.9, a degree of a minimum of $n_{poly} = 4$ (four straight lines) is necessary to represent temperature profiles of material including defects [31]. Generally speaking, polynomials of lower degree are more stable, those of higher degree are superior in reducing the error between the polynomial and the actual data. This last point is especially important when using real data, which tends to differ from the model illustrated in figure 5.9, especially at the beginning and at the end (this problem will be investigated further in the next sections, especially in section 5.3.4). Thus, when choosing a degree for the polynomial fitting, a trade-off between stability and error minimization must be done.

In the following sections two procedures to fit a polynomial to the data are presented. The first one uses MATLAB's *polyfit* function, the second one is an approach which uses discrete orthogonal polynomials (DOP) with constraints. This second possibility to fit a polynomial uses principles developed by [30]. Finally, the process to find and determine the correct maximum in the second derivative of the polynomial (for both fitting approaches) is presented.

5.3.3 Polynomial Fitting Using MATLAB's polyfit

MATLAB's *polyfit* function fits a geometrical polynomial to given points through a least-squares minimization [39]. The chosen degree of this polynomial is $n_{poly} = 5$. Although figure 5.9 identifies this degree to represent the modelled data badly compared to other degrees, experiments revealed this degree to be the best compromise between error minimization and polynomial stability.

However, the *polyfit* function provides feasible results but problems do arise. Figure 5.10 provides two examples of inadequate polynomial fitting.

The figures 5.10(a) and 5.10(b) show two different temperature profiles (using data from a real measurement) and their corresponding fitted polynomials. Both fits seem to be accurate but the problems become visible in the second derivatives in the figures 5.10(c) and 5.10(d). Those second derivatives are very different from what we would expect, compare figure 4.8(b). This is due to the least-squares minimization of the polynomial to the data: This fitting
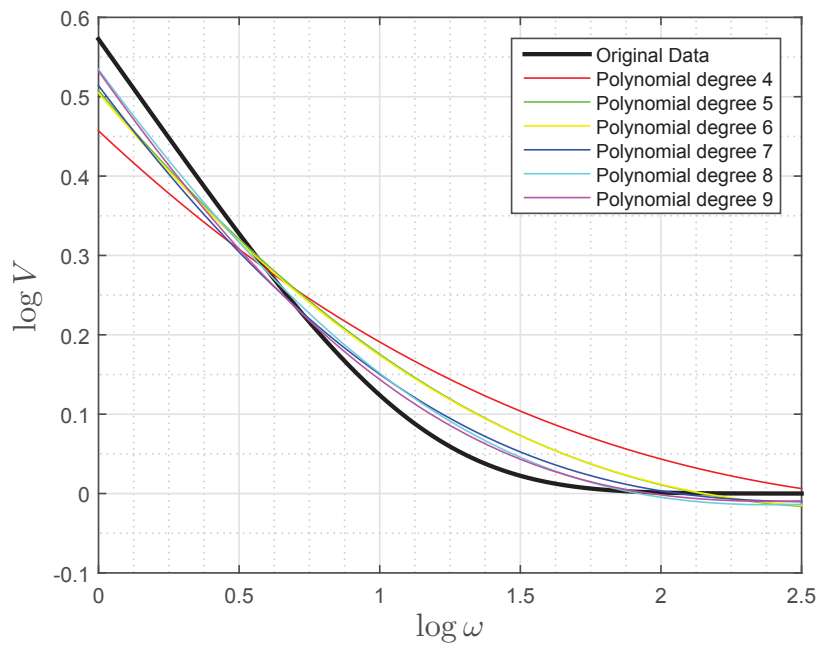
(a) Original temperature profile with fitted polynomials
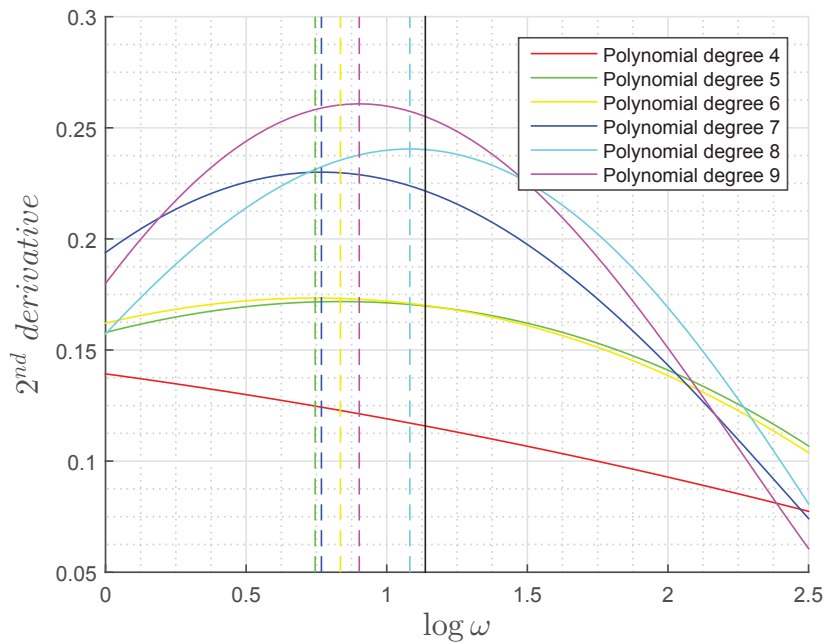
(b) 2nd derivative with fitted polynomials

Figure 5.9: Comparison of polynomials of different degree fitted to the temperature profile in reflection mode. In figure (b) the vertical solid black line marks the intersection of the two straight lines (t_w), the vertical dashed lines mark the maximum of the second derivative of each polynomial.
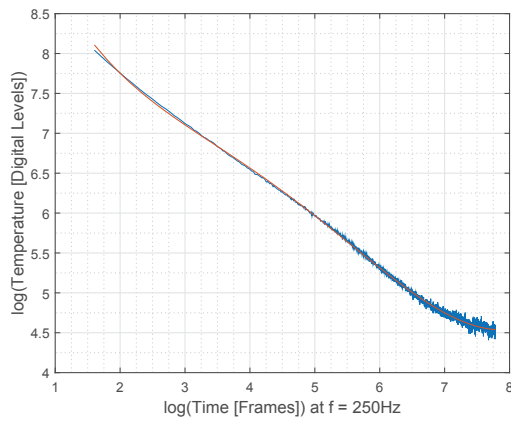
(a) Original data and fitted polynomial, example 1
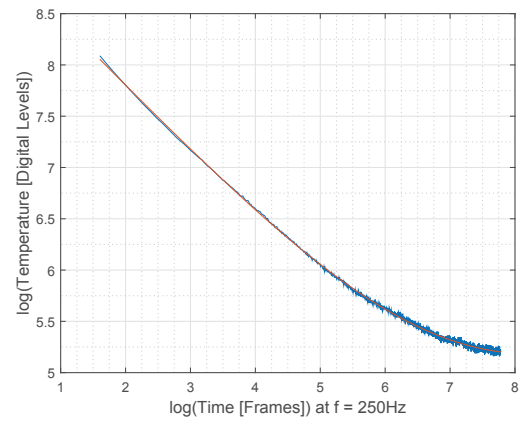
(b) Original data and fitted polynomial, example 2
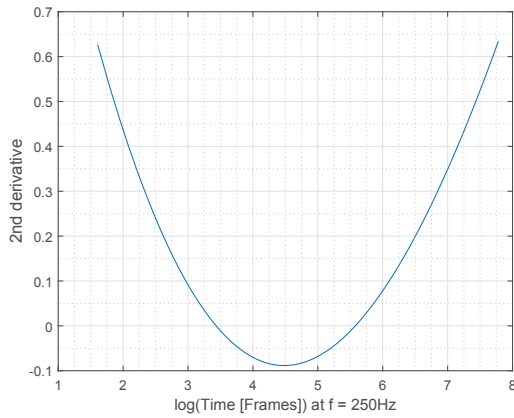
(c) Second derivative, example 1
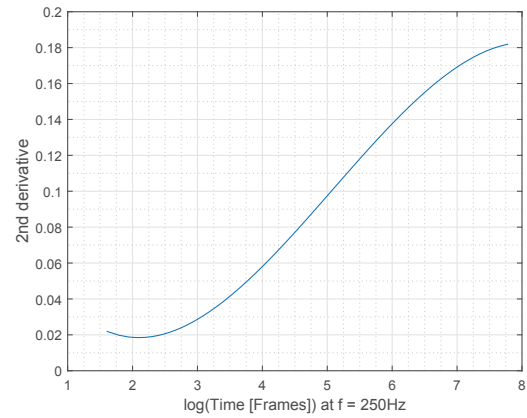
(d) Second derivative, example 2

Figure 5.10: Two examples of inadequate polynomial fitting with corresponding second derivatives

function does not consider any constraints in the derivatives of the polynomial. Therefore, the fitted polynomials can tend to high deflection at the beginning and end of the temperature profile due to the smaller number of support points. This problem is even more distinct at the start of the profile, since there are even less support points due to the logarithmic scaling.

Although the presented approach to fit polynomials to the measured data yields acceptable results, the mentioned problems lead to outlier and deviations in the consecutive evaluations. Thus, another approach to fit the polynomials was investigated and is presented in the following section.

5.3.4 Polynomial Fitting Using Discrete Orthogonal Polynomials

Since improvements in the polynomial fitting approach presented in the previous section are desirable, the following process attempts to fit polynomials including defined constraints to

the recorded data.

From the model presented in chapter 4 and especially in figure 4.8 we know that the first derivative at the start of the profile should be around -0.5 while at the end of the profile it should be zero. The second derivative should be zero at both, beginning and end.

To achieve such a fitting we use an approach and the corresponding tools developed by O'Leary and Harker and presented in [30]. Therefore, we generate a set of basis functions B. This set consists of n_{BF} polynomials of degree zero to $n_{BF} - 1$. We want to fit a polynomial of degree n_{poly} to the data and since we are not interested in basis functions of degree zero (which is just a constant) we need the numbers of basis functions to be

$$n_{BF} = n_{poly} + 1 \tag{5.3}$$

Furthermore, the linear combination of the polynomials of B can represent any value at every node in a given set of nodes. In our case, such a set of nodes is a vector with all time stamps of the frames within the recorded data in logarithmic scale (and therefore all values on the x-axis of a temperature profile), x_{Frames}. All polynomials within the set B are orthonormal and complete, which means that

$$B^T B = I \text{ (orthonormal) and} \tag{5.4a}$$

$$BB^T = I \text{ (complete)} \tag{5.4b}$$

and generated by the *dop* function of the *DOP-Toolbox*, which is based on the mentioned approach in [30].

We use the set of basis functions B to compute approximated values $\hat{y}$ as

$$\hat{y} = B\alpha \tag{5.5}$$

where α represents a vector with all coefficients of the polynomials. To receive a fit where $\hat{y}$ approximates the recorded data we compute:

$$\min_{\alpha} \|y - B\alpha\|_2^2 \tag{5.6a}$$

$$\text{given } C^T \hat{y} = C^T B\alpha = d \tag{5.6b}$$

where

$$y \ldots \text{temperature data}$$
$$B \ldots \text{set of basis functions}$$
$$\alpha \ldots \text{vector of coefficients}$$
$$C \ldots \text{set of constraints}$$
$$d \ldots \text{values of the constraints}$$

The set of constraints C is a column vector where every entry again is a row vector c. Each of those row vectors represents a constraint. To receive those constraint vectors c we generate a differentiating matrix D' using the *dopDiffLocal* function from the *DOP-Toolbox*. This differentiating matrix is a pseudo spectral approximation which computes the derivative of $\hat{y}$ as

$$\hat{y}' = D'\hat{y} \tag{5.7}$$

over a given support length $ls \in x_{Frames}$. It does this by fitting polynomials up to a degree of n_{Diff} to the nodes on ls using a least-square fit and returns the differentiated polynomials.

Analogously we can compute the second derivative of $\hat{y}$ as

$$\hat{y}'' = D'\hat{y}' = D'^2\hat{y} = D''\hat{y} \tag{5.8}$$

where

$$D'' = D'^2 \tag{5.9}$$

represents a pseudo spectral approximation of degree two.

Since the function points are unequally distributed due to the logarithmic scaling, it is difficult to find the best support length ls for the differentiating matrices. Therefore, D' and D'' are generated two times with different support length, which yields a total of four differentiating matrices. The parameters for this generation which were found to yield good results are summarized in table 5.1.

Parameter	Value	Description
ls_S	5	short support length
ls_L	91	long support length
n_{DiffS}	5	short support length polynomial degree
n_{DiffL}	5	long support length polynomial degree

Table 5.1: Values and descriptions of the parameters used for the generation of D' and D''

To define the constraint vectors c, we extract rows from the two differential matrices according to the desired constraint. In this context the rows of the differential matrices correspond to the location of the constraint. Thus, the first row represents the first point of the temperature profile (or a derivative), the last row of the matrix represent the last point of the profile (or a derivative).

The values of the constraints d are given as a column vector where every row (every entry in the vector) represents the value for the corresponding c vector in the constraint matrix C.

Since α is now the only unknown, we solve equation (5.6b) for α, which yields

$$\alpha = (C^T B)^+ d + \text{Null}(C^T B)\gamma, \tag{5.10}$$

where Null(A) is a vector basis for the null space of A, and substitute α in equation (5.6a) through this expression gained in equation (5.10), which yields

$$\min_{\gamma} \|y - B(C^T B)^+ d - B\text{Null}(C^T B)\gamma\|_2^2 \tag{5.11}$$

In this equation we substitute

$$H = B\text{Null}(C^T B)$$
$$Z = y - B(C^T B)^+ d$$

which yields

$$\min_{\gamma} \|Z - H\gamma\|_2^2 \tag{5.12}$$

Similar to the previous approach where we derived α we can solve this minimization for γ and receive

$$\gamma = H^+ Z + \text{Null}(H)\zeta \tag{5.13}$$

We act on the assumption that the basis functions in B will always fully span the space, thus Null(H) will always be of dimension zero. Therefore, we omit this second term in the equation.

Using the result from equation (5.13) in equation (5.10) we are able to compute α. Thus, we can calculate the y values of the fitted polynomial using

$$y = B\alpha \tag{5.14}$$

Instead of this possibility we transform those results into a geometrical polynomial using the Vandermonde matrix V. This matrix is the equivalent of B in case of geometrical polynomials in the context of

$$y = Vp \tag{5.15}$$

Compare therefore equation (5.14). The Vandermonde matrix is defined as

$$V = \begin{bmatrix} x_1^d & x_1^{d-1} & \cdots & x_1^1 & 1 \\ \vdots & \vdots & & \vdots & \vdots \\ x_n^d & x_n^{d-1} & \cdots & x_n^1 & 1 \end{bmatrix} \tag{5.16}$$

where x represents a vector of n values and d equals the degree of the corresponding geometrical polynomial p. We compute p as

$$p = V \backslash B\alpha \tag{5.17}$$

where the operator "\" represents a MATLAB internal function which inverts a matrix with the minimum number of coefficients. In the case of a full ranked set of basis functions B, this operator equals the generation of a pseudo inverse matrix.

The quality of the polynomial fit highly depends on the chosen parameter. Those are for example the support length and the degree for generating the differentiating matrices.

Furthermore, the constraints influence the result of the fitting in terms of number of constraints and their values. Evaluations with three and four constraints have been carried out. Those constraints were

$$y'(n_{Frames}) = 0 \qquad\qquad y'(1) = -0.5$$
$$y''(1) = 0 \qquad\qquad y'(n_{Frames}) = 0$$
$$y''(n_{Frames}) = 0 \qquad\qquad y''(1) = 0$$
$$y''(n_{Frames}) = 0$$

where n_{Frames} represents the number of frames in the record (and therefore the last points on the x-axis).

Since the constraints restrict the degree of freedom, attention must be paid to the chosen polynomial degree. For every constraint added to the fitting we have to increase the degree of the polynomial by one ([31]). If we consider figure 4.9 the minimum degree of the polynomials is $n_{min,FL} = 2$ for temperature profiles over flawless material and $n_{min,DF} = 4$ for profiles over defects. Thus, we end up with $n_{min,FL} = 5$ and $n_{min,DF} = 7$ when we use three constraints

and $n_{min,FL} = 6$ and $n_{min,DF} = 8$ when we use four constraints.

When we fit a polynomial to the temperature profile of a pixel, we have no a priori knowledge if there is a defect beneath this point on the surface. Thus, we have to use a polynomial of higher degree (which is $n_{poly} = 7$ or $n_{poly} = 8$) to be certainly able to represent the temperature profile of a defect. A problem when using polynomials of high degree for temperature profiles over flawless material (very straight-lined) is that those polynomials tend to deflect. Figure 5.11 shows two examples of this problem.
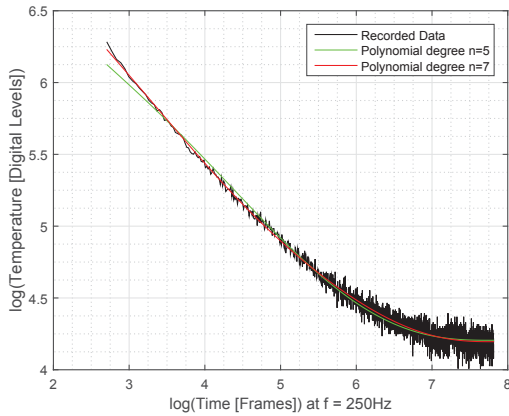
(a) Recorded data and fitted polynomials, example 1
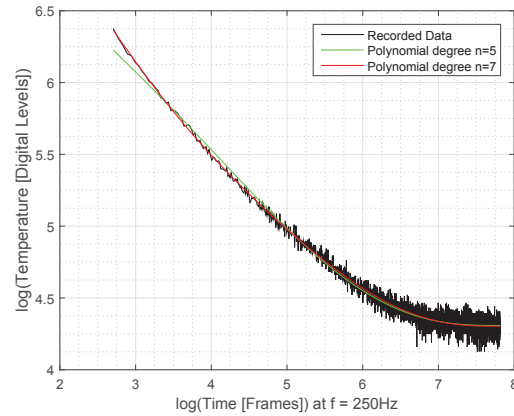
(b) Recorded data and fitted polynomials, example 2
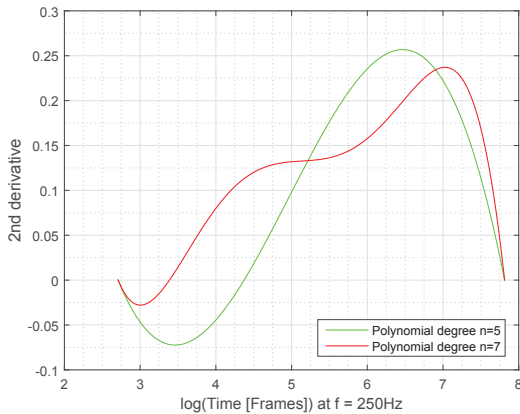
(c) Second derivatives of fitted polynomials, example 1
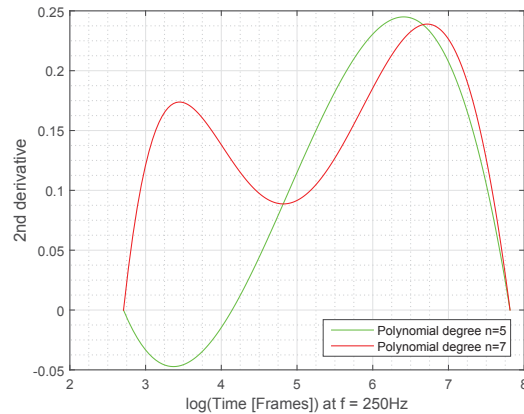
(d) Second derivatives of fitted polynomials, example 2

Figure 5.11: Problem with deflection of polynomials of higher degree

The fitted polynomials in figure 5.11(a) and 5.11(b) look rather promising. The polynomial of higher degree seems to approximate the recorded data even better than the polynomial of lower degree. But if we consider the figures 5.11(c) and 5.11(d) we can see that the fluctuating behaviour within the data in case of the polynomial of higher degree yields higher fluctuations in the second derivative. In both cases, the second derivative of the polynomial of lower degree looks much more like we would expect from figure 4.8(b) compared to the one of

higher degree. In the first example, the maximum in the second derivative of the polynomial of higher degree is shifted backwards while a high curvature in the second example yields to another maximum which would be mistaken by the algorithm as defect.

This leads to the problem that a polynomial of lower degree is hardly able to approximate a temperature profile of a defect, while a polynomial of higher degree tends to instability for temperature profiles of flawless material. Thus, a new approach to solve this problem was developed: The difference in the y values between both polynomials is computed as r^2, which is the sum of the squared differences. If the considered temperature profile is of flawless material, r^2 can be expected to be relatively small (since the polynomials themselves are very close to each other, only the second derivatives vary widely, compare figure 5.11). In case of a defect, r^2 can be expected to be much larger because the polynomial of lower degree will hardly be able to approximate the data, while the polynomial of higher degree will yield a good fit. Thus, r^2 is used as an indicator to distinguish between flawless and defect material. Polynomials of both low and high degree are fitted to the data of every single pixel and r^2 values can be illustrated as picture of the corresponding specimen ("difference picture"). This picture can be used as a qualitative result of the defect detection.

Furthermore, a difference limit e_{Limit} is introduced which is supposed to enable the automatic distinction between defect pixels and flawless pixels. If r^2 is below this limit, the material of the pixel is considered flawless and further evaluated using the polynomial of lower degree. Otherwise the polynomial of higher degree is used for further processing. The evaluation process after this distinction is the same as for the polynomials gained from MATLAB's *polyfit* function (compare section 5.3.3) and further described in the next section.

Note that the success of this approach highly depends on the chosen difference limit e_{Limit}. The procedure to define such a limit is to display the difference picture to the user, who is asked to define a rectangle on this picture, which he believes to be flawless material. All r^2 values of the difference picture within this rectangle are then further processed. The mean value of those pixels and the standard deviation is computed. The difference limit is then defined as

$$e_{Limit} = \mu_{r^2} + n_{std} \cdot \sigma_{r^2} \qquad (5.18)$$

where

e_{Limit} ... difference limit

μ_{r^2} ... mean value of r^2 values within the selected region

n_{std} ... multiplier of standard deviation

σ_{r^2} ... standard deviation of r^2 values within the selected region

A reasonable value for n_{std} was found to be around two.

Note that this evaluation method is not callable from the GUI in the measurement software presented in chapter 3.6. This is due to the high dependency of this evaluation on the used parameters. It has to be assumed that only experienced users will be able to use this method in the appropriate way and receive feasible results. Thus, as long as the presented software is not adapted and optimized to specific applications, the DOP evaluation remains experimental.

5.3.5 Maximum Determination in the Second Derivative

For further evaluation, the (geometrical) polynomials need to be differentiated twice and the correct maximum in the second derivative needs to be determined (compare chapter 4.3). To do this, MATLAB's function *polyder* ([39]), which derives a given polynomial, is used four times to receive the polynomial of the second, third and fourth derivative. To find the maximum of the second derivative, we need to find the roots of the third derivative with MATLAB's *roots* function. Subsequently, we distinguish (desired) positive from negative extreme points by evaluating the polynomial of the fourth derivative at the determined roots.

Since the presented methods and approaches to fit a polynomial to the recorded data are not free from errors, we can not be sure that the profiles will always look as we expect. Experiments showed that through bad polynomial fitting in special cases maximum points can arise which are complex or lie outside the record time. To deal with such special cases the determined extrema are checked with particular condition. Such conditions are e.g. that only real (no imaginary) extrema are considered or that the extremum needs to be located within the record time. If more than one extremum which satisfies all those conditions remains, the first one is used as result (t_w), since it is supposed to represent a defect. If there is no extremum left after the particular condition check, the result is set to zero.

Such adjustments (adding particular conditions to the evaluations to change the result of t_w) can be very helpful, since there will always be borderline cases where the evaluation fails to determine the correct value, although a human investigator would have been able to do so. Those issues can be largely dealt with by adding such particular conditions to the

evaluation which solve the specific problem but have no influence on the evaluation in general (so that those interventions do not interfere with already correct evaluations). Note that if the presented processes are used in a concrete application and can therefore be optimized for a set of test cases, more particular conditions could be added to improve the results. In the course of this work, more general conditions (which do not improve the result of one specimen at the expanse of another one) could not be found.

5.3.6 Qualitative and Quantitative Investigations

As described in the previous sections, determined t_w values can be associated with thermal diffusivity or thickness/depth values. However, experiments show that the determined t_w values often yield results (thickness/thermal diffusivity) which deviate from the actual properties of a specimen. This problem will be discussed in detail in chapter 7. Nevertheless, the derived values often give a good qualitative statement about defects in a specimen, even if their actual (quantitative) properties can not be reproduced properly. Thus, the TSR investigations are split into two parts:

- **Qualitative Investigations:** The results of the evaluations are used to determine defects in qualitative manner. This includes all result pictures, wich are t_w, thermal diffusivity, thickness/depth pictures. Furthermore, the value of the second derivative of the fitted polynomials (of both, the *polyfit* and the DOP approach) at certain points in time can be illustrated as image. Since the second derivative of a polynomial is very sensitive to the progress of the profile, those images often provide a very good estimation about existing defects within a specimen.

- **Quantitative Investigations:** If defects are detected within a specimen, their properties can be determined in quantitative manner, using thickness/depth and thermal diffusivity pictures in particular.

Note: Since the result pictures (t_w, thermal diffusivity and thickness/depth) give qualitative as well as quantitative information, they are used for both investigation steps at once for the examples which will be presented in chapter 7.

5.4 Measurement in Reflection Mode - PPT

To perform a PPT evaluation as described in section 4.4, MATLAB's *fft* function [39] is used. This function is applied to every temperature profile of every single pixel in the record and returns all frequencies consisting of a real and imaginary part in the form of (compare [38]):

$$F_n = \sum_{k=0}^{N-1} T(k)e^{2\pi ikn/N} = Re_n + i \cdot Im_n \tag{5.19}$$

This yields the frequency spectrum, separated in n discrete frequency increments. Those frequency increments are stored in a three-dimensional matrix, where the first two dimensions relate to the x- and y-axis of the recording window and the third dimension holds the result of the transform. Note: The Fourier transformation is applied to the whole temperature profile (no flash elimination).

According to [38] the amplitude and phase shift (compare chapter 2.5.2) for every frequency increment (compare section 4.4) can be calculated as

$$A_n = \sqrt{Re_n^2 + Im_n^2} \tag{5.20a}$$

$$\phi_n = \arctan\frac{Im_n}{Re_n} \tag{5.20b}$$

Those results are again stored in a three-dimensional matrix (amplitude and phase shift in separate matrices), where the first two dimensions relate to the x- and y-axis of the recording window and the third dimension holds the desired value (amplitude or phase shift) for a specific frequency increment.

Since phase shift images are less sensitive to non-uniform heating than amplitude images (according to [38]), the phase shift image is used for further defect detection. Furthermore, because of the similarities of PPT to Lock-in thermography (compare chapter 2.5.3), [14] states that the phase image could be used for quantitative defect depth determination. Figure 5.12 illustrates the first four phase images (starting at the lowest frequency) at the given frequencies for the sample described in chapter 7.3. Note that the first phase image is actually the image at $f = 0Hz$, but since this represents a constant excitation there is no phase shift at this frequency and this image is therefore not considered. Note also that the irregularity in the upper right corner of the images represent the support (holder) of the specimen.

Those phase images reveal a specific property of the PPT: The phase of the Fourier transform acts as a band pass filter [38]. This means that different frequencies will yield a phase shift only for specific depths or for a range of depth, respectively. This can be observed in those four phase images. In figure 5.12(a) (lowest frequency) even the deepest (upper right) defect is very well visible, while the shallowest (lower left) defect is much less distinct compared to the other phase images. With increasing frequency the deepest defect disappears from the phase image while the shallowest becomes better and better visible. Figure 5.12(d) shows that the deepest defect is not visible any more and the middle deep

(a) f = 0.0042Hz

(b) f = 0.0083Hz

(c) f = 0.0125Hz

(d) f = 0.0167Hz
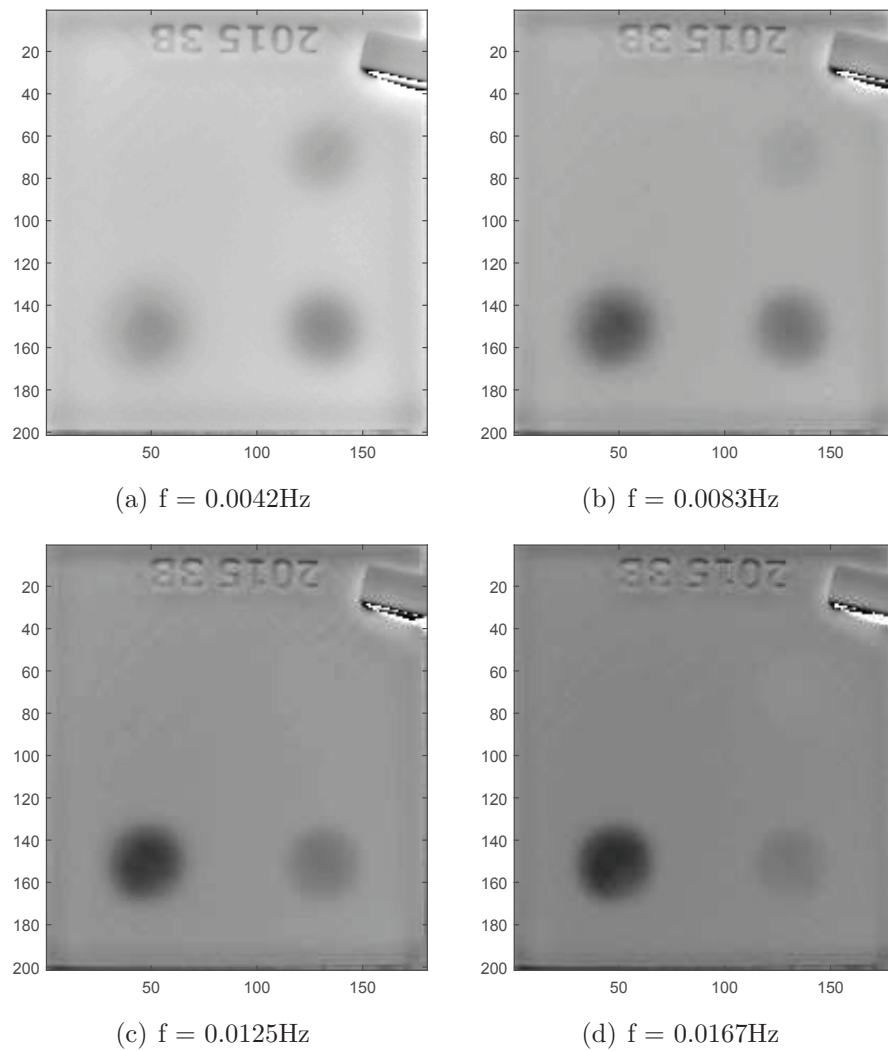
Figure 5.12: Phase images for corresponding frequencies

defect (lower right) tends to disappear from the phase image. This is due to the decreasing amplitude of the inserted energy and therefore the decreasing signal-to-noise ratio (compare figure 4.11(b)).

This means that important information is spread on different phase images. Thus, two features have been developed to assist the user at the defect detection.

- **Value Accumulation:** This function uses a number of phase images (starting from the lowest frequency to the number specified by the user) from the result of the computation and computes the sum of phase shift values for every pixel over the specified number of frequency increments. This is to accumulate the phase and therefore the phase of possible defects over a variety of frequencies. Experiments showed that this number should be kept at small levels (4-5) since the noise increases tremendously when using phase shift images of higher frequencies.

- **Difference Accumulation:** This function uses an approach similar to the base material extraction in image processing (chapter 6.2). However, the procedure used here is much simpler and therefore only the fundamentals will be described here. The complete process is presented in detail in chapter 6.2. For this evaluation method all pixel values (phase values) are stored in a histogram. If the specimen takes the major part of the image, the flawless material will yield a high peak in terms of pixel values in this histogram (compare figure 6.2). The process further extracts this maximum peak in the histogram. This peak is supposed to describe the phase value of the surfaces above flawless material. Note that for the success of this approach, the same requirements as for the base material extraction (chapter 6.2) must be met. This obtained value is then subtracted from a number of phase images. This number is again specified by the user and the image selection starts at the lowest frequency and ends at the specified number. Thus, the resulting images will contain values around zero on surfaces of flawless material, while the defects will yield a different value. This increases the ratio of values for defects and values for flawless material. Following the difference images of the selected phase images are summed up. Additionally, this feature provides the possibility to select a rectangle in the recording window and only use pixels of this selected excerpt for the difference accumulation. This is necessary in case the specimen does not cover a major part of the recording window.

Figure 5.13 illustrates the results of those features applied on the previously used sample.

(a) Value Accumulation   (b) Difference Accumulation
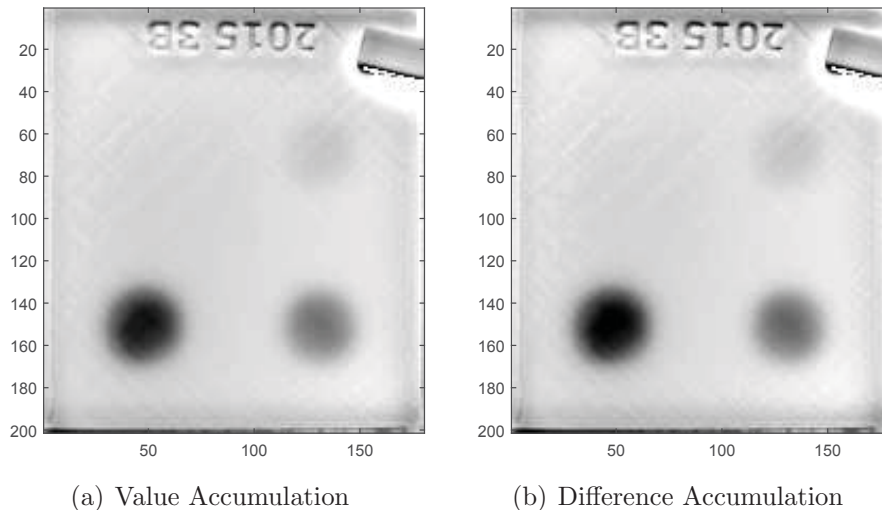
Figure 5.13: Results of the assistant features "Value Accumulation" and "Difference Accumulation"

Both features face some problems:

- The phase shift depends not only on the defect depth but also on the frequency for

which it is computed. Thus, if the phase shifts (or the differences of the phase shift of defects compared to the flawless material) are summed up or averaged, the resulting value can not be considered as representative for a specific depth. Those two methods only suit a qualitative defect detection.

- If a number of images is computed and a defect is well visible only on a small number of those images (as it is the case in the example in figure 5.12) the representation of this defect in the resulting figures will be smaller than in the original images because of the summing and averaging. This problem also argues for a small number of images to choose for the processing.

Through those problems the user is urged to not only use the assistant features, but also investigate some of the phase shift images (probably some of the lowest frequencies) specifically. The success of those features also highly depends on the measurement parameters, such as recording time and recording frequency (which again depend on the material of the specimen, ...). For CFRP and plastic specimens, this thesis recommends to compute the value accumulation and the difference accumulation of the first four phase shift images (four lowest frequencies) as well as to display those four images for qualitative defect detection. The usefulness of the presented features is investigated in detail in the specific examples in chapter 7. Note that since the phase shift does not only depend on the defect depth but also on the evaluated frequency (and therefore on the record length and recording frequency) the depth determination using the phase shift (as described by [14]) would go beyond the scope of this work and is therefore not further examined.

5.5 Manual Evaluations

To give the user the possibility to directly and easily evaluate measurements and illustrate the results in charts and pictures, some tools have been developed and implemented into the software. Those tools are presented and demonstrated on the 3D printed part described in chapter 7.3, measured and evaluated in reflection mode. Note: Those evaluation tools are implemented for measurements in transmission as well as in reflection mode, using the *polyfit* approach (5.3.3) of the TSR technique. However, only the profile plotting for particular pixels described in section 5.5.1 is executable for measurements in transmission mode. Further tools are only available for measurements in reflection mode.

5.5.1 Plotting Profiles of Particular Pixels

To detect and investigate defects manually and quickly, the software enables the user to interactively choose (an arbitrary number of) points on the resulting t_w picture (or the first

frame of the record in transmission mode). An example is illustrated in figure 5.14.
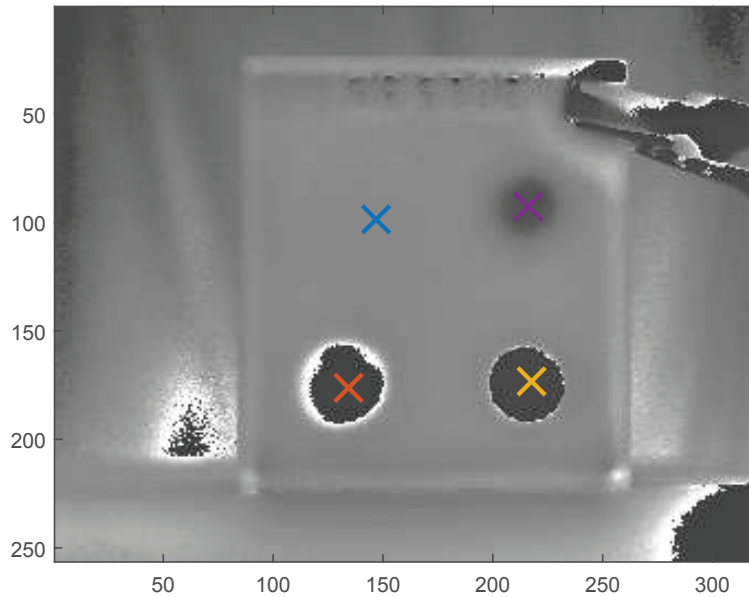
Figure 5.14: Selected pixels by user on the t_w picture

To receive the desired profiles, not only the temperature profiles of the particular pixels are used for computation. The desired pixel is averaged together with the eight surrounding pixels (which results in an 3×3 - matrix). This average computation is to reduce noise of this particular pixel. Consecutively T_0 of the specific profile is subtracted from this profile.

Next, the t_{EoF} determination is executed as presented in the corresponding previous sections. The temperature profiles are plotted from t_{EoF} to the end of the record.

For better comparability, the (unfiltered) image (figure 5.14) is returned by the software together with the selected pixels in the color according to the temperature profile in figure 5.15.

Note that in case of an evaluation in transmission mode the result is not illustrated in double logarithmic space but in linear space.

5.5.2 Plotting Polynomials of Particular Pixels

To investigate the quality of the polynomial fitting and to inspect the second derivatives of the temperature profile in case of a measurement in reflection mode and a TSR evaluation, the user has the possibility to plot the information from selected pixels (in this example from the selected pixels in figure 5.14). The pixels are selected and the temperature profiles are extracted from the record in the same way as described in section 5.5.1. Furthermore, polynomials are fitted to those profiles, differentiated and evaluated as presented in section
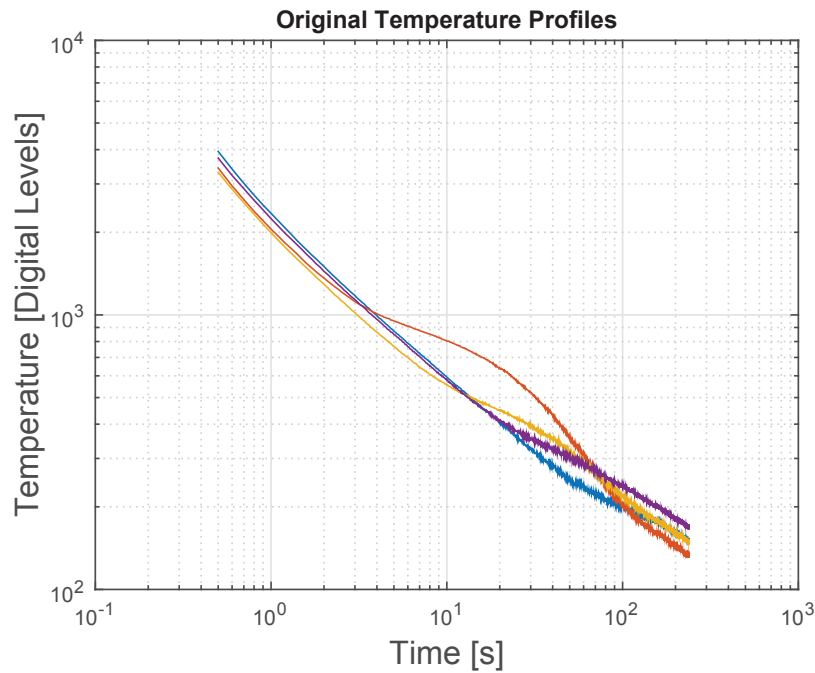
Figure 5.15: Temperature profile of the selected pixel in figure 5.14

5.3.3 to receive the fitted polynomials and the corresponding second derivatives. The results of this example are presented in figure 5.16.

(a) Temperature profiles

(b) Second derivatives
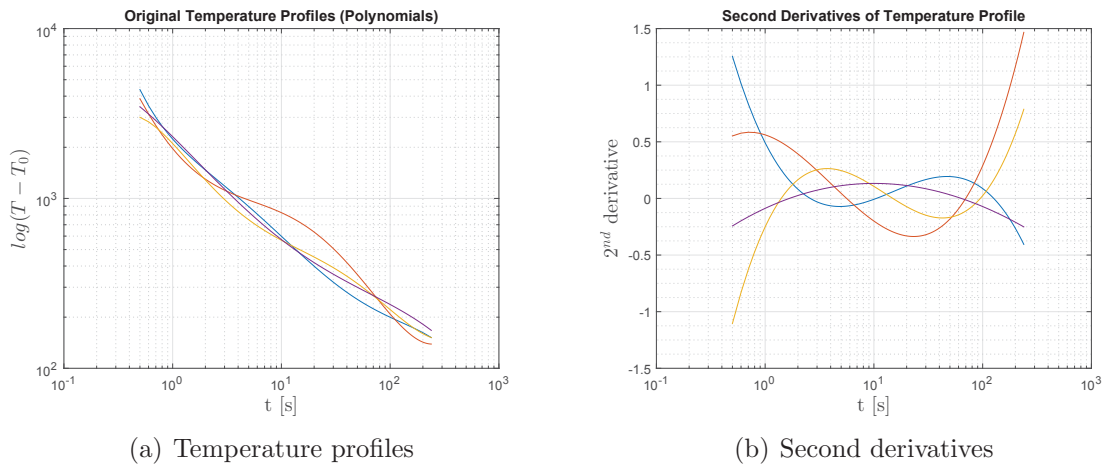
Figure 5.16: Temperature profile and second derivatives of the selected pixels

5.5.3 Imaging Second Derivatives at Certain Times

A very useful visualization of the temperature response of a specimen is the second derivative of the time profile, since the maximum of this derivative marks t_w (compare chapter 5.3). It is desirable to see the value of the second derivative for every pixel of the entire recording

window (illustrated as picture) at t_w of a particular pixel. This helps the user to investigate the behaviour of the rest of the specimen at t_w of a selected pixel (for example a defect).

Therefore, the user is asked to select (an arbitrary number of) points on the resulting t_w picture. Afterwards, a polynomial fitting and its second derivative is applied to the time domain of every single pixel of the record. In contrast to the previously described methods, the polynomials are not directly evaluated (for example to find a maximum) but the polynomials of the second derivatives are stored in a matrix. This yields one polynomial for every single pixel of the record.

Subsequently, those (second derivative) polynomials are evaluated at the t_w values corresponding to every selected pixel in the t_w picture. Figure 5.17 illustrates such an evaluation of the same four pixels selected in figure 5.14.

(a) Second derivative after 1.8s

(b) Second derivative after 4.8s

(c) Second derivative after 10.9s

(d) Second derivative after 47s
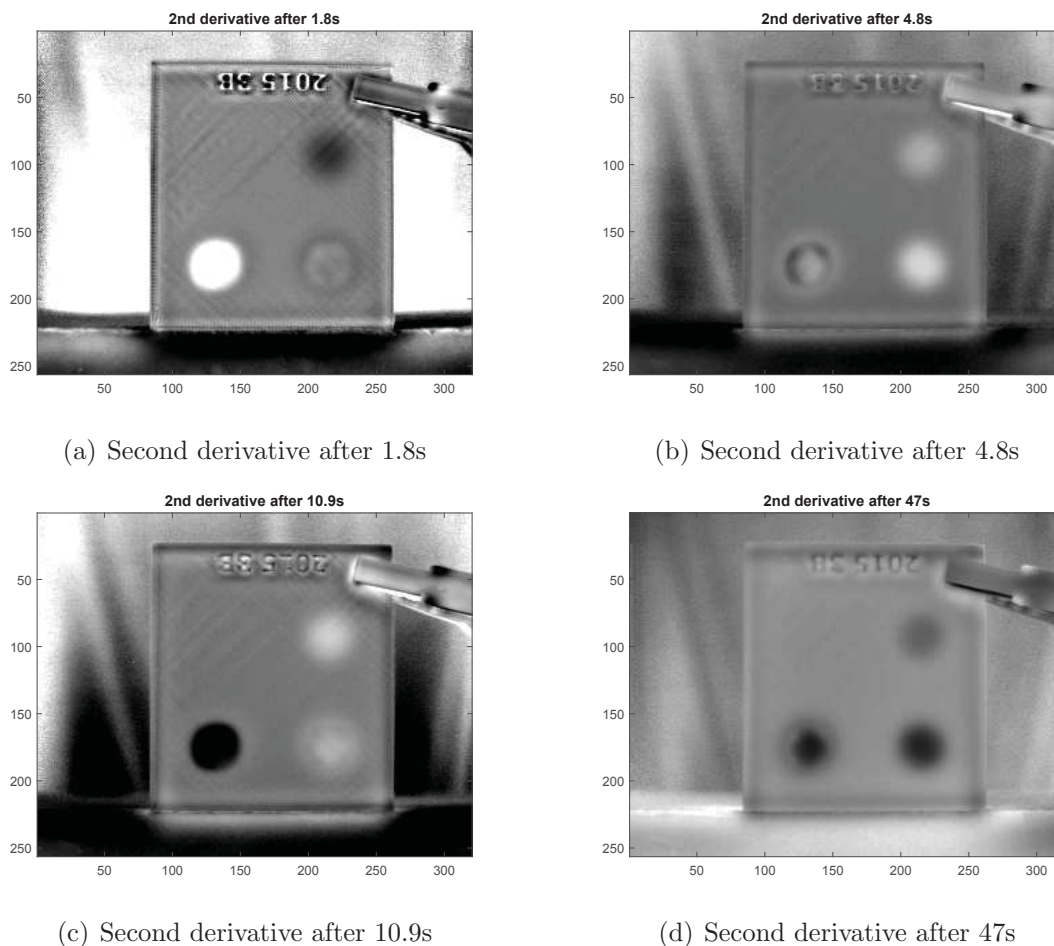
Figure 5.17: Evaluations of second derivatives at t_w of selected pixels

5.5.4 Imaging Second Derivatives at Maximum Difference

As figure 5.17 illustrates, the values of t_w are not equal to the time of maximum contrast. Therefore, a method was developed to evaluate second derivatives at times of better contrast.

This method asks the user to interactively select two pixels on the t_w picture between which the contrast is to be maximized. It then extracts the temperature profiles of those two points and fits polynomials to them. Afterwards the temperature differences for every point in time of the evaluated polynomials is computed. Finally, the second derivative picture is evaluated at the point in time of maximum temperature difference.

If we want to receive a second derivative picture of maximum contrast between two points, we would naturally search for the point in time of maximum difference in this second derivative instead of the temperature profiles. But the second derivatives of the fitted polynomials tend to highly deflect at the boundaries of the range (compare for example figure 5.16(b)). Searching for a difference maximum in this data would yield unwanted results (resulting evaluation times at the boundaries instead of a time within the period of heat flow). It is also quite difficult to determine limits in which between the desired time has to be searched for. On the other hand, the polynomials of the temperature profiles represent the original data very well, even at the boundaries (compare figure 5.16(a)). Additionally, as figure 5.16(a) implies, we can suppose that a point in time of high temperature difference is a point in time of high differences in the curvature of the profile as well. Those assumptions enable us to create a quite simple way to quickly search for high differences in the second derivatives of the profiles.

Figure 5.18 illustrates the result of the procedure described above.
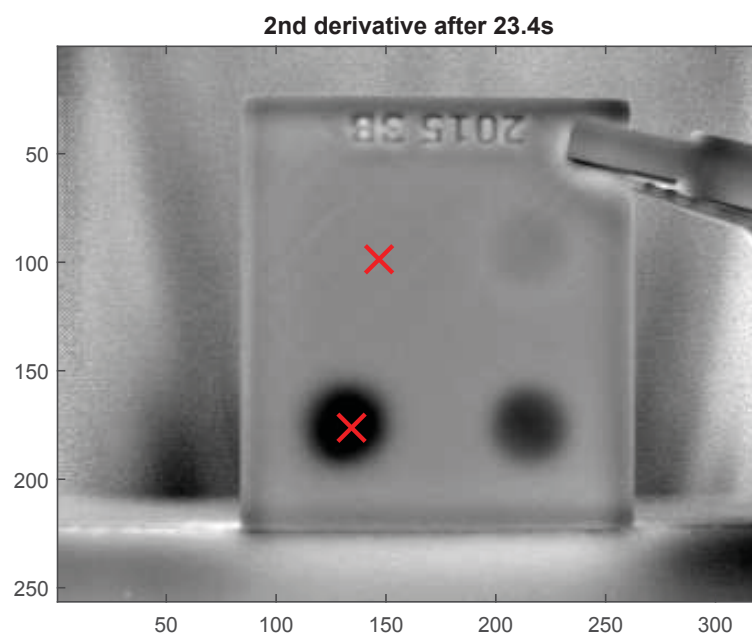
Figure 5.18: Second derivative at maximum difference in temperature (23.4s), selected pixels marked on the picture.

6 Image Processing

The goal of the image processing is to derive qualitative conclusions from the quantitative results of the data processing (chapter 5). Algorithms have been developed which identify values of the results as defects or non-defects. The methods have to be able to separate such defects from the base material and return information about every single defect.

The results obtained after data processing are images of the specimen where every pixel does not represent the intensity level of a certain point in time, but a certain value (time, α, L, D, ...). This value describes the heat flow through or specific material properties of the sample on this exact location (compare chapter 5). Most of the time, the image processing uses differences in the values between the pixels and therefore the presented methods suite for transmission as well as for reflection measurements. The progress is illustrated largely on the basis of a precursor of a real specimen in reflection mode (where a t_w picture was used, see figure 6.1) which is further described in chapter 7.3. This precursor consists of a different material than the example used in 7.3, thus the t_w values are different from the following evaluations. However, the t_w picture of this sample shows errors and problems which are greatly suited to demonstrate the image processing approaches. Note: The used data processing method is polynomial fitting using MATLAB's *polyfit* function (compare section 5.3.3).

6.1 Elimination of Outliers

The evaluation algorithms presented in chapter 5 turned out to be very reliable, however, outliers still appear in the results. Since those outliers would affect further calculation, for example the thickness calculation using the average of a wide area of values in the resulting pictures, those outliers have to be eliminated as entirely as possible.

There are a number of algorithms for 2D filtering. An example is to calculate the average of a matrix of pixels around a certain pixel and replace the actual value of this certain pixel by the computed average of the matrix [7]. This approach would spread incorrect influence of the extreme values on bigger parts of the image. Therefore, another type of non-linear filter was chosen. This filter calculates the median of a $m \times n$ matrix around a certain pixel. The value of this pixel is then replaced by the computed median [7]. This process is performed for
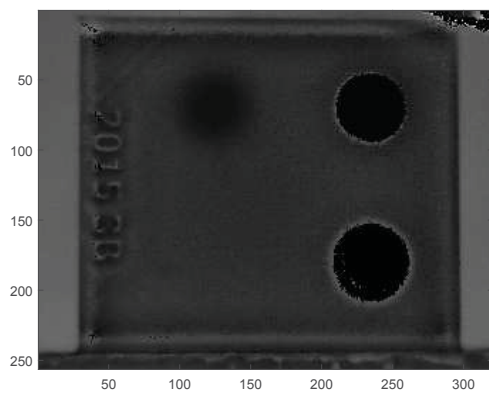
(a) Original t_w picture
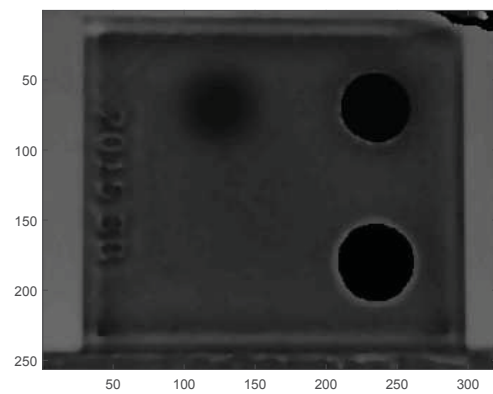
(b) Filtered t_w picture
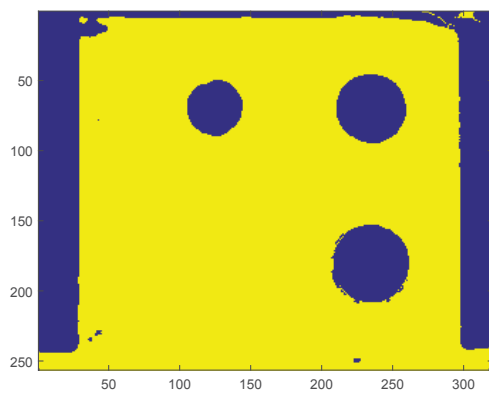
(c) Original mask
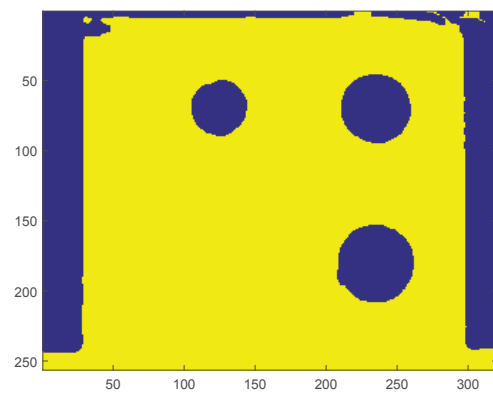
(d) Closed mask
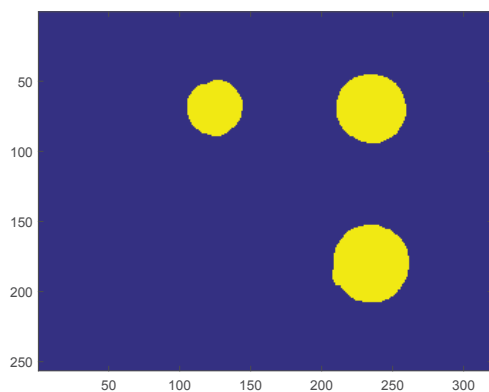
(e) Defects
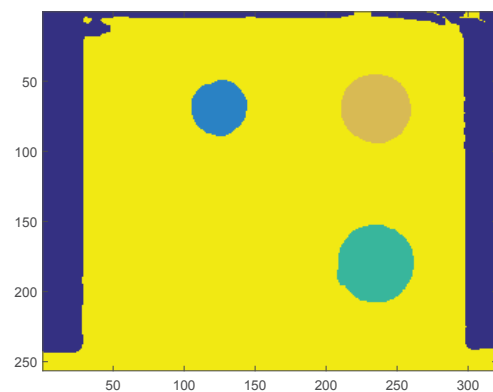
(f) Labeled defects

Figure 6.1: Illustration of the progress of image processing on the basis of a real sample in reflection mode.

all pixels of the result picture. Such a filter is available in MATLAB and called *medfilt2* [39]. The *medfilt2* filter is especially suitable for the "salt & pepper" problem, where a picture is loaded with noise which results in sparsely spread bright and dark pixels. This problem describes the outliers in the results of the presented evaluation methods very well. Since this filter replaces the pixel by the median instead of the average, edges are preserved well [39]. Those characteristics make this filter very suitable for the described problem.

Tests showed, that a 5×5 filter matrix yields very good results at full resolution (320×256).

As an illustration of this filter method see figure 6.1(a) and figure 6.1(b) respectively. One can observe the elimination of wrong pixel values in the defect in the lower right area (bright pixels), as well as in the base material within the characters on the left side and the upper left corner of the specimen (dark pixels).

6.2 Extraction of the Base Material

To find the specimen or the pixels which represent the flawless material of the sample, an algorithm was developed which requires the following preconditions (which also apply to the difference accumulation in section 5.4):

- The dimensions of the sample take a better part of the recording window. This can be ensured by varying the distance between camera and sample as long as the specimen is of rectangular shape with a width-to-height ratio of not much more than one.

- The flawless surface emits radiation homogeneously. This means the specimens should not exhibit scratches, edges, reflections etc. on its surface. This condition can be highly satisfied by simply painting the surface with a dull, black paint (homogeneous emissivity across the whole surface close to one).

- The pixels representing flawless surface are a multiple of pixels representing surface above defects.

Since the following procedures use statistical methods to identify defects in the specimen, the function of the first condition is to ensure that the results are not distorted by pixels which belong to the surrounding area or the background behind the specimen. To keep such pixels out of further computations, an additional feature was added to the software. If the specimen does not take a better part of the recording window, the user has the possibility to choose a rectangular window on the resulting picture which covers the specimen. For the following computations only the pixels of this window will be chosen. Thus, pixels around the actual specimen do not influence the statistical evaluations.

To find the flawless surface, all pixels are stored in a histogram. Therefore, MATLAB's *hist* function [39] is used to perform this task. The number of bins is set to [32]

$$n_{bins} = \sqrt{n_{pixels}} \tag{6.1}$$

where n_{pixels} is the total number of pixels in the picture, which is usually the maximum resolution of the camera of $n_{\text{pixels}} = 320 \times 256$.

Since we presume that the number of pixels of flawless surface count for the better part of the total number of pixels, we assume that the histogram will have a high amplitude at the value which represents the flawless surface. Since there is impurity in the specimen and noise in the radiation, we suppose a Gaussian distribution of the values around this peak.

In fact, tests prove those assumptions as appropriate. Figure 6.2 show such a histogram of a real specimen as an example.
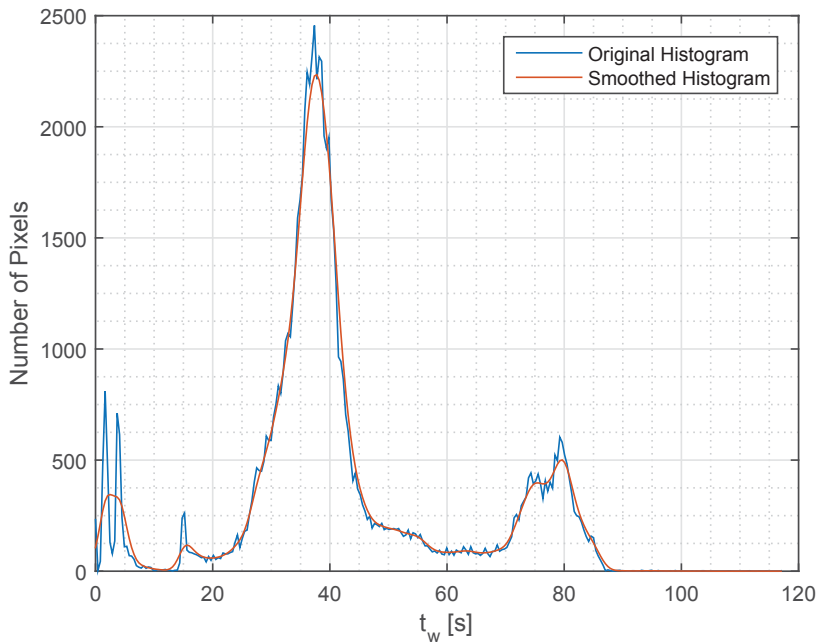
Figure 6.2: Histogram of pixel values (t_w values) of a resulting picture. The two trends show the histogram before and after convolution.

To smooth this histogram we use the principle of convolution [21]. MATLAB provides such a function named *conv* [39]. To perform such a convolution, we generate a 1-D Gaussian kernel in the length of five percent of the number of bins and norm this kernel. Note that the usage of the mentioned five percent is not a mathematical rule but a value which had been found convenient in experiments executed in the course of this thesis. The result of such a convolution compared to the original histogram is illustrated in figure 6.2.

The histogram in this figure represents the flawless surface pixels as big peak with Gaussian

noise (as we expected). Furthermore, one can observe that possible defects deposit as such peaks as well, but with much smaller magnitude, because of the much smaller number of pixels which represent such a defect. To separate the flawless surface from the defects, we mark all pixels which are located within the Gaussian curve which represents this surface. To find the correct curve (since every defect yields an independent Gaussian curve as well) we search for the maximum value within the histogram. Because of the chosen preconditions, we can always expect this maximum value to be the mean value of the flawless surface and therefore the peak of the according Gaussian curve in the histogram.

In an ideal case the histogram shows a big Gaussian curve which represents the base material and some smaller Gaussian curves which correlate with the defects (depending on the number and size of the defects). A way to separate those curves from each other and consequently the defects from the base material is to find the intersections of those curves which represent the minimum probability of the adjacent distributions [27]. But because of the noise it is very difficult to determine such an exact intersection between the curves, compare figure 6.2 from $t_w = 50s$ to $t_w = 70s$. To consider this noise we determine an upper and a lower limit of values around the identified maximum to define a range within this Gaussian curve which will be considered as values of the desired surface (the base material).

To do so we compute the gradient of the histogram. An example of such a gradient is illustrated in figure 6.3(a).

(a) Gradient of the Histogram   (b) Smoothed Histogram
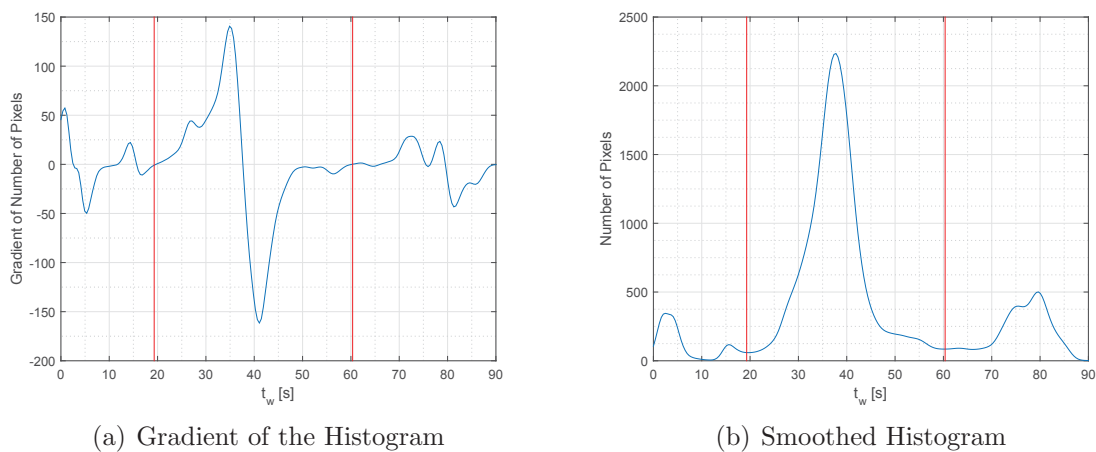
Figure 6.3: Determined limits for base material pixel selection.

To determine the limits, the roots of this gradient are evaluated and the two values closest to the computed maximum of the histogram are chosen as upper limit (closest root above the maximum) and lower limit (closest root below the maximum).

Figure 6.3 illustrates those limits in gradient and histogram chart according to the example.

Every pixel of the picture can now be classified as base material (flawless surface) and non-base material (surrounding outside of the specimen and defects) according to the determined

limits. Through this it is possible to generate a mask which represents the flawless material. Figure 6.1(c) illustrates such a mask. One can also compare this mask to the original image in figure 6.1(a) from which the mask was derived.

This mask still contains pixels which are assigned incorrectly. This problem can be seen in figure 6.1(c) in the lower left corner of the sample and below the lower right defect (although those pixels do neither belong to the material nor are they defects - they represent the holder for the specimen during the measurement), as well as in the border area of the lower right defect. Therefore, binary morphology operators are used to eliminate those errors [21].

The chosen procedure is to use MATLAB's *imdilate* and *imerode* functions ([39]), which perform a dilation and erosion on the image (the mask) using a predefined kernel size. The combination of those two operators in this exact order eliminates single pixels and small pixel accumulations which are assigned to the wrong category [3]. This whole process is called "closing" [21]. Tests showed that a kernel of size 5×5 at full resolution (320×256) yields good results. Figure 6.1(d) illustrates the processed mask. The incorrectly assigned pixels described above can be eliminated, the border area of the defect is smoothed. Unfortunately this process is not able to close the opened area in the upper left corner of the sample.

Although this approach yields good results for wrong pixels within the specimen, it is not able to reduce such pixels in the surrounding of the sample. Figure 6.4 illustrates this problem and the suggested solution.

Figure 6.4(a) shows the α picture of the described 3D printed part in transmission mode. Figure 6.4(b) illustrates the extracted base material using the procedure described above. This mask includes pixels which obviously do not belong to the specimen. This is because those pixels of the surrounding area of the sample have an α value which (coincidentally) fits into the computed boundaries. The presented approach of a combination of dilation and erosion operations does not eliminate those wrong pixels. Quite the contrary, the dilation yields the scattered pixels in the lower zone of the picture to connect to a single larger area. The following erosion operator is not able to undo this problem, see figure 6.4(c). Therefore, this procedure is repeated, but in opposite sequence, which is called "opening" [21]. This means, after the dilation and erosion, the resulting mask is again edited with an erosion and afterwards a dilation operator. This modified approach is able to eliminate the incorrect pixels (see figure 6.4(d)). Furthermore, the additional operations do not influence the result of the original approach presented in figure 6.1(d).

6.3 Object Segmentation

To segment the image into defect and non-defect areas and to extract information about every defect separately, another binary morphology operator is used: MATLAB's *imfill* [21],

(a) Original α picture

(b) Original mask

(c) Mask after dilation and erosion (closing)

(d) Final mask
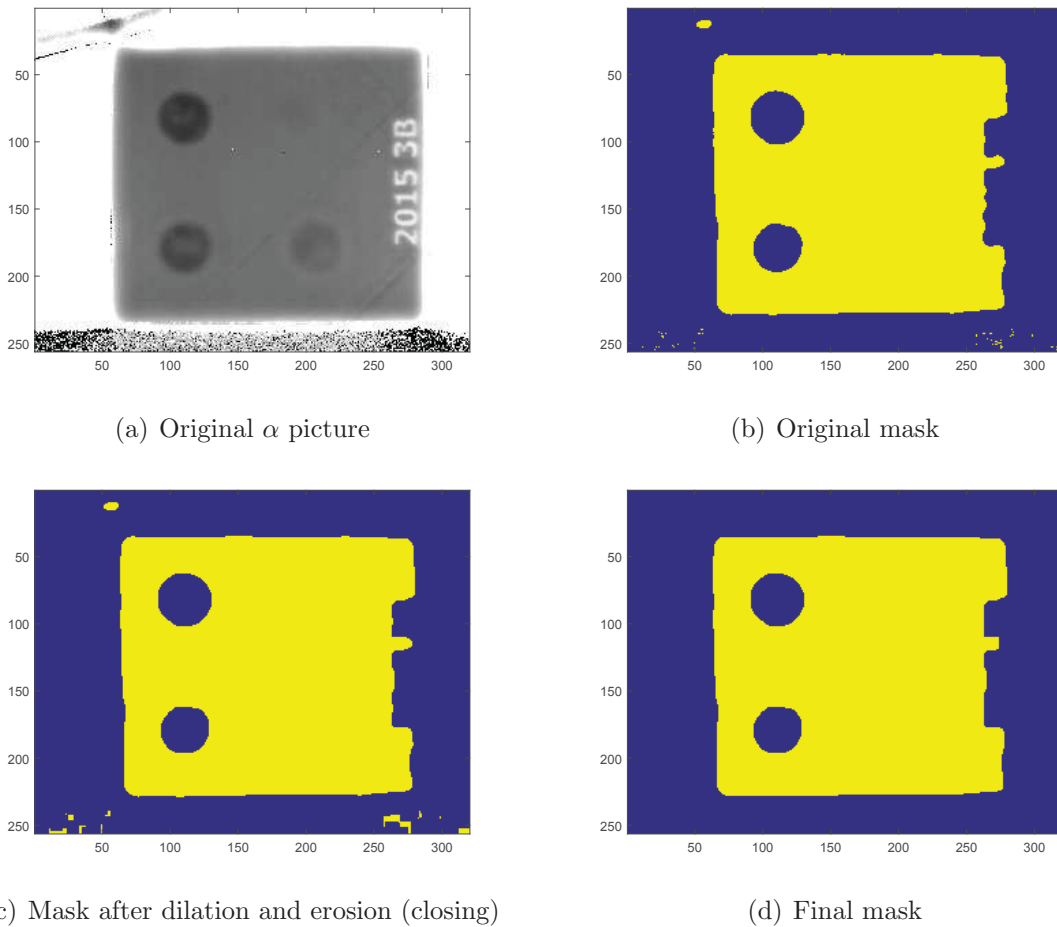
Figure 6.4: Mask handling on the precursor of a 3D printed part (compare chapter 7.3) using additional erosion and dilation functions. Note: In contrast to the previous example in figure 6.1, this measurement was performed in transmission mode.

[39]. This function fills all defects within the specimen in a way that every accumulation of pixels which does not belong to flawless surface and which has no contact to the edge of the image is set to one (where one represents the flawless surface). Through this, the function returns an image with the specimen as a whole or without any defects respectively.

To receive all defects, we just subtract the original mask from the "filled" image [21]. One can observe the result of this step in figure 6.1(e). Assuming that the defects in the sample are separated from each other by flawless material we can apply MATLAB's *bwlabel* ([39]) function to the extracted defects, which will return an image containing the labelled defects. The mask containing the base material and the labelled defects is illustrated in figure 6.1(f).

Through this segmentation it is possible to extract the desired values for every defect separately and continuatively to determine quantitative properties of the defects, such as area (in pixels) or the defect-area-to-sample-area-ratio, or - in case of a reflection measurement - the depth of every defect.

Concluding, attention must be paid to problems using this procedure which can be observed in the presented example:

- As mentioned above, the algorithm is not able to close the open area in the upper, left corner of the sample. This is due to the strongly differing pixel values in this area compared to the rest of the specimen surface. This deflection is most likely the result of a reflection during the measurement. This demonstrates the dependency of this procedure on the stated preconditions. Note: In this specific example this problem does not affect the defect detection but if the aberration in the pixel values yields a mask geometry where those pixels are surrounded by mask pixels and therefore lie *within* the mask, the algorithm would spuriously detect another defect in this area.

- The mask images show that the support (the hold) of the specimen is labelled as the base material of the sample itself. It is a coincidence that the support material - although of completely different dimensions and material properties - yields the same t_w values as the specimen, but this shows that necessary surrounding materials must be chosen carefully or their surface should be treated to receive different values. Ideally, the camera should be positioned so that no material other than the sample can be seen on the record.

- Although the defects (circular holes) are all the same size, they are not entirely correctly detected. This is due to heat diffusion around the edges of those defects, which is not considered in the analytical model. Generally, one can observe that the deeper a defect lies within the specimen the more the edges blur in the resulting images. Therefore, defect size determination becomes more imprecise with increasing defect depth.

- Since small irregularities are eliminated by the dilation procedure, defects need to show a minimum size to be detectable. If we use a kernel size of $n \times n$ in the dilation procedure, a defect must be of the same size or larger to ensure that at least one pixel (which represents a defect) is left after the dilation. Furthermore, the *medfilt2* function can blur the borders of a defect in corner areas and shift those borders by one pixel towards the defect. Thus, a defect must exhibit values outside the base material limits (compare figure 6.3) on a closed area of at least $n + 1 \times n + 1$ pixels (using a dilation kernel size of $n \times n$) to be definitely determinable by the image processing algorithm.

7 Examples

7.1 Twisted CFRP Specimen

A CFRP Specimen from previous experiments presented in [5] was investigated. This specimen consists of five square carbon fibre layers which are rotated to each other and joint together (see figure 7.1). One layer measures 400×400mm with a thickness of 0.5mm.
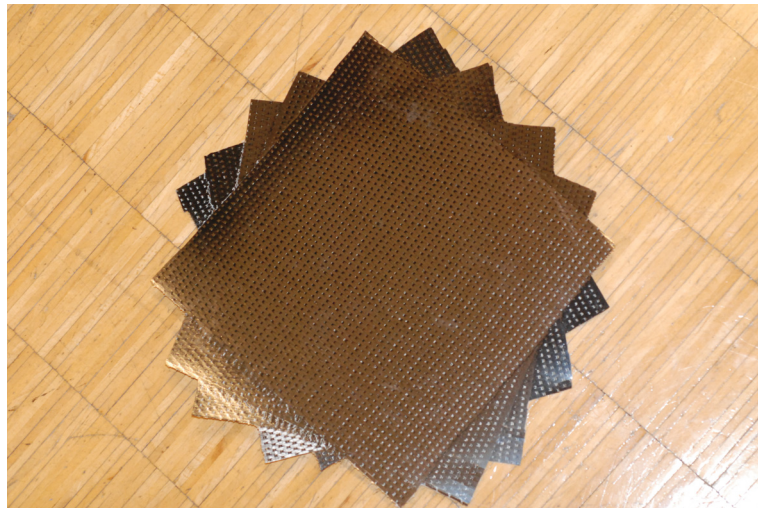
Figure 7.1: Twisted CFRP specimen with five layers

Additionally, five artificial defects in different depths have been placed in this specimen by inserting small PTFE (Teflon) pieces between the layers.

7.1.1 Measurement in Transmission Mode

Performing a flash thermographic measurement in transmission mode on this specimen is to evaluate two properties:

- **Detection of defects:** Since the heat transfer between the layers is partially disturbed due to the PTFE inlays, the heat flow in these areas is lower than in the rest of the specimen. The ability of the evaluation procedure to correctly detect those defects is to be tested.

- **Determination of specimen thickness:** The thickness of different areas of the specimen shall be determined. Since the particular layers are rotated to each other, there are different areas with 1, 2, 3, 4 and 5 layers. The algorithms are applied on such areas.

The two evaluation tasks are carried out using the presented methods (Parker's method and logarithmic method).

First the thermal diffusivity is calculated for each pixel of the record. This is done by assuming a total thickness of 2.5mm. Thus, the thermal diffusivity values are only valid for the mid area of the specimen, where all five layers overlap. The border areas are not considered at this point, only the defects are of interest in this investigation. As figure 7.2 illustrates, the PTFE inlays can be detected very well. Furthermore, the results of the two methods seem to be very similar. Note that the intensity levels are set for best visible contrast; Areas of intensity levels above the chosen maximum or below the chosen minimum are not all the same intensity (although the figure would suggest that).

(a) Thermal diffusivity from Parker's method   (b) Thermal diffusivity from logarithmic method
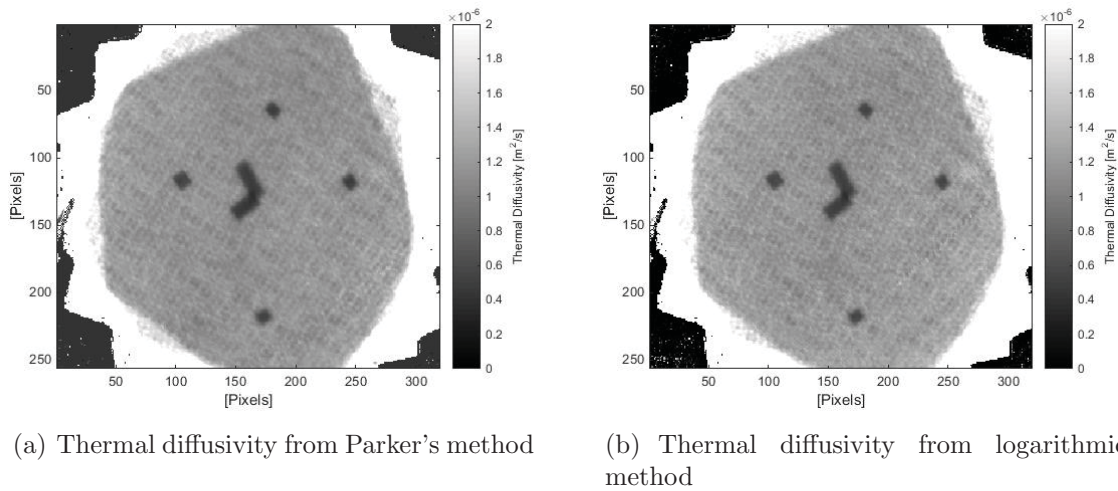
Figure 7.2: Results of the thermal diffusivity computations

To determine the thickness of the specimen and the different areas respectively, the thermal diffusivity needs to be defined. Since this parameter is unknown for this specific specimen, it needs to be evaluated experimentally. This is done by extracting a wide range of defect free area from the logarithmic result and averaging those data points. The hereby received thermal diffusivity coefficient is $\alpha = 1.2153 \cdot 10^{-6} m^2/s$. This measured value differs from the results gained in other, but analogue measurements, compare [9, 10, 33] and table 2.2. Note that differences in the thermal diffusivity of CFRP can be addressed to the high heterogeneity of this material and therefore to different parameters in the production process of such specimens. Thermal diffusivity is therefore influenced by the matrix, the fibre and the composition and structure of those components. It is difficult to compare the structure and

composition of this specimen to the ones used in [9, 10, 33]. Therefore, a direct comparison of the thermal diffusivity results is difficult as well.

Using the received α value, the thicknesses can be calculated for both methods. Figure 7.3 illustrates those results. The different layers (0.5mm each) are very well visible and the calculated thicknesses fit very well to the actual specimen. Also, the difference between the two methods is very small. Again, the intensity boundaries are set, so that the contrast of the different layer thicknesses will be best visible.

(a) Parker's method   (b) Logarithmic method
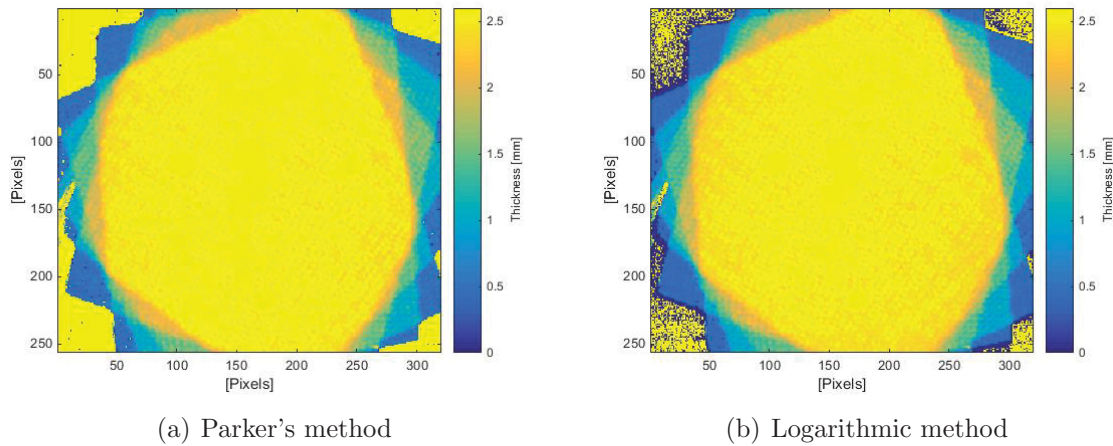
Figure 7.3: Thickness of the sample areas for both methods

Note that in this experiment we compute the thermal diffusivity depending on the thickness of the specimen (in the defect-free area). Using the derived value, we compute the thickness again. This is obviously a loop which does not represent the standard procedure. Usually only one of the presented methods (determination of thermal diffusivity with known thickness or determination of thickness with known thermal diffusivity) is executed. In this specific case, we had to compute the thermal diffusivity first, because this property of the specimen is not exactly known. In a real application, this step would be omitted.

7.1.2 Measurement in Reflection Mode - TSR

The measurement in reflection mode using MATLAB's *polyfit* function (compare chapter 5.3.3) yielded a t_w picture of the CFRP specimen illustrated in figure 7.4.

The process yields acceptable qualitative results. All defects are very well visible, except for the deepest defect (red circle in figure 7.4). However, the quantitative aspect of the results is insufficient. We would expect defects to show much smaller t_w values than the flawless material. The result shows much higher values for most of the defects instead (Note that the values for most of the defects exceed the illustrated color bar in the figure by far). To investigate this issue two pixels have been selected in the result (blue and red marks in
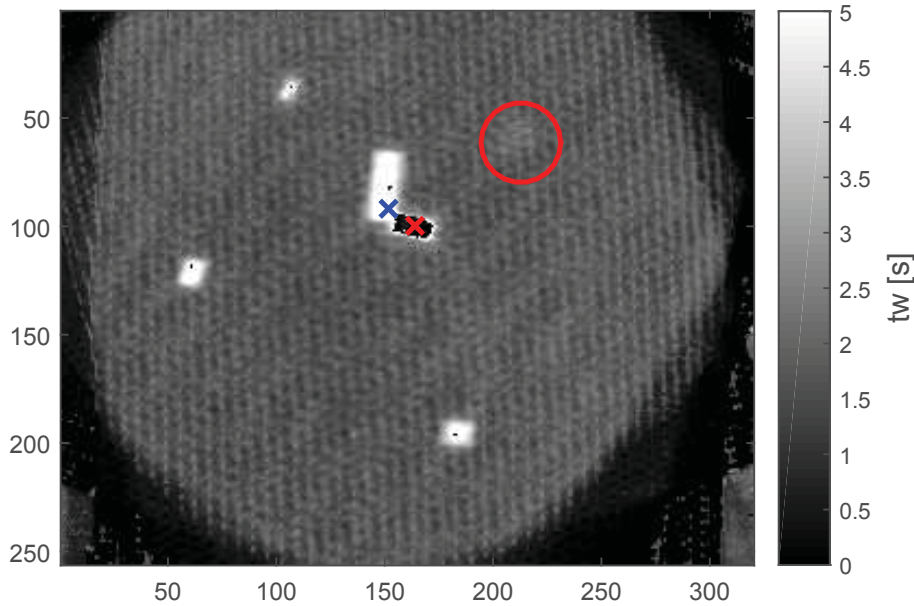
Figure 7.4: t_w picture of the specimen in reflection mode using MATLAB's *polyfit* function, marked pixels used for further investigations

figure 7.4) and their temperature profiles and derivatives are presented in figure 7.5. Note that the colors of the marks in figure 7.4 correspond to the profiles in figure 7.5.

This figure illustrates the temperature profiles of both defects as we would expect it. The problem becomes evident when we consider the fitted polynomials. The polynomials of the red profile is fitted well, which corresponds in a reasonable value for t_w (compare figure 7.4). But the polynomial of the blue profile highly deflects at the begin. This yields in a biased second derivative as illustrated in figure 7.5(c). This is the reason for the incorrect results. However, although those results can not be used in quantitative matter, they provide suitable qualitative information about the defects within the specimen.

The same measurement was evaluated using the DOP fitting. The difference picture and the resulting t_w picture are illustrated in figure 7.6.

Both pictures show very good qualitative results. All defects are visible very well, distinct from the flawless material and sharply edged, except for the deepest defect (marked with a red circle in the t_w picture). The t_w values in figure 7.6(b) do not show the same problems as in the t_w picture of the *polyfit* fitting (figure 7.4). As we would expect, the t_w values at the defects are much smaller than at flawless material. However, to investigate the results in more detail, four pixels have been selected to extract the temperature profile and the corresponding polynomials. The temperature profiles, fitted polynomials and their derivatives are illustrated in figure 7.7.
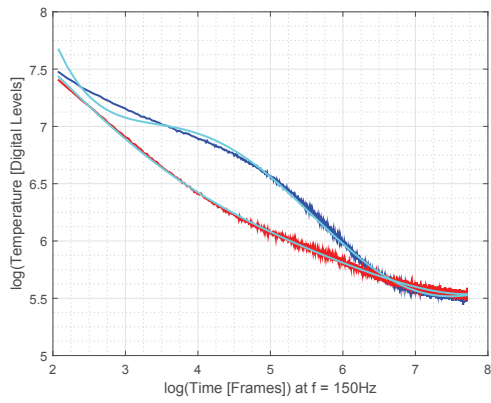
(a) Temperature profiles and the fitted polynomials
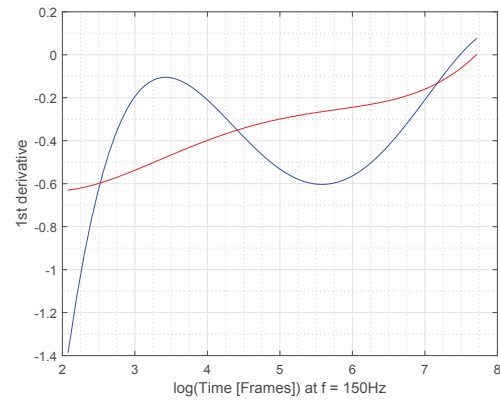
(b) First derivative of the fitted polynomials
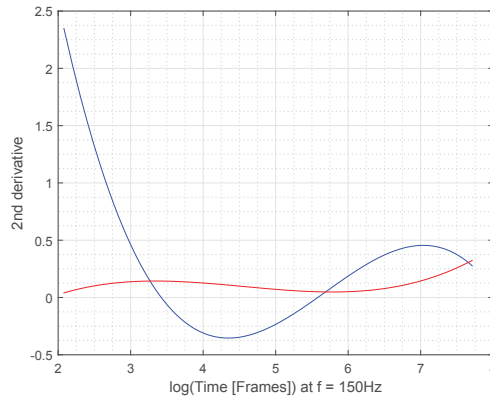
(c) Second derivative of the fitted polynomials

Figure 7.5: Temperature profiles, fitted polynomials and their second derivatives of selected pixels (corresponding to figure 7.4)
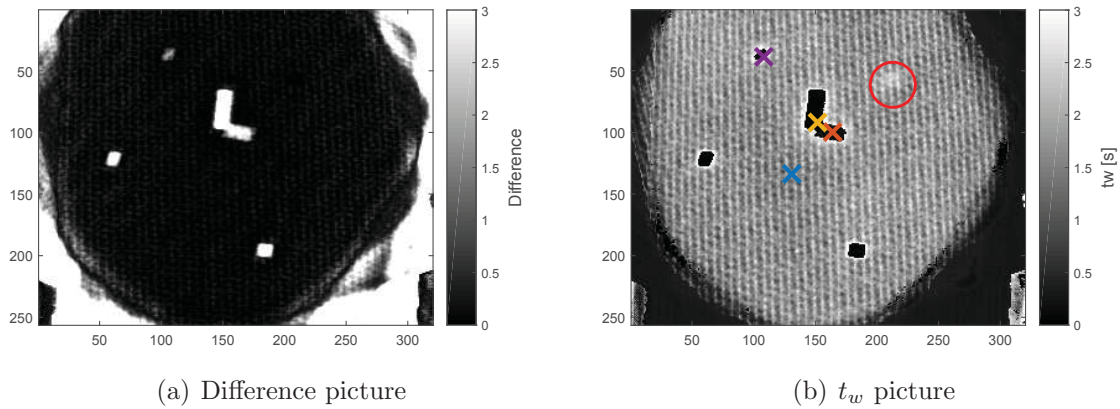
(a) Difference picture

(b) t_w picture

Figure 7.6: Results of the evaluation using DOP fitting
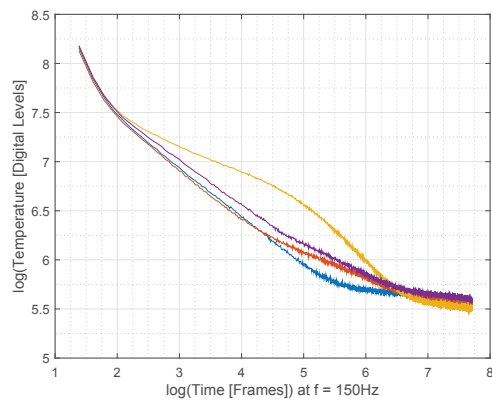
(a) Temperature profiles
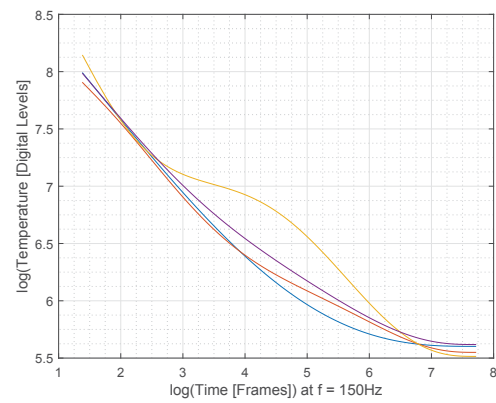
(b) Fitted polynomials
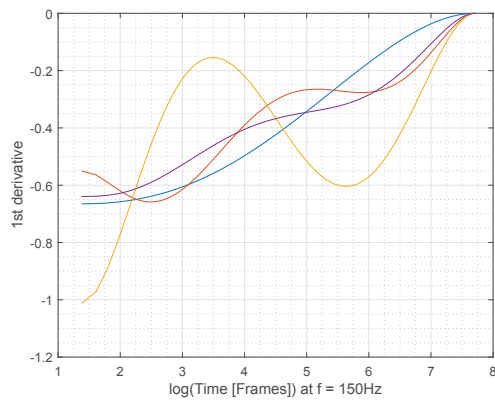
(c) First derivatives
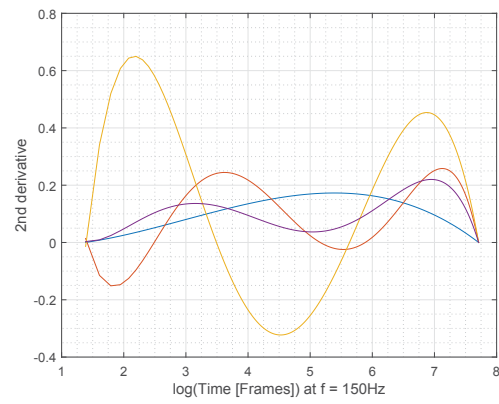
(d) Second derivatives

Figure 7.7: Extracted temperature profiles from figure 7.6(b)

Figure 7.7(a) shows a problem: the profiles do not start with a slope of -0.5 but with a more negative slope. This can be addressed to the abating flash. A possibility to avoid this corruption is to increase k_{EoF} closer to -0.5 (in this specific case -0.7 instead of -1, compare section 5.3.1), which will move t_{EoF} backwards. But if we consider figure 7.7(a), we can see that almost at the same time the first derivative of the profile declines to -0.5, the yellow temperature profile turns towards a plateau, which represents a defect. If we move t_{EoF} in the mentioned way, the curvature to the plateau will decline and the first maximum in the second derivative of the yellow profile (compare figure 7.7(d)) will disappear. Thus, we will lose information about the shallow defect. This means, it is always necessary to do a trade off between reducing the flash influence and ensuring the detectability of shallow defects. However, figure 7.7(b) indicates that due to the constraints used in the DOP fitting, the (too) negative slope in the recorded data does not influence the fitted polynomial.

Note that for this evaluation the difference limit, which is used to distinguish between flawless and defect pixels and choose the appropriate polynomial (compare equation (5.18) in chapter 5.3.4), is modified. This means that n_{std} is set to $n_{std} = 10$.

To compare the results of the *polyfit* and the DOP approach more closely, figure 7.8 provides an illustration of the polynomial fitting and the derivatives of the selected pixels marked in figure 7.4.

This example also illustrates the differences between local and global t_{EoF} determination. Although we use the same pixels for the investigations of the *polyfit* and the DOP approach, the local t_{EoF} determination used in the *polyfit* method yields a higher (later) t_{EoF} than the global determination in the DOP computation. The reason for this difference can be found in the different smoothing methods (compare chapter 5.3.1).

For further qualitative investigations, the values of the second derivatives at certain points in time are illustrated in the figures 7.9 and 7.10. Figure 7.9 shows the second derivatives of the polynomials generated by the *polyfit* approach, as well as of the polynomials, which have been selected due to the difference limit (compare section 5.3.4), generated by the DOP approach. Since we are looking for defects, we also compute the second derivative pictures of the DOP polynomials of higher degree exclusively, since those polynomials are supposed to represent a defect (compare section 5.3.4). Those pictures are illustrated in figure 7.10. Both figures illustrate, that all defects (even the deepest one) can be detected within a picture of second derivatives at certain points in time.

For detailed quantitative investigations, figure 7.11 illustrates the thickness/depth picture generated by the DOP approach, together with a number of marked pixels. The actual values of those pixels (extracted from the according thickness/depth picture in a range of 5×5 pixels around the marked pixel) are summarized in table 7.1 for both approaches. This summary shows, that DOP approach is better suited for quantitative investigations (in case

(a) Fitted polynomials

(b) First derivatives

(c) Second derivatives
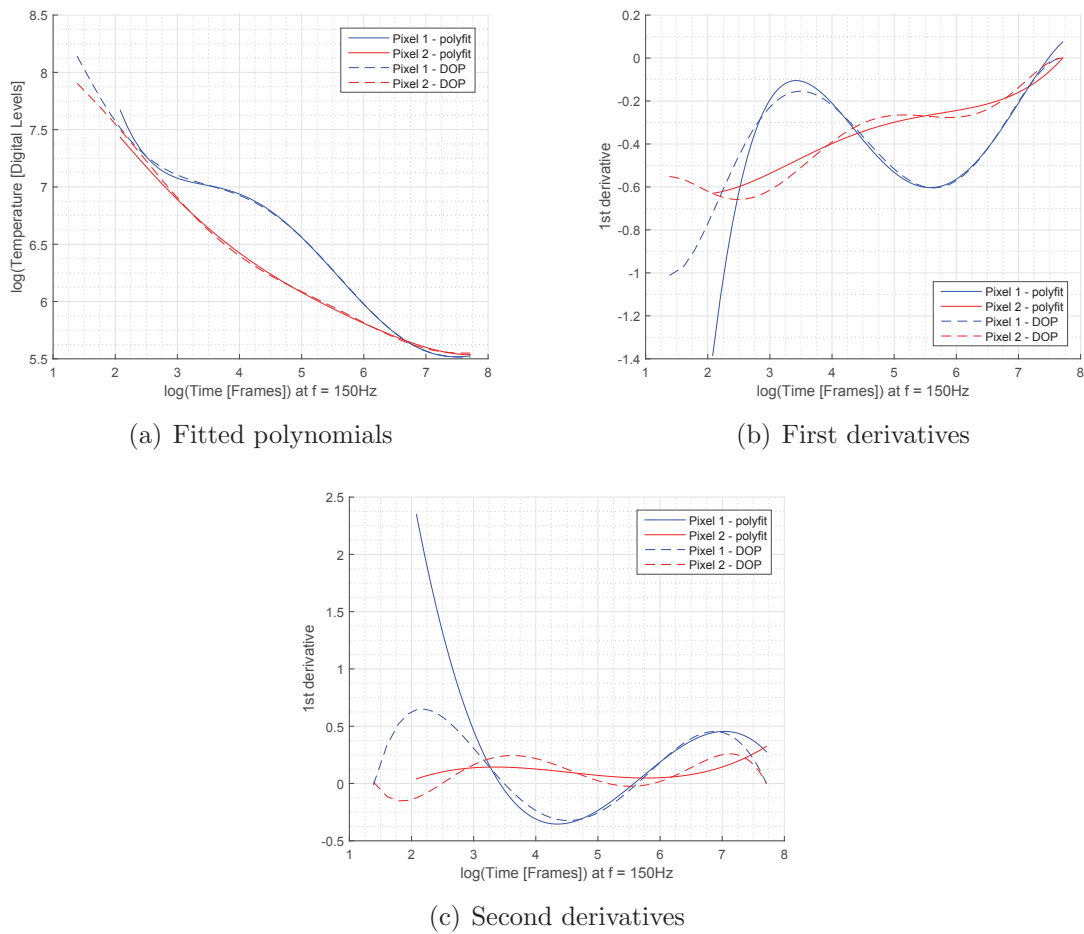
Figure 7.8: Comparison of the polynomial fitting and the derivatives between the *polyfit* and DOP approach
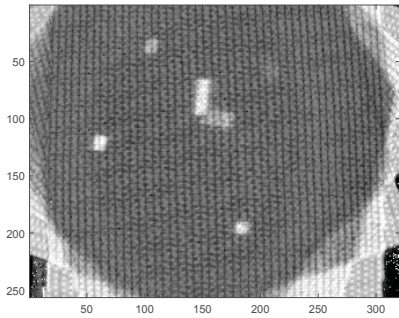
(a) *polyfit*: 0.1339s
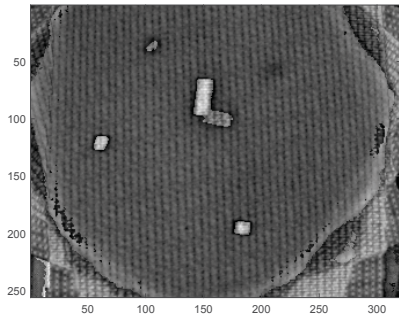
(b) DOP: 0.1339s
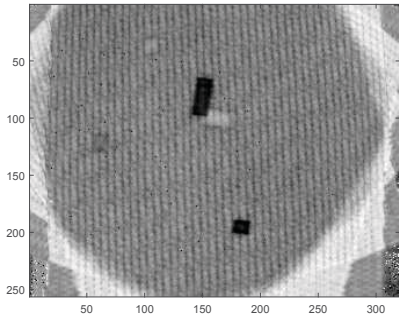
(c) *polyfit*: 0.2696s
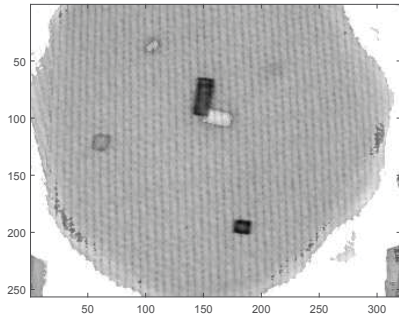
(d) DOP: 0.2696s
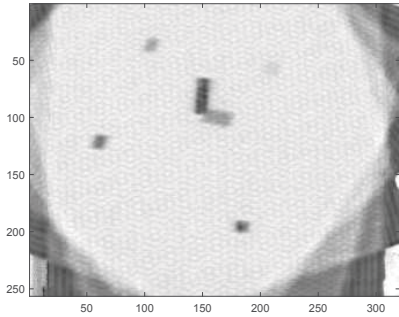
(e) *polyfit*: 1.4760s
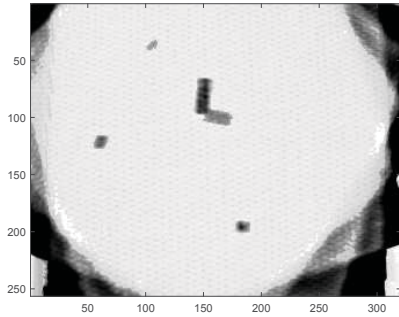
(f) DOP: 1.4760s
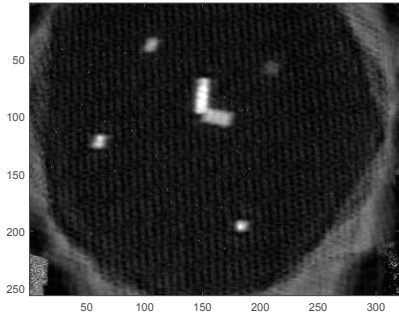
(g) *polyfit*: 12.0536s
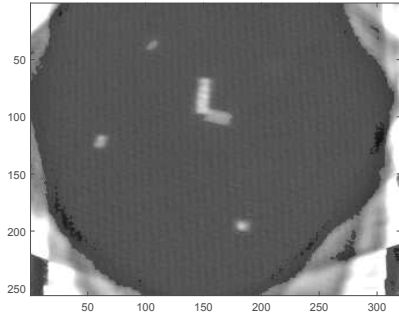
(h) DOP: 12.0536s

Figure 7.9: Second derivatives at certain points in time for *polyfit* and DOP polynomials

(a) 0.1339s

(b) 0.2696s

(c) 1.4760s

(d) 12.0536s
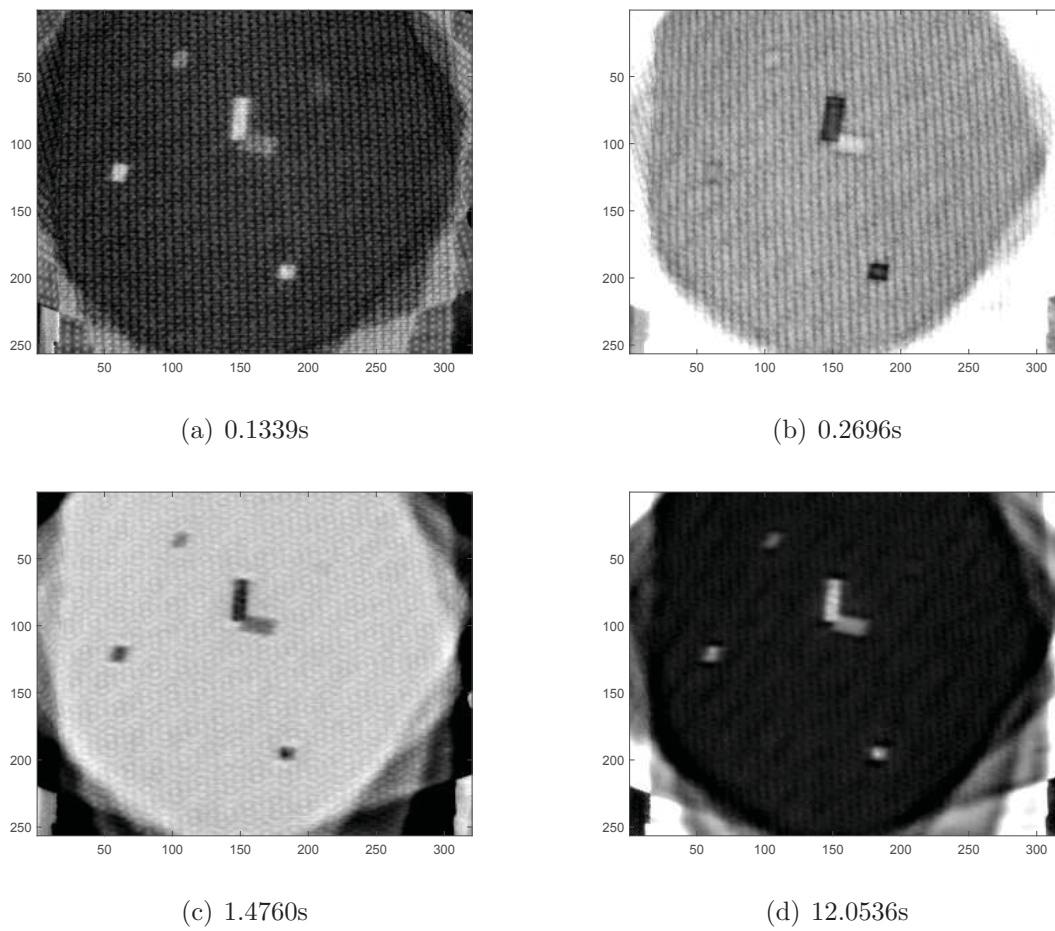
Figure 7.10: Second derivatives at certain points in time for DOP polynomials used for the representation of defects

of this specific specimen) than the *polyfit* approach (although the DOP approach returns biased values as well).
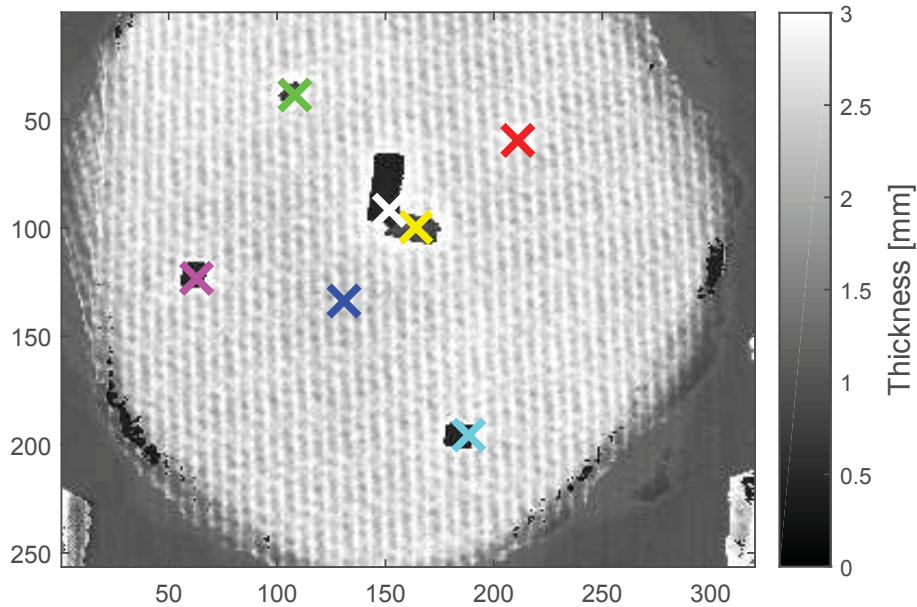
Figure 7.11: Thickness picture of the specimen in reflection mode, values of the marked pixels are presented in table

Marked Defect	Thickness/Depth [mm]		
	Specimen	polyfit	DOP
Blue	2.5	2.44	2.36
Yellow	1.5	1.09	1.00
White	0.5	5.48	0.47
Green	1.5	4.27	1.01
Magenta	1.0	5.42	0.51
Cyan	0.5	4.46	0.46
Red	2.0	2.92	3.04

Table 7.1: Summary and comparison of the results between MATLAB's *polyfit* and the DOP approach

7.1.3 Measurement in Reflection Mode - PPT

The performed measurement described above was also evaluated using the PPT evaluation presented in chapter 5.4. The result of this evaluation is illustrated in figure 7.12.

(a) Phase image at f = 0.0658Hz

(b) Phase image at f = 0.132Hz

(c) Phase image at f = 0.197Hz

(d) Phase image at f = 0.263Hz

(e) Difference Accumulation

(f) Value Accumulation
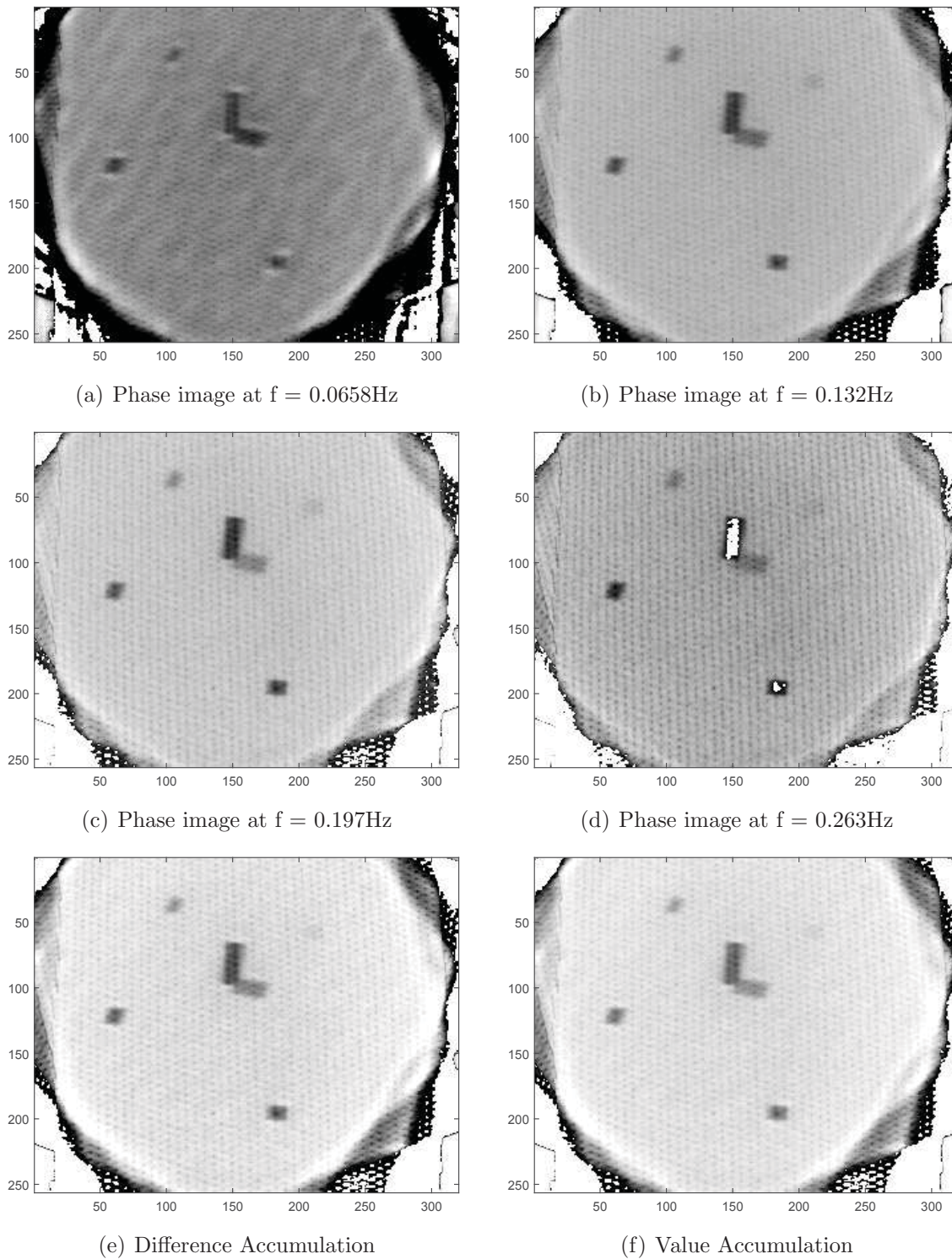
Figure 7.12: Results of the PPT evaluation

As described in section 5.4, the detectability of deeper defects decreases with the investigated frequency. However, in this example the detectability of deep defects only slightly changes with the frequency. Still, it is to record that the deepest defect (at the upper right, marked in cyan in figure 7.13) is basically not visible. Only in the second and third phase image there is a slight indication of the inlay. The fourth phase image (figure 7.12(d)) shows positive phase shift values (compared to the negative values in the remaining image) for the defect in the middle of the specimen (marked in green in figure 7.13). This is because around this frequency the phase angles start to change sign. A phase image at a higher frequency (for instance 0.526Hz, four frequency increments further) the phase shift is positive across the entire image. Therefore, only the first three phase images have been used for the accumulation computations.

Unfortunately the illustrated images in this hard copy do not represent the relation between flawless surface and defects properly. Comparing the sub figures in figure 7.12 implies that

1. the contrast between flawless material and defects in the image is less than it actually is and

2. there is not much of a difference between the phase images and the Difference Accumulation.

Therefore, those results are investigated more closely. Figure 7.13 shows the result image of the Difference Accumulation including selected areas on the surface (interactively selected by a user) which are used to compare the different result images in the following section.

Each marked point in the figure represents a selected pixel. For every pixel there was a 5×5 matrix extracted symmetrically around the pixel from every result image (all chosen phase images, the Difference Accumulation image and the Value Accumulation image). To reduce the influence of noise the average of every of those 25 value sets was computed. This average is supposed to represent the value for the selected area (the selected pixel, respectively). All of those values are summarized in table 7.2.

The table shows that the difference values for the defects, computed using the Difference Accumulation, differ significantly from the ones of the flawless material - observable by the ratio for each defect. Even defect five, which is barely visible to the naked eye, exhibits a much bigger ratio in the Difference Accumulation image compared to the other result images. Through this it is much easier to separate defects from the remaining material. An objection to this approach could be, that the ratio of defect to flawless material is of course high, because of the calculation process itself. The algorithm subtracts the mean phase shift value of the flawless material from every pixel. Thus, the value of all the pixels of the base material will be around zero. Through this the ratio computation is a division
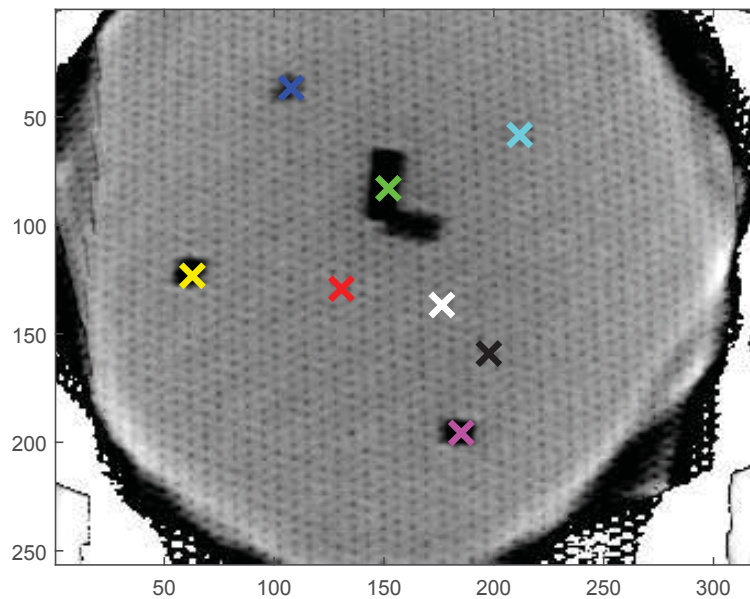
Figure 7.13: Result image of the Difference Accumulation, compared pixels are marked, results are summarized in table 7.2

by values close to zero and every small fluctuation will cause a big change of the ratio. To investigate this problem two reference points have been chosen on the flawless surface in the Difference Accumulation image. Since those reference points represent the same material as the first measurement point, one can expect the ratio to be close to one. In fact, the values of the reference points differ about 10% (reference 1) and 30% (reference 2) from the first measurement. This aberration can be addressed to the noise which influences the computed ratio in the way described above. However, even defect five indicates a much bigger deviation in the ratio than 10% or 30%.

Thus, although the computed ratio in the Difference Accumulation image is subject to high noise, actual (and even very deep) defects yield a much higher change in this ratio than the noise.

7.2 Flat Bottom Hole Depth in Steel Plate

This specimen is a steel plate of the dimensions $200 \times 100 \times 8.6$mm with a total of 12 drill holes located in two rows with six holes each. The specimen is illustrated in figure 7.14.

The diameters of the drill holes are 8mm for the holes of the upper row and 10mm for the holes of the lower row. The depth of the holes are 5.6mm, 4.6mm, 3.6mm, 2.6mm, 1.6mm and 1mm from the very left column to the very right. This yields a remaining material

		1. Phase	2. Phase	3. Phase	Differ. Accum.	Value Accum.
Material/red	Phase	-0.5557	-0.7440	-0.9718	-0.0396	-2.2716
Defect 1/green	Phase	-0.6886	-1.1235	-1.4195	-0.9996	-3.2316
	Ratio	1.2391	1.5100	1.4606	25.2603	1.4226
Defect 2/blue	Phase	-0.6255	-0.9306	-1.1403	-0.4645	-2.6965
	Ratio	1.1256	1.2508	1.1734	11.7375	1.1870
Defect 3/yellow	Phase	-0.6723	-1.0471	-1.2929	-0.7803	-3.0123
	Ratio	1.2098	1.4073	1.3304	19.7201	1.3261
Defect 4/magenta	Phase	-0.6722	-1.0852	-1.3804	-0.9058	-3.1378
	Ratio	1.2096	1.4585	1.4205	22.8911	1.3813
Defect 5/cyan	Phase	-0.5237	-0.7971	-1.0249	-0.1137	-2.3457
	Ratio	0.9424	1.0713	1.0547	2.8729	1.0326
Reference 1/white	Phase	-0.5406	-0.7455	-0.9825	-0.0367	-2.2687
	Ratio	0.9728	1.0020	1.0110	0.9267	0.9987
Reference 2/black	Phase	-0.5334	-0.7426	-0.9846	-0.0287	-2.2607
	Ratio	0.9599	0.9981	1.0132	0.7244	0.9952

Table 7.2: Comparison of different result images for all five defects of the specimen. Every defect is marked in figure 7.13 and the corresponding color is assigned in the first column of the table. "Phase" relates to the corresponding phase shift value of the specific defect in the specific result image (phase images one to three correspond to the images in figure 7.12 (a) to (c)). "Ratio" is the ratio of the phase shift value of the specific defect to the phase shift value of the flawless material in the corresponding result image.

thickness under the drill holes of 3mm, 4mm, 5mm, 6mm, 7mm, 7.6mm from the very left to the very right.

To increase the emissivity, both sides of the specimen have been painted black.

The purpose of the measurements was primarily to determine the depth of the holes (or the remaining plate thickness, respectively) in transmission and reflection mode.

7.2.1 Measurement in Transmission Mode

The Parker's method and the logarithmic method for transmission mode have been used for this specimen. First of all, the logarithmic method is used to compute the thermal diffusivity α of the ground material, because this parameter highly varies depending on the exact composition of the material. Since this composition is not exactly known, we could not rely on any value from the literature, but had to measure the thermal diffusivity ourselves (similar to section 7.1.1). Through this problem, this experiment does not prove the ability of the evaluation algorithms to identify the thermal diffusivity, but the determination of the depth of the holes compared to the base material (and therefore the difference in the material
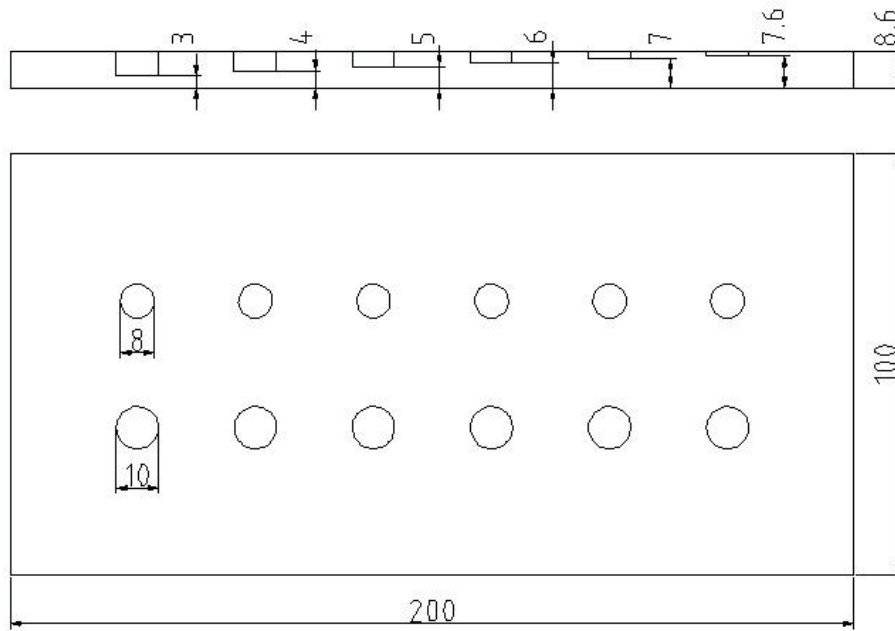
Figure 7.14: Test specimen, technical illustration

thickness) is not influenced by a deviant thermal diffusivity value. The hereby received value for the thermal diffusivity is $\alpha = 8.4966 \cdot 10^{-6} m^2/s$, which is in good agreement with similar materials (tool steels), compare [12] or table 2.2.

The results of the evaluations for both transmission methods (Parker's and logarithmic method) are illustrated in figure 7.15.
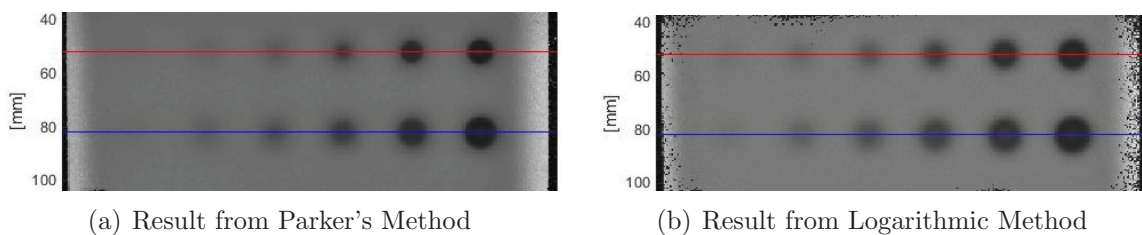
(a) Result from Parker's Method

(b) Result from Logarithmic Method

Figure 7.15: Evaluation results of the test specimen: The pixel intensities (brightness) represents the material thickness under the particular pixel. Note: Since the specimen surface with the drill holes was turned to the flash light, those results of the specimen are flipped along the vertical axis compared to figure 7.14. The inserted lines mark the cross sections which were taken for further evaluation.

For a more detailed evaluation, the pixel values along the two marked lines were extracted and plotted in figure 7.16.

Those results yield the following conclusions:

- Both methods provide very good estimations of the thickness of the base material.
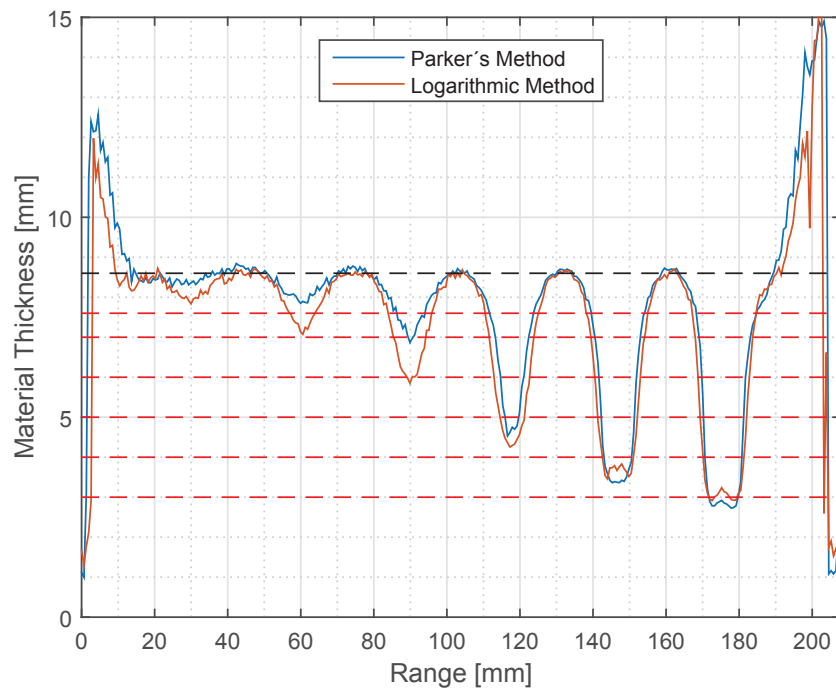
(a) Results for flat bottom holes with 8mm diameter (Upper Line)
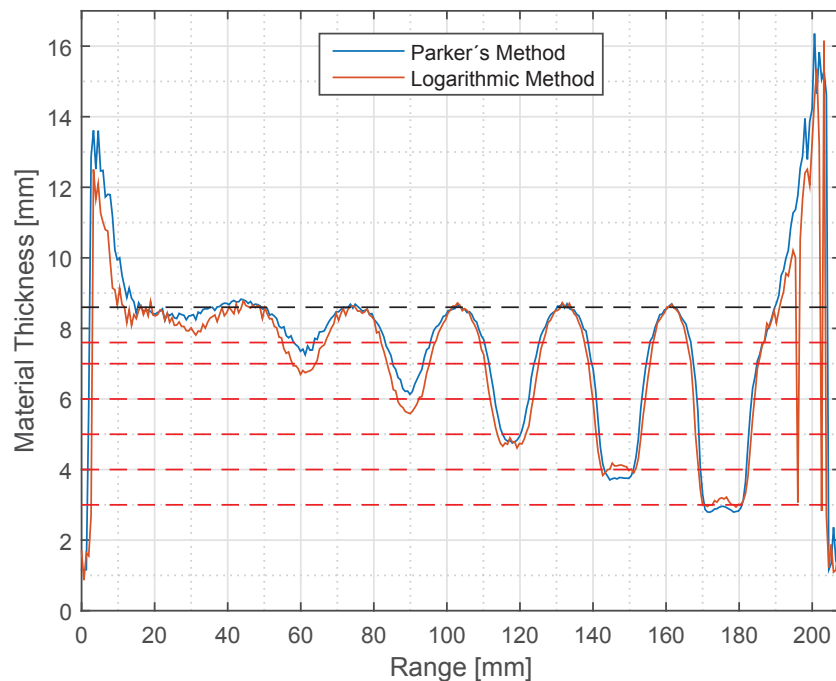
(b) Result for flat bottom holes with 10mm diameter (Lower Line)

Figure 7.16: Results of the evaluations in detail for both marked lines from figure 7.15. The black dotted line represent the specimen thickness (8.6mm), the red dotted lines represent the remaining material under the holes (and therefore the complementary value to the depth of the different holes) along the marked lines from 3mm to 7.6mm.

- The logarithmic method is more sensitive to shallow holes and thicker material respectively. This is best observable for the two very left drill holes.

- The logarithmic method represents changes in the thickness better than the original Parker's method, which leads to a sharper edge indication. This is best observable for the two most right drill holes of the upper line result

7.2.2 Measurement in Reflection Mode - TSR

Measuring the specimen in reflection mode using MATLAB's *polyfit* function (compare chapter 5.3.3) yielded a result illustrated in figure 7.17. The values in this result picture represent the thickness of the material and the remaining wall thickness ("thickness picture") respectively.
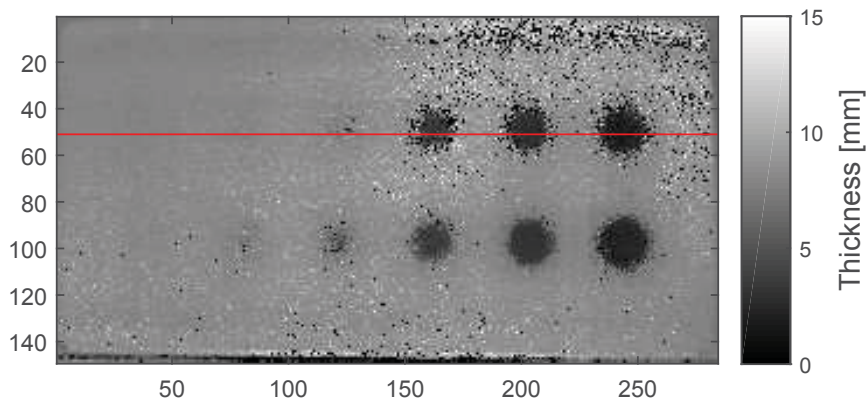
Figure 7.17: Resulting thickness picture from reflection measurement of the steel plate using MATLAB's *polyfit* function; Red horizontal line for quantitative comparison

In this figure, the three deepest defects are visible very well. Their size (diameter) is represented in an acceptable accuracy. The representation of the hole depth (remaining wall thickness respectively) is investigated in more detail in figure 7.24. However, there are obviously a number of outliers, especially in the upper right area of the picture. Some of those outliers show very small values (often zero), some very high values (often higher than the flawless material). Pixels of such values have been investigated more closely. Therefore one pixel with apparently high thickness and one pixel with apparently small thickness have been selected within the noisy area of the specimen. Their temperature profiles and the according second derivatives are illustrated in figure 7.18.

Figures 7.18(a) and 7.18(c) suggest good fitting. However, one can observe that the y-axis values of the polynomials increase again at the end of the profile, although the physical model forbids such an increase. This is the outcome of a bad polynomial fitting due to noise.
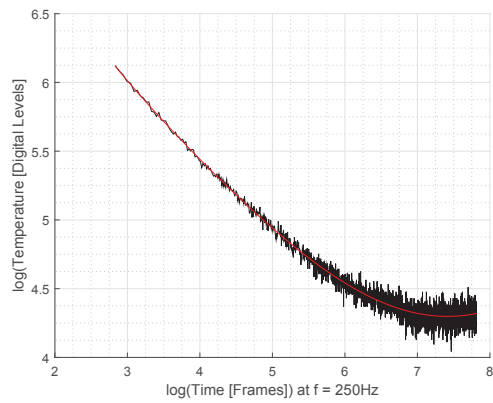
(a) Temperature profile, pixel with apparently high thickness
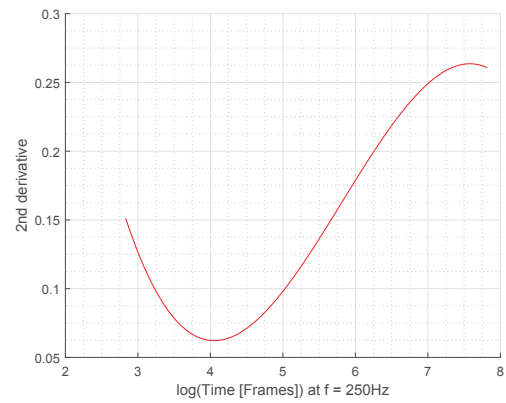
(b) Second derivative, pixel with apparently high thickness
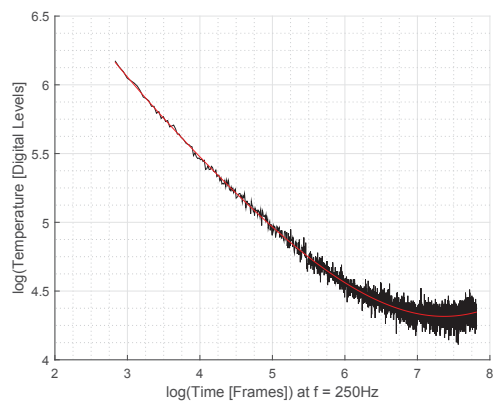
(c) Temperature profile, pixel with apparently low thickness
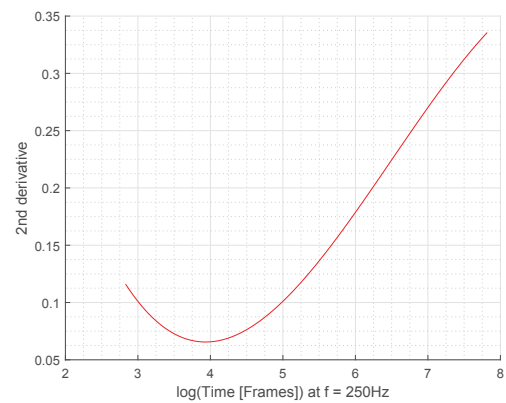
(d) Second derivative, pixel with apparently low thickness

Figure 7.18: Temperature profiles and according derivatives of selected pixels (within the noisy area) from MATLAB's *polyfit* result with incorrect evaluated values

The consequences of this bad fitting can be observed in the figures 7.18(b) and 7.18(d). The curvature of the polynomial in figure 7.18(c) remains till the end of the profile (instead of decrease to zero, compare figure 4.8(b)), thus we can not determine a maximum in the second derivative in figure 7.18(d) (in such a case the algorithm sets the result to zero). For the same reason we can observe a maximum in the second derivative of the first temperature profile (figure 7.18(a)), but again due to the rising polynomial at the end of the profile, this maximum occurs too late. This is why the thickness value of this pixel seems to be higher than the surrounding flawless material.

The results from the DOP fitting are illustrated in figure 7.19.
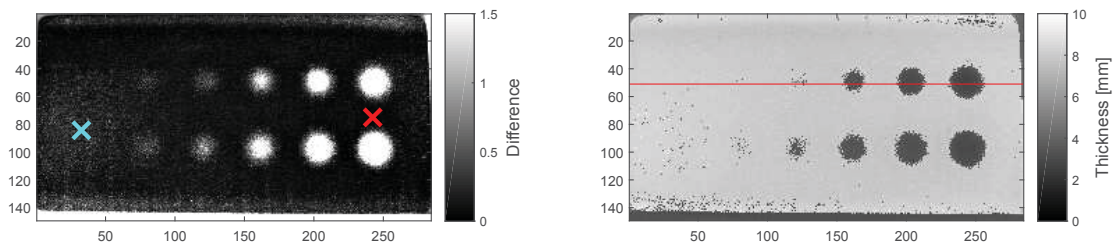
(a) Difference picture, two pixels selected for comparison

(b) Thickness picture

Figure 7.19: Results of the evaluation using DOP fitting

The difference picture shows very good qualitative results. All holes, except for the shallowest, can be detected. However, the diameter of the holes seems to be overestimated, and the clearness of the defects drops with increasing remaining wall thickness. The difference picture reveals another problem: There seems to be much noise in the left part of this picture. This means higher differences between the two fitted polynomials in this region. To investigate the cause for the varying differences within the result, two pixels have been selected (compare figure 7.19(a)) to compare the data of different areas. Figure 7.20 compares the temperature profiles and the fitted polynomials (both degrees for flawless material and defects).

We can clearly see that the difference between the two polynomials is much less in figure 7.20(b) than in figure 7.20(a). This can be addressed to the temperature data itself. If we consider both temperature profiles at about 6.5 and higher on the x-axis, we can see that the data in figure 7.20(b) seems to form a plateau as we would expect, while the data in figure 7.20(a) seems to keep slightly decreasing towards the end. Since the temperature profiles of pixels in the left region of the specimen seem to underlie the same problem, we can address this phenomenon to an external influence, such as a reflection from a surrounding surface or

(a) Noisy pixel, cyan in figure 7.19(a)

(b) Homogeneous pixel, red in figure 7.19(a)
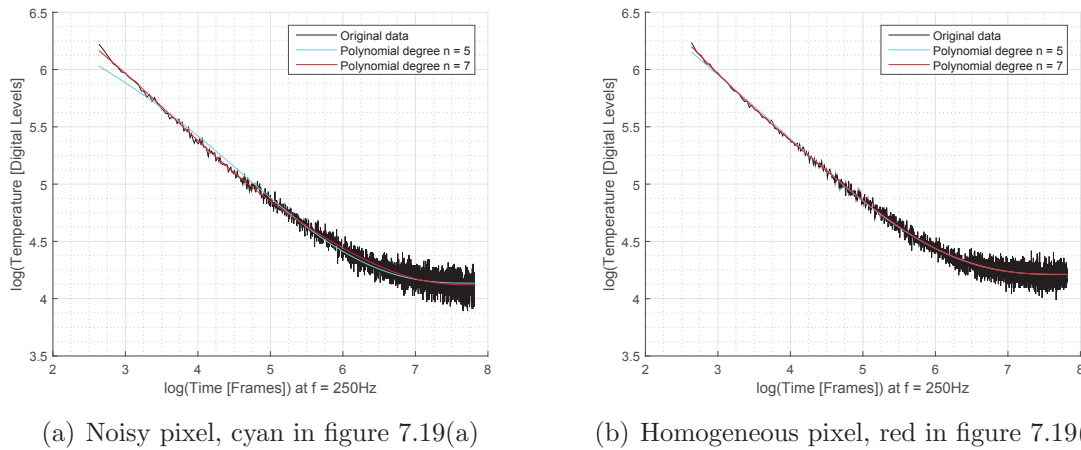
Figure 7.20: Comparison of temperature profiles and fitted polynomials of a pixel in a noisy region and a pixel in a homogeneous region

inhomogeneous heating or cooling.

The thickness picture in figure 7.19(b) shows good results as well (quantitative investigation in figure 7.24), but it suffers the same problem as the difference picture in the left region of the picture (since the results from the difference picture are used to choose the correct polynomial for the t_w determination). A possibility to come by this problem in the evaluation process is to decrease the sensitivity to noise. We can do this by increasing n_{std} in the difference limit determination (compare chapter 5.3.4). Note that n_{std} was set to $n_{std} = 10$ in the presented example. With decreasing sensitivity to noise, the sensitivity to deep defects (shallow holes) decreases as well. To illustrate this two, results with different n_{std} are presented in figure 7.21.

(a) Thickness picture, $n_{std} = 5$

(b) Thickness picture, $n_{std} = 20$
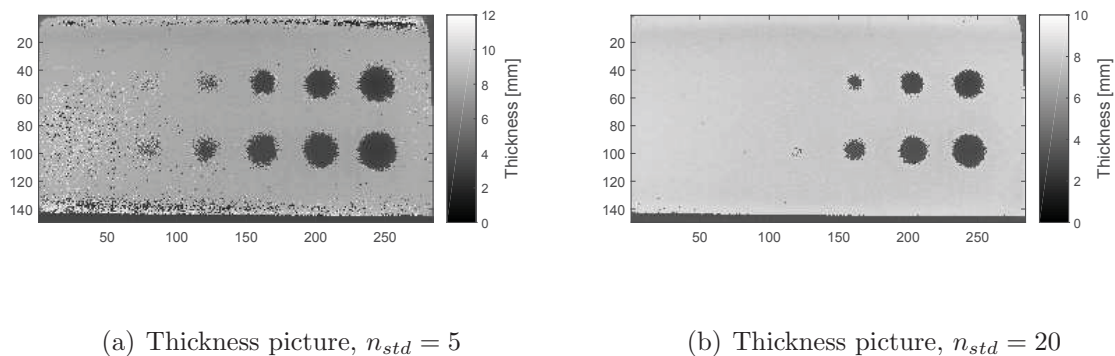
Figure 7.21: Evaluation results using different n_{std}

This figure illustrates again the trade off between detectability of deep defects (shallow holes) and noise influence when optimizing the parameters.

For further qualitative investigations, the values of the second derivatives at certain points in time are illustrated in the figures 7.22 and 7.23. Figure 7.22 shows the second derivatives of the polynomials generated by the *polyfit* approach, as well as of the polynomials, which have been selected due to the difference limit (compare section 5.3.4), generated by the DOP approach. Since we are looking for defects in general and for the holes in this specific case, we also compute the second derivative pictures of the DOP polynomials of higher degree exclusively, since those polynomials are supposed to represent a defect (compare section 5.3.4). Those pictures are illustrated in figure 7.23. Both figures illustrate, that all holes, except for the most left column, can be detected very well within a picture of second derivatives at certain points in time. However, in case of the DOP approach, the evaluation of the polynomial of higher degree yields better results.

To investigate and compare the quantitative results from the *polyfit* evaluation and the DOP evaluation, we extract the thickness values from the corresponding thickness pictures (figure 7.17 and figure 7.19(b)) along the marked lines and plot them in a separate chart in figure 7.24.

For the illustration in this chart, the pixel values along the lines have been smoothed using MATLAB's *smooth* function, to reduce the noise influence. The chart indicates, that both methods tend to represent the material thickness too small. Noise seems to influence the *polyfit* approach more than the DOP procedure. However, in terms of defect depth (hole depth) determination both methods do not yield feasible results. Nevertheless, both methods are able to give a qualitative statement about the depth of the defects relatively to each other. Note that especially the DOP method is highly influenced by its parameters. In case of a real application for a limited range of test objects (in terms of geometry, material, expected defects, ...) these parameters need to be optimized for those specimen. This allows us to expect better results.

7.2.3 Measurement in Reflection Mode - PPT

The performed measurement described above was also evaluated using the PPT evaluation presented in chapter 5.4. The results of this evaluation are illustrated in figure 7.25.

Those results confirm the expected results stated in chapter 5.4. With increasing frequency, the phase image becomes less sensitive to deeper defects. Note that the Difference Accumulation and the Value Accumulation computations have been carried out using the four phase images illustrated in figure 7.25. Compared to chapter 7.1.3, both accumulated images exhibit a higher contrast between defects and flawless material than it is the case for the CFRP specimen. However, to compare the results of the different outputs, the same investigation as presented in chapter 7.1.3 is performed. The results are again illustrated in figure 7.26 and summarized in table 7.3.

(a) *polyfit*: 0.0981s

(b) DOP: 0.0981s

(c) *polyfit*: 0.4860s

(d) DOP: 0.4860s

(e) *polyfit*: 1.6137s

(f) DOP: 1.6137s

(g) *polyfit*: 4.3865s

(h) DOP: 4.3865s
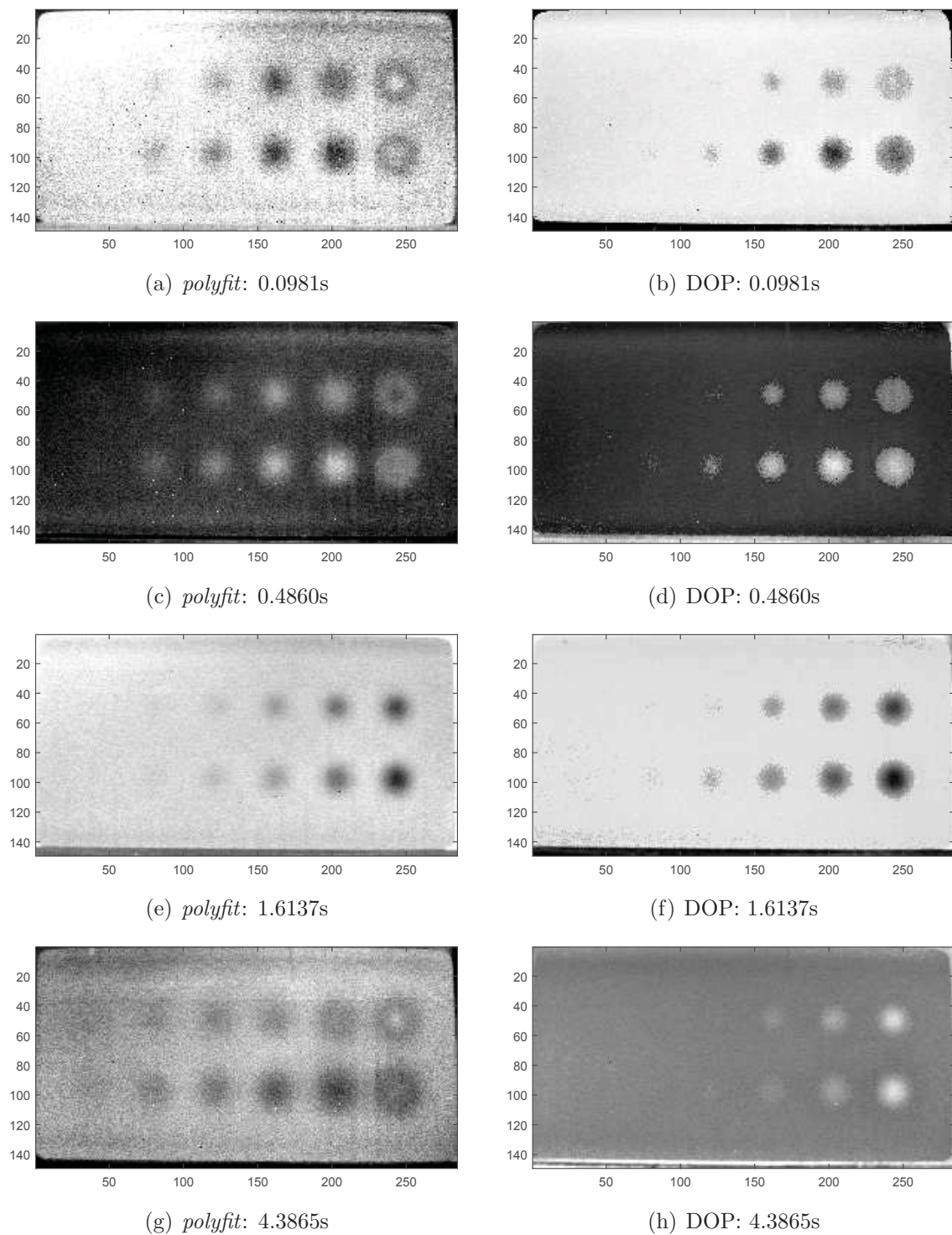
Figure 7.22: Second derivatives at certain points in time for *polyfit* and DOP polynomials

(a) 0.0981s

(b) 0.4860s

(c) 1.6137s

(d) 4.3865s
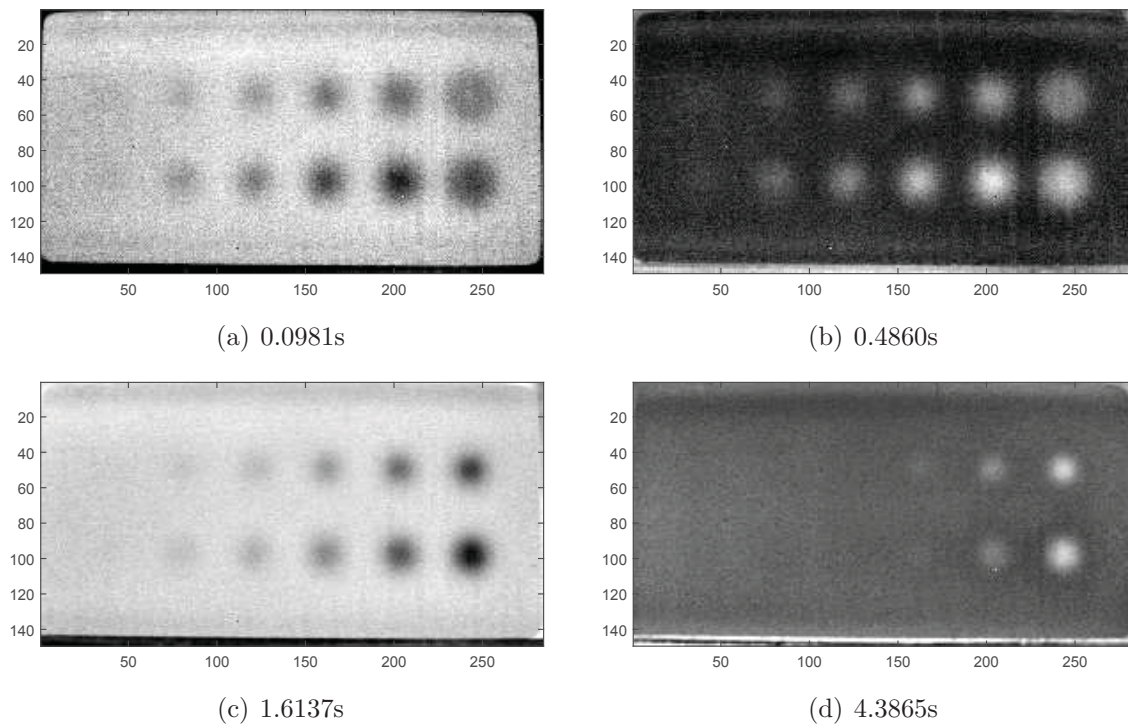
Figure 7.23: Second derivatives at certain points in time for DOP polynomials used for the representation of defects
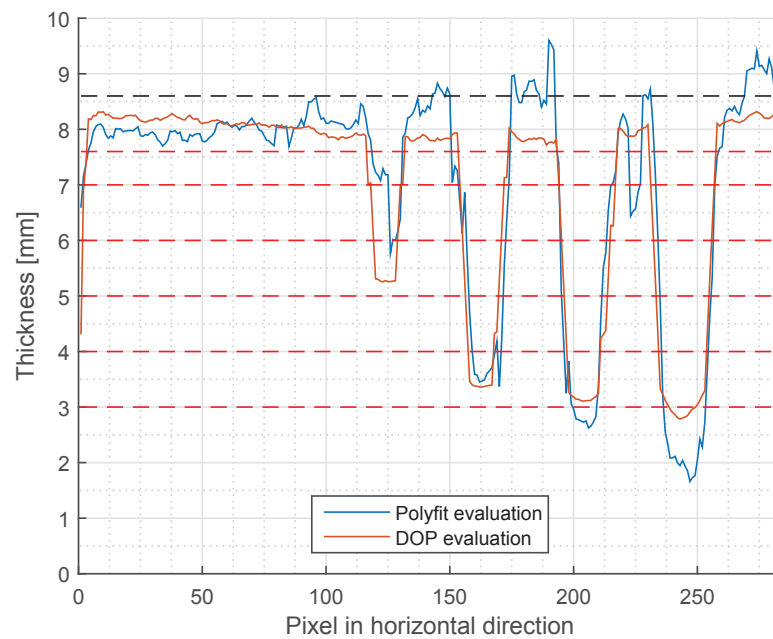
Figure 7.24: Comparison of quantitative results between the evaluation using MATLAB's *polyfit* function and the evaluation using the DOP fitting; Red dotted lines represent the hole depths, the black dotted line represents the plate thickness

(a) Phase image at f = 0.0980Hz

(b) Phase image at f = 0.196Hz

(c) Phase image at f = 0.294Hz

(d) Phase image at f = 0.392Hz

(e) Difference Accumulation

(f) Value Accumulation
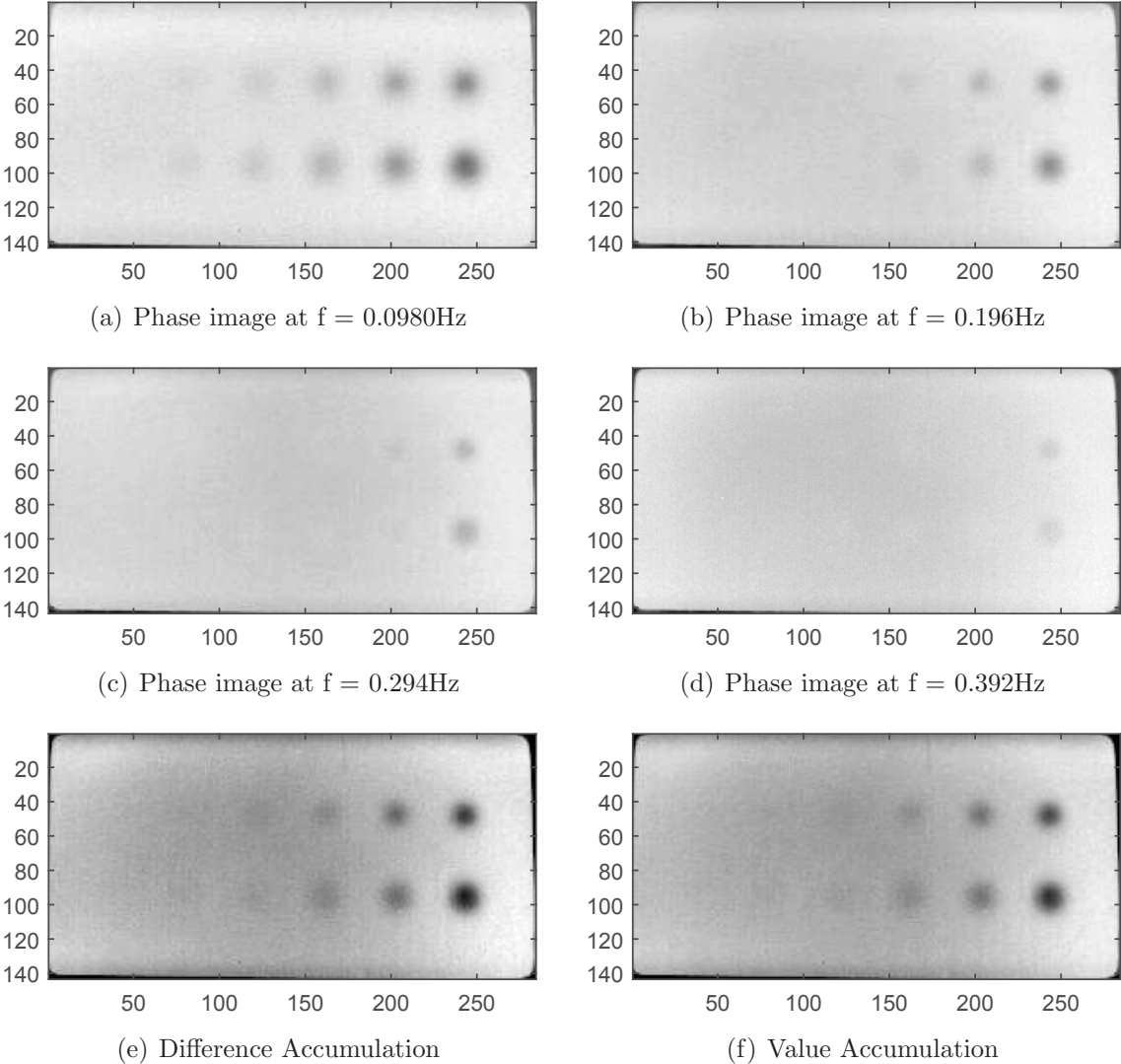
Figure 7.25: Results of the PPT evaluation
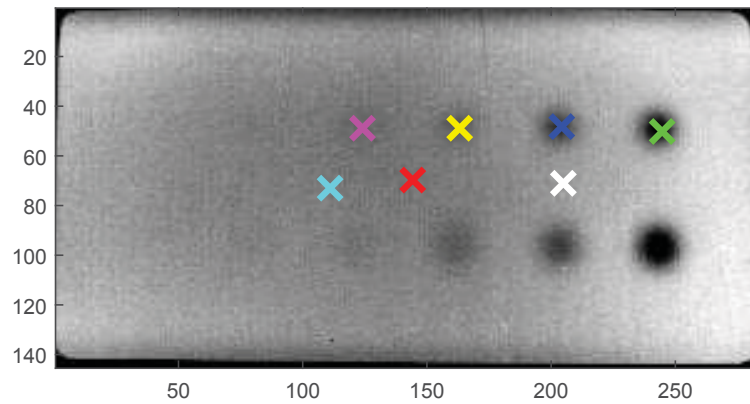
Figure 7.26: Result image of the Difference Accumulation, compared pixels are marked, re-
sults are summarized in table 7.3

Those investigations confirm the results from the phase and result images: The deeper
defects tend to disappear in evaluations at higher frequencies whereas the deepest defects are
not visible in any of the result images (quantified on the ratio). The defect four (magenta)
shows an aberration of more than 30% in the ratio to the flawless material in the difference
accumulation. Although this deviation is significant and would therefore be considered as
sign for a defect, its validity must be doubt, since the first reference (cyan) on flawless
material also deviates by about 20% compared to the first measurement mark (red). It is
questionable how much the ratio deflection of the fourth defect must be attributed to noise
rather than to the phase shift because of the defect.

In figure 7.26 we can see that the values increase towards the outer areas of the picture. A
possible explanation for this phenomenon is non-uniform heating of the specimen. The fact
that the increasing values form some kind of circular pattern on the specimen support this
suspicion. To investigate the influence of this phenomenon on the result, another reference
mark (reference 2, white) was set. The computed ratio for this reference mark (recorded in
table 7.3) indicates that the differences between the first measurement (red) and this second
reference is huge in the difference accumulation (due to the subtraction of the mean, as
described before), but since the values are more positive than compared to the first reference,
defects can still be detected (since they yield more negative values). Thus, information from
the phase images is still useful. Since we only seek a qualitative statement from the PPT
evaluations, this problem does not influence our results.

		1. Phase	2. Phase	3. Phase	4. Phase	Differ. Accum.	Value Accum.
Material/red	Phase	-0.4422	-0.7320	-0.9700	-1.1917	-0.0619	-3.3360
Defect 1	Phase	-0.5821	-0.8016	-0.9836	-1.1706	-0.2637	-3.5378
green	Ratio	1.3161	1.0951	1.0140	0.9822	4.2605	1.0605
Defect 2	Phase	-0.5371	-0.7628	-0.9684	-1.1679	-0.1621	-3.4362
blue	Ratio	1.2144	1.0420	0.9984	0.9800	2.6192	1.0300
Defect 3	Phase	-0.5002	-0.7368	-0.9629	-1.1772	-0.1029	-3.3770
yellow	Ratio	1.1311	1.0066	0.9926	0.9878	1.6630	1.0123
Defect 4	Phase	-0.4705	-0.7346	-0.9612	-1.1906	-0.0827	-3.3569
magenta	Ratio	1.0639	1.0035	0.9909	0.9990	1.3369	1.0062
Reference	Phase	-0.4388	-0.7310	-0.9626	-1.1909	-0.0492	-3.3234
1 cyan	Ratio	0.9922	0.9986	0.9924	0.9993	0.7957	0.9962
Reference	Phase	-0.4276	-0.7117	-0.9551	-1.1693	0.0103	-3.2638
2 white	Ratio	0.9669	0.9723	0.9846	0.9812	-0.1672	0.9783

Table 7.3: Comparison of different result images for all four defects of the specimen. Every defect is marked in figure 7.26 and the corresponding color is assigned in the first column of the table. "Phase" relates to the corresponding phase shift value of the specific defect in the specific result image (phase images one to four correspond to the images in figure 7.25 (a) to (d)). "Ratio" is the ratio of the phase shift value of the specific defect to the phase shift value of the flawless material in the corresponding result image.

7.3 3D printed Specimen

The Institute for Automation has multiple 3D printers available, therefore it was possible to produce plastic samples with defined artificial defects. The measurement and evaluation on one of these samples is presented in this section.

The specimen is a rectangular plate with three defects in different depths. For exact dimensions see figure 7.27.

A specimen of such dimensions but different material was used to describe the image processing steps in chapter 6. Note that in the measurement the sample was rotated by 180°. To simplify the nomenclature the defects are numbered from the lower left defect in figure 7.27 clockwise to the upper right defect.

7.3.1 Measurement in Transmission Mode

The specimen was measured in transmission mode and evaluated using both, Parker's method and the logarithmic method. The resulting α pictures are illustrated in figure 7.28. The averaged value over an area of flawless material is $\alpha = 1.26 \cdot 10^{-7} m^2/s$, which is in good agreement with [20], compare also table 2.2.
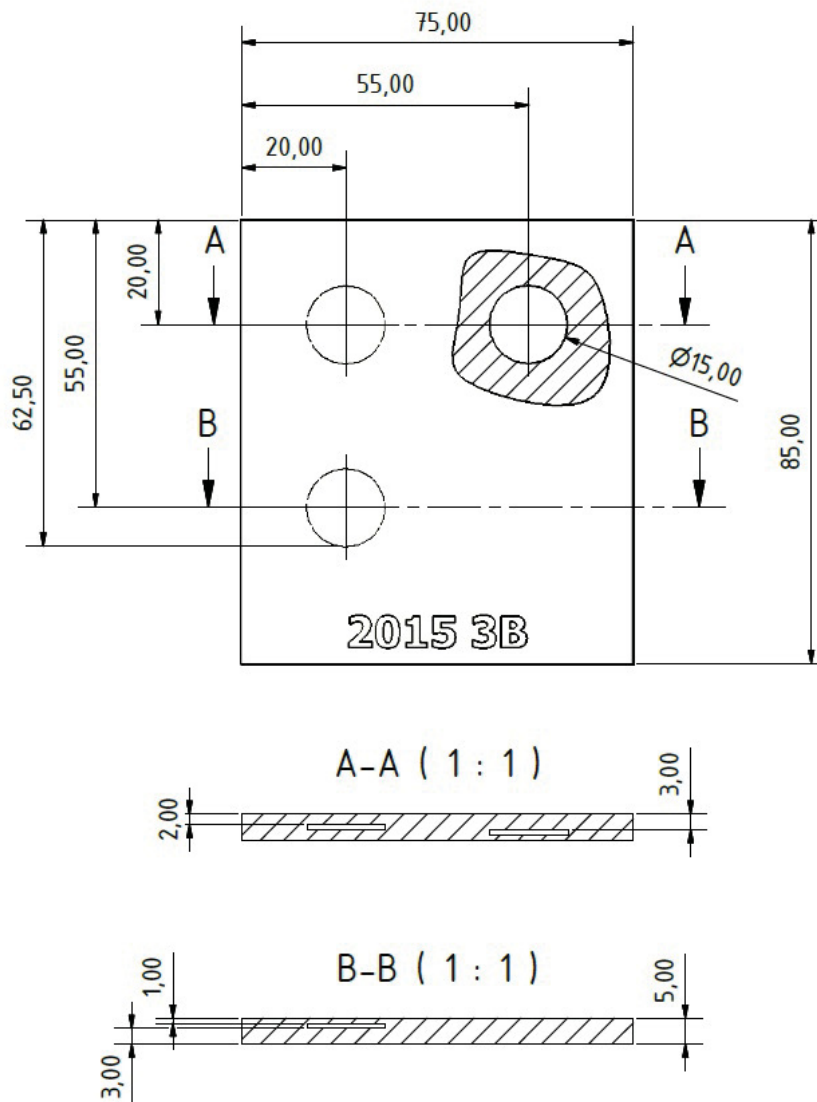
Figure 7.27: Sketch of the specimen including all dimensions and defects.

Both pictures in this figure show very good qualitative results, the defects are clearly distinct from the flawless material. However, the result of Parker's method seems to suffer slightly more noise (bright pixels spread across the picture), while the difference between defects and flawless material seems to be more distinct compared to the result of the logarithmic method. Note that the limits of the intensity level is set very tight compared to the results of the previous sections. Thus, the differences between the two methods must be relativized.

(a) Parker's method   (b) Logarithmic method
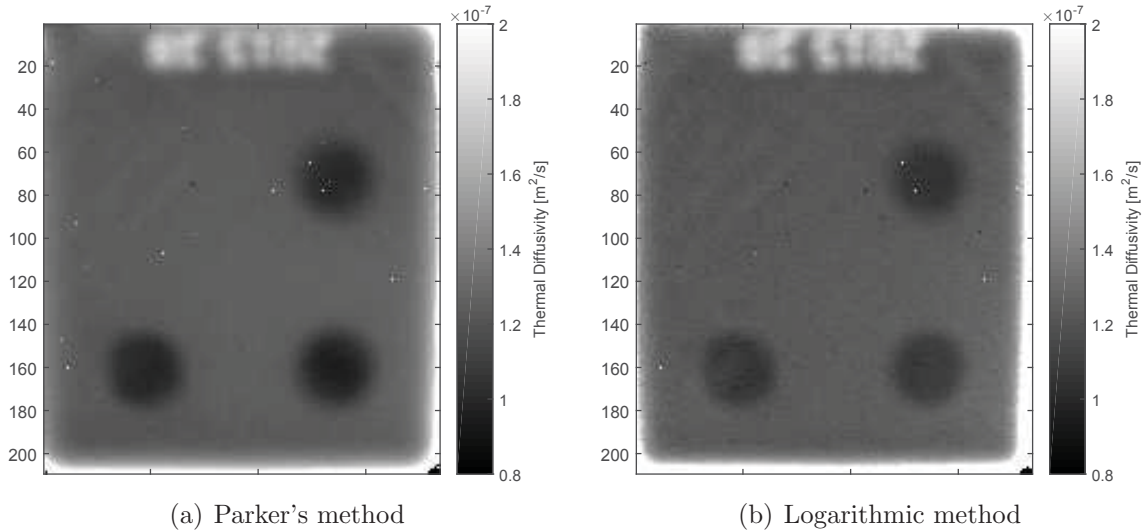
Figure 7.28: Resulting α pictures of the evaluations in transmission mode

7.3.2 Measurement in Reflection Mode - TSR

The results of the measurement in reflection mode using MATLAB's *polyfit* function yielded the thickness picture illustrated in figure 7.29.

This result shows that all defects are detectable very well. Note that the irregularities in the middle of the upper side of the specimen are caused by embedded letters and the ones on the right side by the support which holds the specimen in place. The deepest defect (defect no. one) is obviously not represented in its actual size, but considerations regarding the quantitative results are presented later in this section.

However, there is another irregularity which we would not expect in this result: the shallowest defect (defect no. three) is surrounded by a ring which seems to be of a very high thickness - even thicker than the base material. Furthermore, the thickness values along the inner side of this ring are zero, only the values in the middle of the defect show an actual thickness value. Those two problems have been investigated further. Therefore, two pixels have been extracted from the record to analyze the temperature profiles at those points. One of those pixels is one of the most inner pixels of the "thicker ring" (further called "high value pixel"), the other pixel on the inner side of this ring (further called "low value pixel"). The location of both pixels is marked in figure 7.29 with a cyan mark. The temperature profiles, the corresponding fitted polynomials and the second derivatives of the high and low value pixel are illustrated in figure 7.30.

This figure reveals two problems:

- There is no plateau observable in the temperature profile at the end of the record, as we would usually expect it. This phenomenon can be addressed to the heat loss due to heat radiation, which prevents the energy inserted into the specimen to form an equilibrium
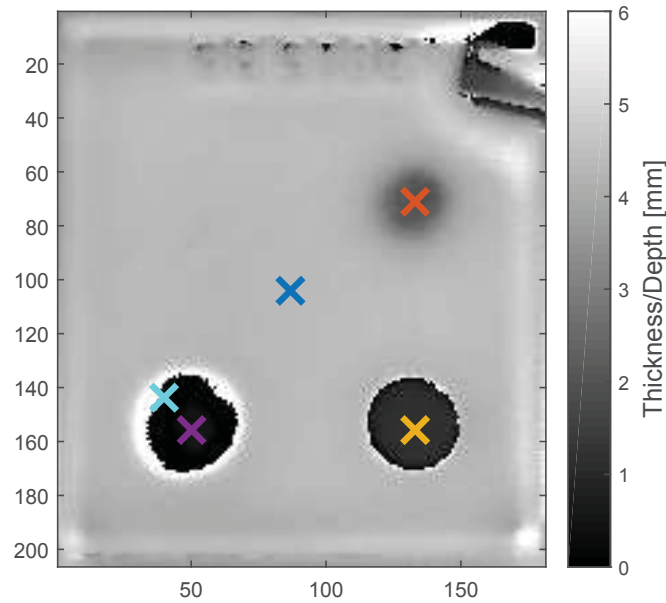
Figure 7.29: Thickness picture resulting from the evaluation using MATLAB's *polyfit*. The marks represent the extracted pixels for further investigations.

temperature after all heat flow processes are finished. The temperature of the surface will decrease further, until it reaches the same temperature as the environment. This problem is negligible in case of metal specimens because of their high thermal diffusivity and therefore short recording lengths. But in case of plastic, recording lengths are much longer and thus the effect of this influence is significant for such samples. This problem was previously pointed out by [6].

- The polynomial fit is insufficient at the start of the temperature profile. Not only the slope is much more negative than -0.5 but the curvature (second derivative respectively, figure 7.30(c)) does not start at zero but at a much higher value. Thus, there is no maximum in the second derivative at the location where the actual data turns positive. The differences between the fitted polynomials can be found at the very end of the temperature profiles: The polynomial of the high value pixel reaches a maximum right before the end of the profile while the polynomial of the low value pixel does not (Although the second derivative should be zero at the end of both profiles). Therefore, the t_w value of the high value pixel is determined too high while there is no maximum in the polynomial of the low value pixel (which is why the algorithm sets the value to zero).

To face the second problem, the measurement was also evaluated using the DOP evaluation. Furthermore, since the shape of the temperature profiles highly differ from the model
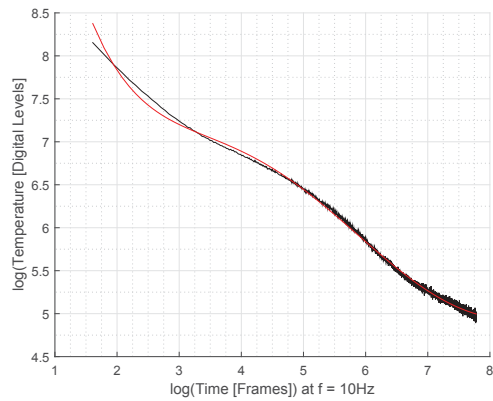
(a) Temperature profile and fitted polynomial of the high value pixel
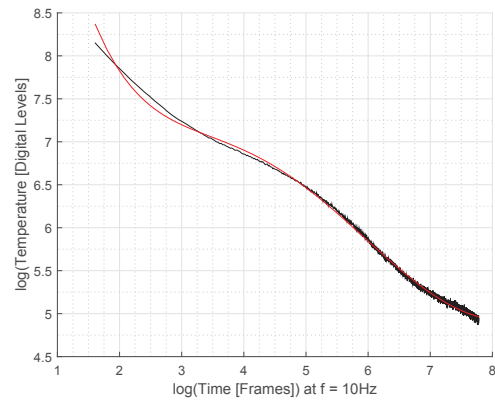
(b) Temperature profile and fitted polynomial of the low value pixel
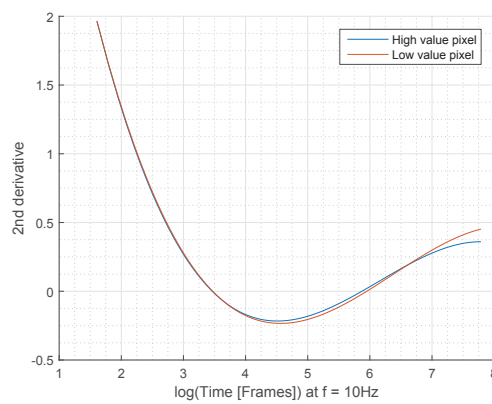
(c) Second derivatives of both pixels

Figure 7.30: Investigation of the irregularities at the edge of the shallowest defect (defect no. three), pixel position marked in cyan in figure 7.29

taken as basis, the constraints for the DOP fitting need to be modified. Therefore we consider figure 7.31.
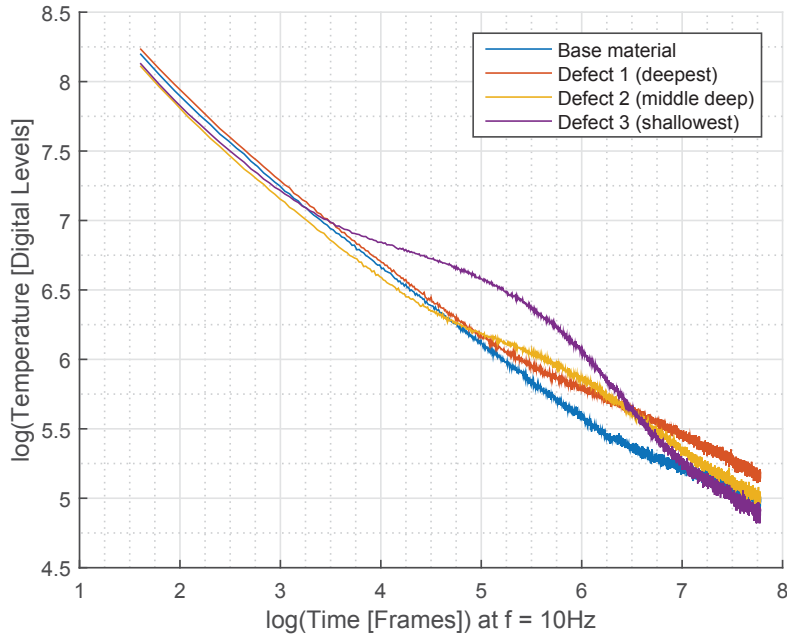
Figure 7.31: Temperature profiles of selected pixels over the three defects and the base material. Pixel position marked in the according color in figure 7.29.

All temperature profiles show a significant slope at the end (as mentioned before). Thus, the constraint which specifies the first derivative at the end of the profile is not set to zero, but to a value which is gathered by evaluation of the slope of the last $n_{LastPoints}$ data points. Furthermore, the slope at the start of the profile is specified as a fourth constraint, compare chapter 5.3.4. Contrary to the approach presented in this chapter, the slope of the $n_{FirstPoints}$ data points at the start of the profile is evaluated as well and set as the constraint in the first derivative. Note that the range of evaluations were $n_{FirstPoints} = 10$ and $n_{LastPoints} = 0.2 \cdot record\ length$. Furthermore, the determined slope was restricted by upper and lower limits which were $k_{BeginMin} = -0.9$ and $k_{BeginMax} = -0.1$ for the constraint at the start and $k_{EndMin} = -0.5$ and $k_{EndMax} = 0$ for the constraint at the end. Since we use four constraints for this example, we need to set $n_{FL} = 6$, compare chapter 5.3.4. Analogous, n_{DF} is set to $n_{DF} = 8$.

This approach yielded the results illustrated in figure 7.32.

First it is to note that both, the difference picture and the thickness picture show good qualitative results, all defects are determinable in both pictures. Note that the irregularity in the upper right part of the pictures is the support of the specimen. However, compared to the DOP approach presented in chapter 5.3.4 and the results of the previous examples, the difference picture in figure 7.32(a) shows unexpected results: Areas over defects do not

(a) Error picture   (b) Thickness picture
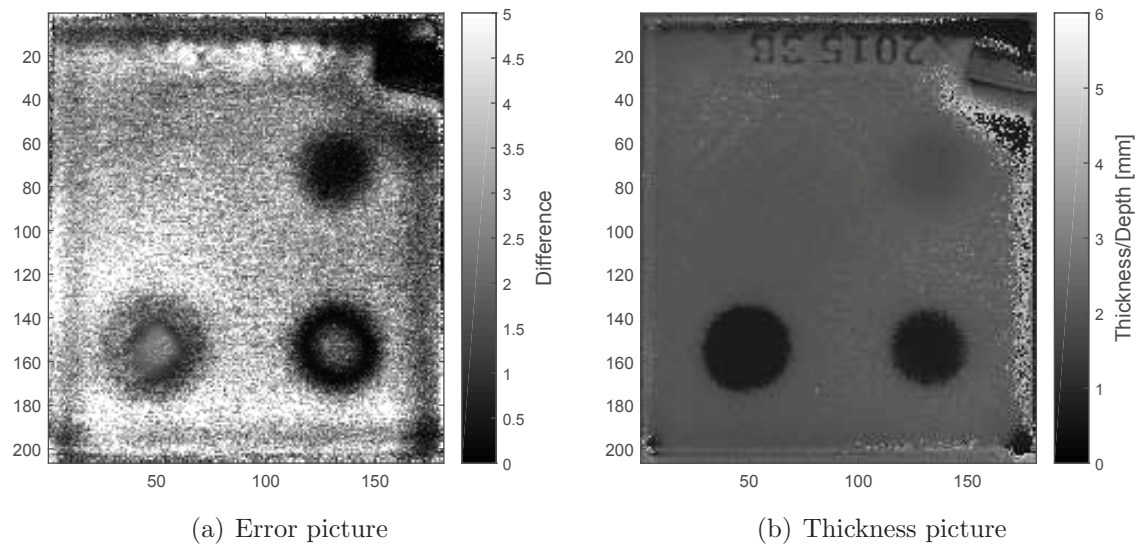
Figure 7.32: Results of the evaluation using DOP fitting

show higher, but lower error values. This means that the polynomial of degree six and seven approximate the temperature profile of defects more similar than profiles of flawless material. However, since the difference of defect pixels is almost always lower than the error of flawless pixels, the algorithm will almost always use the polynomial of degree six to determine t_w. This means that the result in figure 7.32(b) mainly consists of polynomials of degree $n_{poly} = 6$ (Note that the parameter n_{std} has almost no influence on this problem, since the error values of the defects are even lower than μ_{r^2}).

In such a case, where the actual recorded data differs from the model in such an extent, the algorithms to generate the results need to be reconsidered (although they do deliver good results). For example, since the DOP approach yields good results by only using a polynomial of degree six, we could only compute such a polynomial and use the first maximum in the second derivative as t_w. Considerations like this should be done to optimize the results for actual applications which deal with special materials or samples like in this case.

For further qualitative investigations, the values of the second derivatives at certain points in time are illustrated in the figures 7.33 and 7.34. Figure 7.33 shows the second derivatives of the polynomials generated by the *polyfit* approach, as well as of the polynomials, which have been selected due to the difference limit (compare section 5.3.4), generated by the DOP approach. Since we are looking for defects, we also compute the second derivative pictures of the DOP polynomials of higher degree exclusively, since those polynomials are supposed to represent a defect (compare section 5.3.4). Those pictures are illustrated in figure 7.34. Both figures illustrate, that all defects can be detected very well within a picture of second derivatives at certain points in time. Again, in case of the DOP approach, the evaluation of the polynomial of higher degree yields better results.

(a) *polyfit*: 5.4598s   (b) DOP: 5.4598s   (c) *polyfit*: 10.9947s

(d) DOP: 10.9947s   (e) *polyfit*: 24.4692s   (f) DOP: 24.4692s

(g) *polyfit*: 60.1845 s   (h) DOP: 60.1845 s
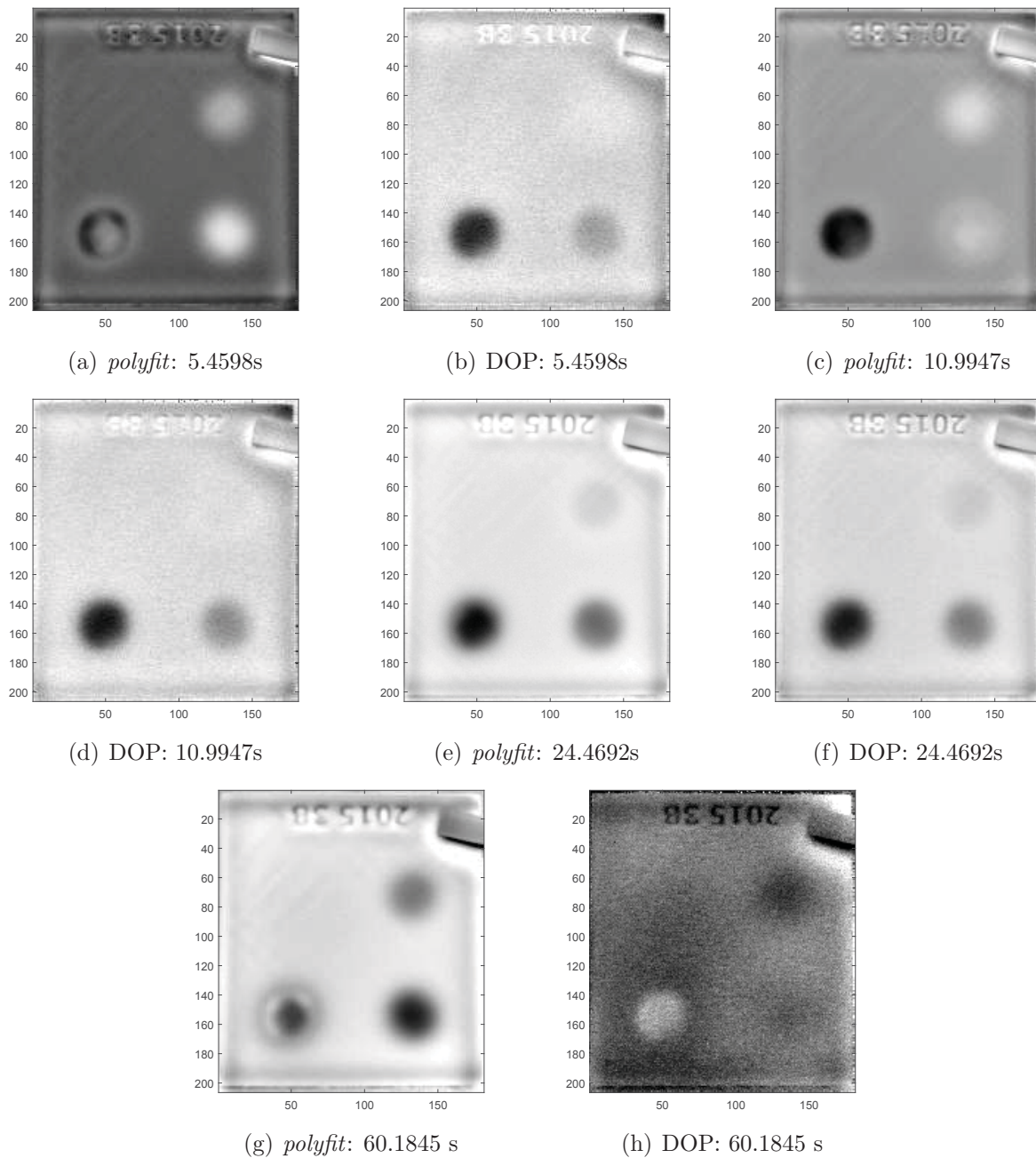
Figure 7.33: Second derivatives at certain points in time for *polyfit* and DOP polynomials

(a) 5.4598s

(b) 10.9947s

(c) 24.4692s

(d) 60.1845s
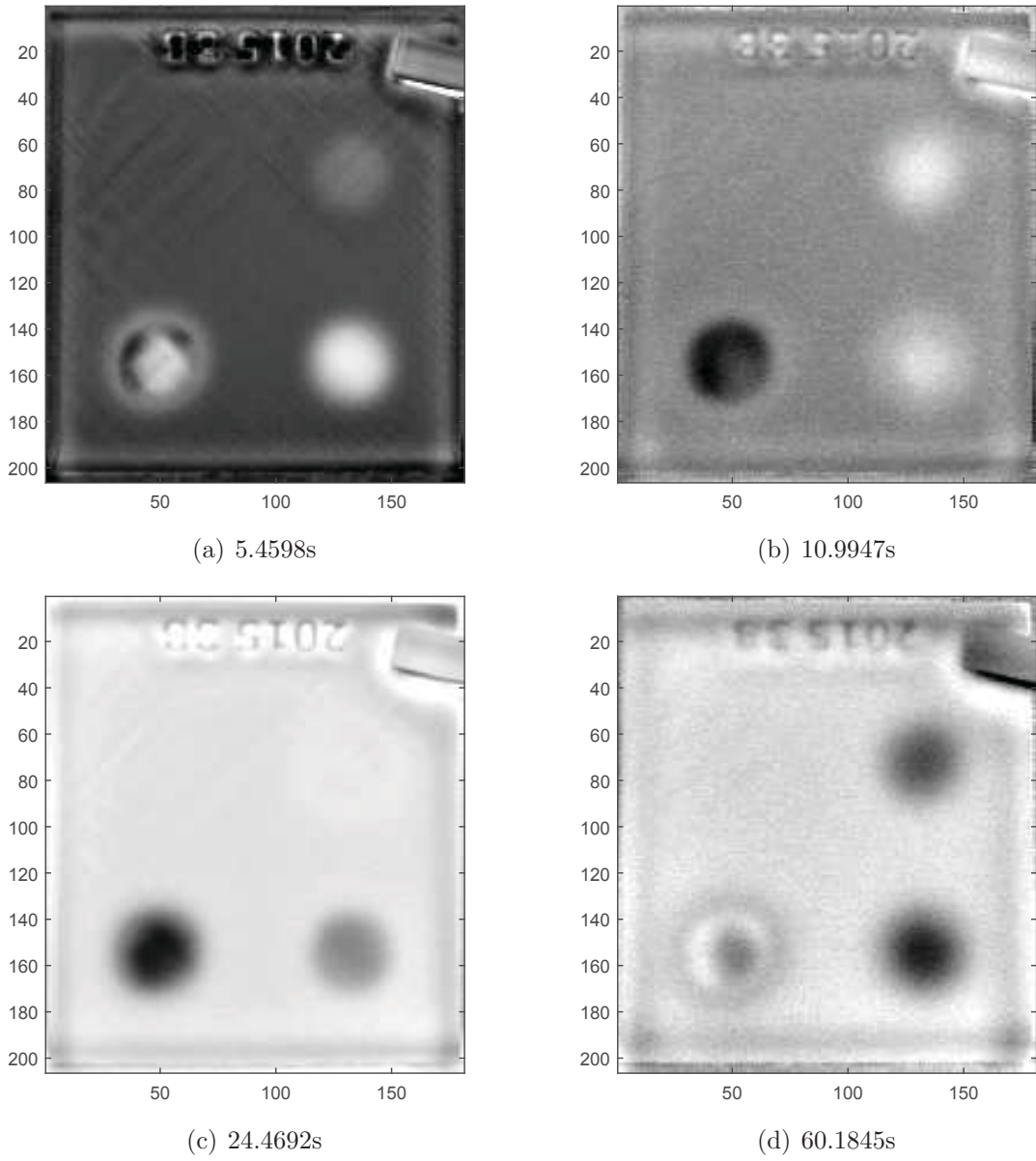
Figure 7.34: Second derivatives at certain points in time for DOP polynomials used for the representation of defects

If we consider the thickness/depth picture in figure 7.32(b), we can observe that the thickness of the specimen is determined much too small (around 2-2.1mm instead of 5mm). The reason for this can be found in figure 7.35. This figure shows the temperature profile of the pixel marked in blue in figure 7.29 together with the fitted polynomials of the *polyfit* approach, as well as both polynomials of the DOP approach. Figure 7.35(a) indicates an insufficient fit of the polynomial of degree $n = 6$. This is the polynomial which is used for flawless material representation. This insufficient fit yields a deviation of the maximum in the second derivative, compare with the polynomial of the *polyfit* approach in figure 7.35(c). A polynomial of higher degree, such as the polynomial of degree $n = 8$ in figure 7.35 represents t_w much more precisely (maximum in the second derivative correlates with the maximum of the *polyfit* polynomial), but yields a second (earlier) maximum in the second derivative, which would be mistaken by the software as a defect. This phenomenon also appears for polynomials of degree $n = 7$. Thus, the DOP approach is not suited for quantitative investigations of such materials without modifications.

(a) Temperature profile and fitted polynomials

(b) 1st derivatives
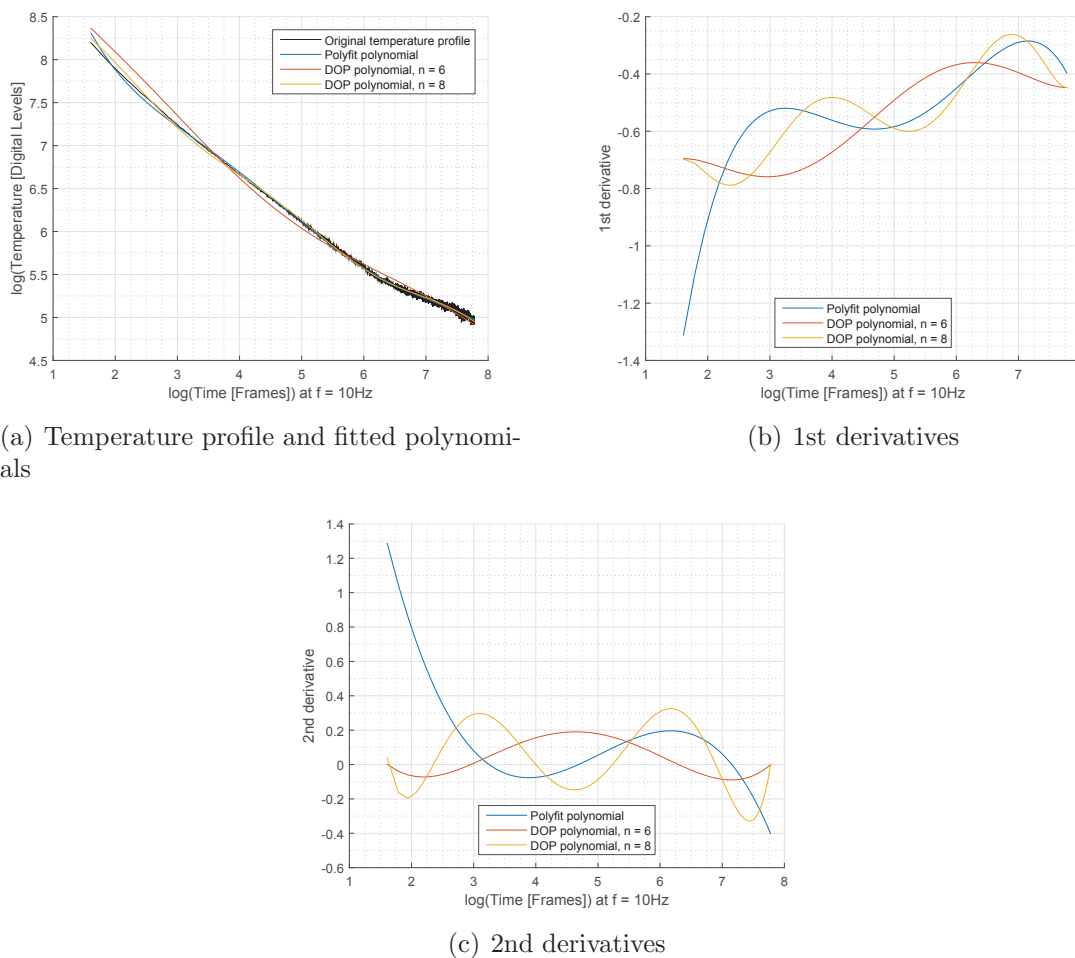
(c) 2nd derivatives

Figure 7.35: Different polynomial fittings and their derivatives to a temperature profile of the base material, used pixel marked in blue in figure 7.29

Defect no.	Diameter [mm]			Thickness/Depth [mm]		
	Specimen	polyfit	DOP	Specimen	polyfit	DOP
Base Material	-	-	-	5	4.3	2.1
1	15	10.2	12.7	3	2.0	1.8
2	15	14	14.8	2	1.2	0.7
3	15	15.7	17	1	0.5	0.7

Table 7.4: Summary and comparison of the results between MATLAB's *polyfit* and the DOP approach

To investigate and compare the results with regard to quantitative properties further, the diameter and depth of the defects in the thickness/depth picture of MATLAB's *polyfit* function as well as of the DOP approach have been determined and are summarized in table 7.4.

This table shows, that the quantitative results do not represent the defects correctly. The dimension (diameter) of the defects is underestimated in case of deep defects and overestimated in case of shallow defects. Furthermore, when estimating the depth of a defect, we can only use the pixels in the middle region of the defect (due to the problems in the vicinity of the defect borders described above). Due to the problems of the polynomial fitting in case of the DOP method mentioned above, the depth values of this approach can not be used for a quantitative evaluation. Although the results of the *polyfit* method can not be taken for granted, they provide a good estimation of the actual defect.

7.3.3 Measurement in Reflection Mode - PPT

The phase and accumulation result images of this measurement have already been used in chapter 5.4 to illustrate the evaluation process of the PPT (see figure 5.12 and figure 5.13). Therefore, they will not be presented here again.

To look at those results more closely they are investigated in the same way as described in section 7.1.3. Figure 7.36 and table 7.5 present the results of this investigation.

The values in the table yield the following conclusions:

Defects in different depths show different visibility (as mentioned in chapter 5.4). The Value Accumulation and especially the Difference Accumulation are able to merge the defects, which are visible in different phase images, together to one result image where all defects can be detected. The first two phase images, but even more the Difference Accumulation image, show high contrast between a defect and the flawless material.

However, the Difference Accumulation must be considered with caution. As the ratios of the two reference marks on flawless material indicate, those ratios are subject to high noise. This phenomenon can be addressed to a division by a number close to zero (compare section
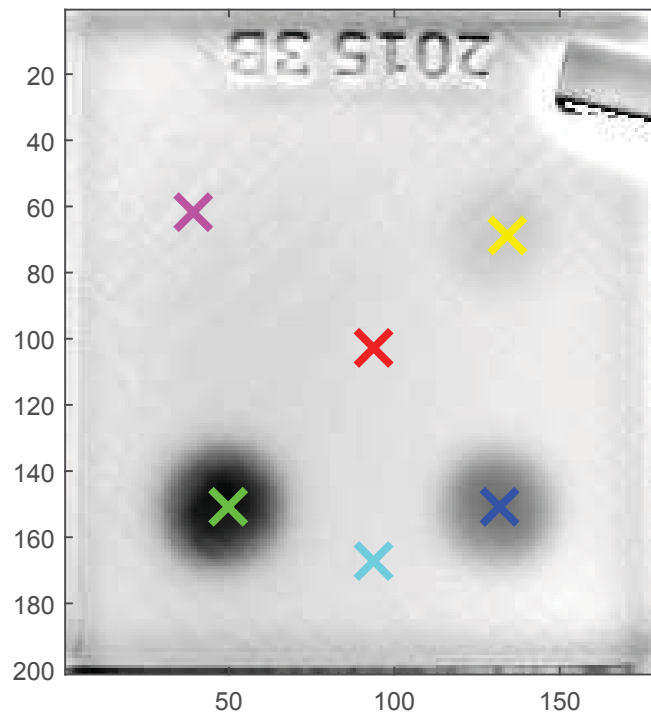
Figure 7.36: Result image of the Difference Accumulation, compared pixels are marked, results are summarized in table 7.5

5.4 and 7.1.3). Still, the ratios of the defects are significantly higher (in terms of absolute values), which allows us to use this ratio to identify defects.

7.4 Glued Steel Plates

A specimen was tested that was produced and already used by [1] (but with a different testing method) and is illustrated in figure 7.37. This specimen consists of two 300×170mm steel plates with a thickness of 0.75mm, which have been glued together. To do so, the glue was just partially deposited on the steel plates in the shape of four circles with different diameters ([1]). Additionally, to increase emissivity, one side of the specimen was painted black. The other side was left blank because of the usage in other experiments and could therefore not be painted. The idea of this specimen is to simulate a bonded joint with air pockets. No quantitative results are of interest, the goal is only to be able to separate areas of a correct bond and air pockets (which are basically contact points between the two steel plates around the bonds).

		1. Phase	2. Phase	3. Phase	4. Phase	Differ. Accum.	Value Accum.
Material/red	Phase	-0.5157	-0.6342	-0.7164	-0.7703	0.0051	-2.6366
Defect 1	Phase	-0.7141	-0.9726	-1.0753	-1.1044	-1.2246	-3.8664
green	Ratio	1.3847	1.5336	1.5009	1.4338	-238.3019	1.4664
Defect 2	Phase	-0.7434	-0.8499	-0.8472	-0.8374	-0.6362	-3.2779
blue	Ratio	1.4416	1.3401	1.1826	1.0870	-123.7945	1.2432
Defect 3	Phase	-0.6482	-0.6730	-0.6989	-0.7366	-0.1150	-2.7568
yellow	Ratio	1.2570	1.0613	0.9756	0.9563	-22.3868	1.0456
Reference	Phase	-0.5144	-0.6286	-0.7139	-0.7740	0.0108	-2.6309
1 magenta	Ratio	0.9975	0.9912	0.9966	1.0047	2.1003	0.9979
Reference	Phase	-0.5024	-0.6297	-0.7168	-0.7694	0.0235	-2.6182
2 cyan	Ratio	0.9743	0.9929	1.0006	0.9988	4.5665	0.9930

Table 7.5: Comparison of different result images for all four defects of the specimen. Every defect is marked in figure 7.36 and the corresponding color is assigned in the first column of the table. "Phase" relates to the corresponding phase shift value of the specific defect in the specific result image (phase images one to four correspond to the images in figure 5.12 (a) to (d)). "Ratio" is the ratio of the phase shift value of the specific defect to the phase shift value of the flawless material in the corresponding result image.

7.4.1 Measurement in Transmission Mode

The measurement in transmission mode was carried out with the black painted surface facing the IR-camera. The evaluation was done using the logarithmic method described in chapter 4.2.2. The result is the α picture in figure 7.38.

The picture shows very good results. All four bond joints can be detected. They are furthermore very well distinguished from the glue free areas.

It is to note that the values of the thermal diffusivity, which are given in the color bar of the result image, are not representative and can not be taken as correct. This is due to the fact that we do not deal with a homogeneous specimen. The overall thermal diffusivity is composed of

1. the thermal diffusivity of the steel plates and the thermal contact resistance between those two plates and

2. the thermal diffusivity of the steel plates, the thermal contact resistance from the transition steel/glue and glue/steel and finally the thermal diffusivity of the glue.

The resulting values are therefore a combination of those components and can only be used for qualitative statements - as desired.

(a) Top view

(b) Section view
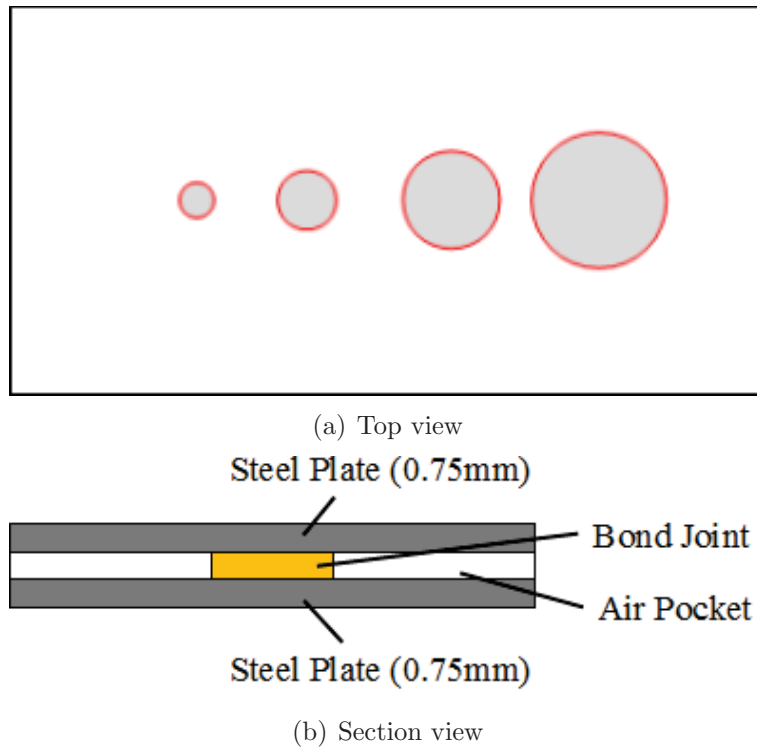
Figure 7.37: Illustrations of the glued steel plates

7.4.2 Measurement in Reflection Mode - TSR

The measurement in reflection mode was carried out with the black painted surface facing camera and flash lamp.

First, the t_w picture was generated using MATLAB's *polyfit* function. The result is illustrated in figure 7.39.

This figure shows that all four bond joints differ significantly from the rest of the plate surface. Thus, since the bond joints can be detected, air pockets in such joints can be found as well. However, figure 7.39 shows irregularities. Therefore, four pixels have been selected and marked in the figure for further investigations. Figure 7.40 illustrates the temperature profiles of those four pixels in the corresponding color.

The temperature profiles of this figure are of a complete different shape than we would expect. The temperature over the bond joints drops faster than over areas, where the plates are separated from each other. This makes sense, because we can expect the thermal diffusivity through the glue to be higher than through the separated plates, which represent a high thermal contact resistance. There is an obvious anomaly in the area around the smallest bond joint. The temperature in this area (violet mark in figure 7.39) seems to drop faster than in other areas without bond joints (compare figure 7.40). The reason for this is an adhesive label on the rear side of the specimen at this location. As mentioned, the rear side of the specimen is not painted. The label shows very high emissivity values compared to the
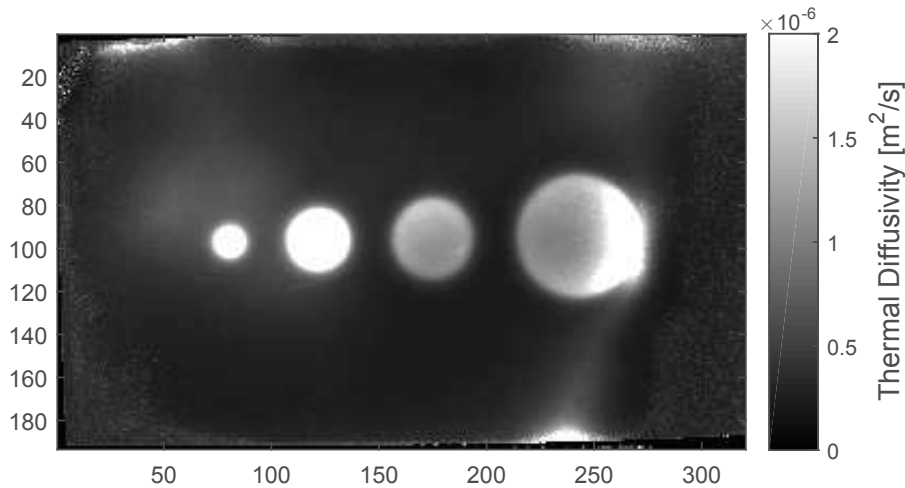
Figure 7.38: Resulting α picture in transmission mode using the logarithmic method

blank metal surface (compare table 2.4). Thus, the label (which is used in other experiments and should therefore not be removed) distorts the heat flow and yields the corresponding temperature profile. This phenomenon can also be observed in the transmission measurement (figure 7.38, only very weak distortion around the smallest bond joint) and in the following PPT evaluations.

Figure 7.41 illustrates the results using the DOP evaluations. This evaluation also allows to distinguish between bond joints and air pockets qualitatively. Note that the used conditions are the same as in case of the 3D printed specimen presented in section 7.3.2 (measuring the slope of the temperature profile at the begin and the end, using four boundary conditions, using polynomials of degree $n_{FL} = 6$ and $n_{DF} = 8$).

However, since this example differs from the model in a large extent, both evaluation methods have problems to derive meaningful information from the data. To receive better results for such an application, we need to define the properties we want to focus on in the evaluation. Since there is basically no base material as there is in the model and in all other examples, we could instead evaluate all first or second maximum in the second derivative of the temperature profiles. After the model is adapted to such new conditions, the algorithms can be modified and optimized to fit the new model.

Analogue to previous examples, the values of the second derivatives at certain points in time are illustrated in the figures 7.42 and 7.43 for further qualitative investigations. Figure 7.42 shows the second derivatives of the polynomials generated by the *polyfit* approach, as well as of the polynomials, which have been selected due to the difference limit (compare section 5.3.4), generated by the DOP approach. Since we are looking for irregularities, we also compute the second derivative pictures of the DOP polynomials of higher degree
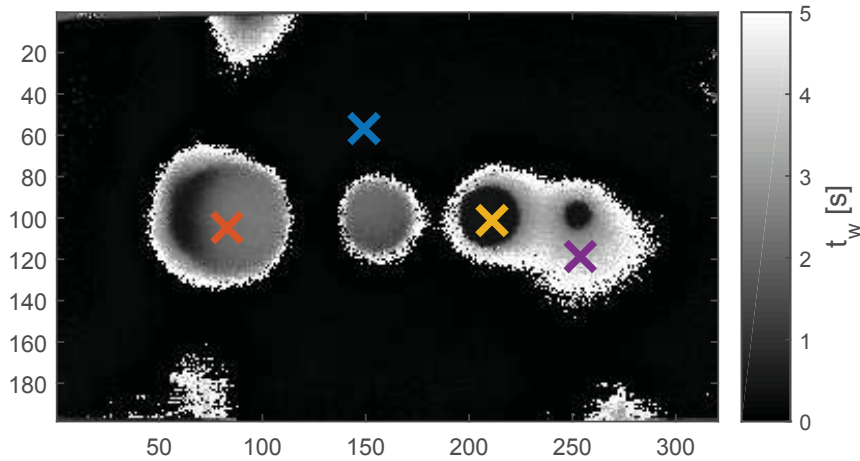
Figure 7.39: Resulting t_w picture using MATLAB's *polyfit* function. The marks represent the selected pixels for further investigations

exclusively, since those polynomials are supposed to represent a defect or irregularities, respectively (compare section 5.3.4). Those pictures are illustrated in figure 7.43. Both figures illustrate, that all bond joints or air pockets can be detected very well within a picture of second derivatives at certain points in time. In this case, the results of the selected DOP polynomials (figure 7.42) are very similar to the results of the polynomials of higher degree (figure 7.43).

Finally, figure 7.40 illustrates the discrepancy between record frequency and record length. If we want to evaluate the first maximum in the second derivative (or represent this maximum with a polynomial, respectively), we need a high frequency to reproduce the temperature profile at the start in a high resolution. If we want to evaluate the second or last maximum in the second derivative (or represent this maximum with a polynomial, respectively), we need a long recording duration (one can see in figure 7.40 that the end plateau of the blue temperature profile is not on the record any more). Since the software of the used experimental rig is limited by the size of the recorded data file, we always have to do a trade off between record frequency and length.

7.4.3 Measurement in Reflection Mode - PPT

The measurement from section 7.4.2 was evaluated using the PPT method. Because of the chosen measurement parameters (short recording time, high recording frequency because of the high thermal diffusivity of the steel) the available frequency increments for the phase shift evaluation are more numerous (compare equation (4.22)) than for similar measurements using plastic or CFRP specimens. Thus, the phase shift changes much faster with the frequency
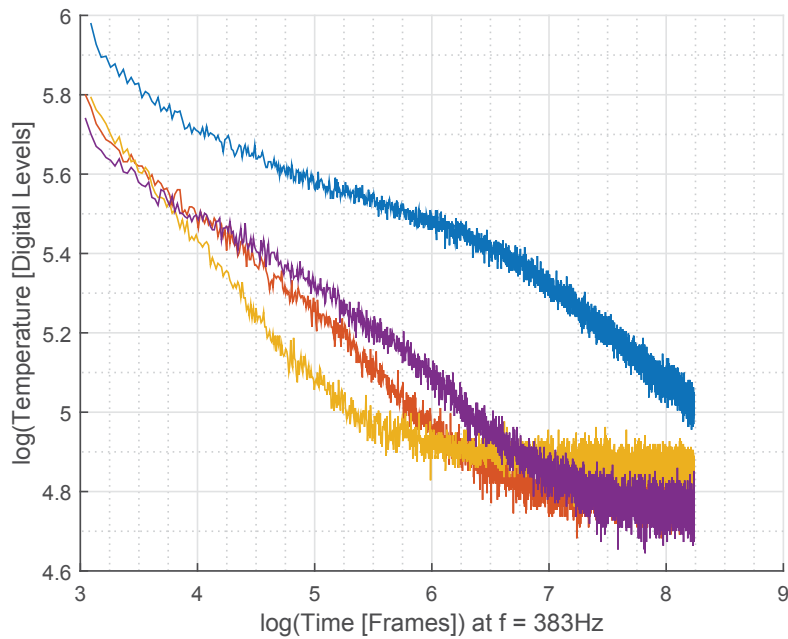
Figure 7.40: Temperature profiles of the four selected pixels from figure 7.39 in the corresponding color

increment. Therefore, only the first phase evaluated at a frequency of 0.191Hz was used to present the result (phase images at higher frequencies yield changes in the sign of the phase as seen in figure 7.12(d), accumulation images are therefore not computable as well). This phase image is illustrated in figure 7.44.

This figure shows that all four bond joints are visible very well. Compared to the result from the TSR technique, illustrated in the figures 7.39 and 7.41, the result is in fact excellent. The PPT technique is - in cases of insufficient recording time - obviously much more stable than the TSR technique. For qualitative measurements, this is a big advantage. Furthermore, the PPT evaluation does not require a t_{EoF} determination, which eliminates

(a) Difference picture

(b) t_w picture
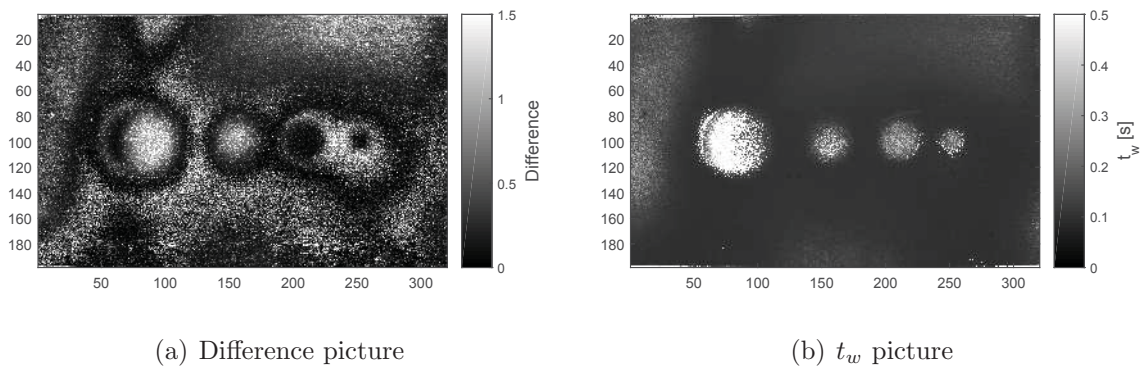
Figure 7.41: Results of the evaluation using DOP fitting

(a) *polyfit*: 0.2350s

(b) DOP: 0.2350s

(c) *polyfit*: 0.5781s

(d) DOP: 0.5781s

(e) *polyfit*: 1.2866s

(f) DOP: 1.2866s

(g) *polyfit*: 3.8650 s

(h) DOP: 3.8650 s
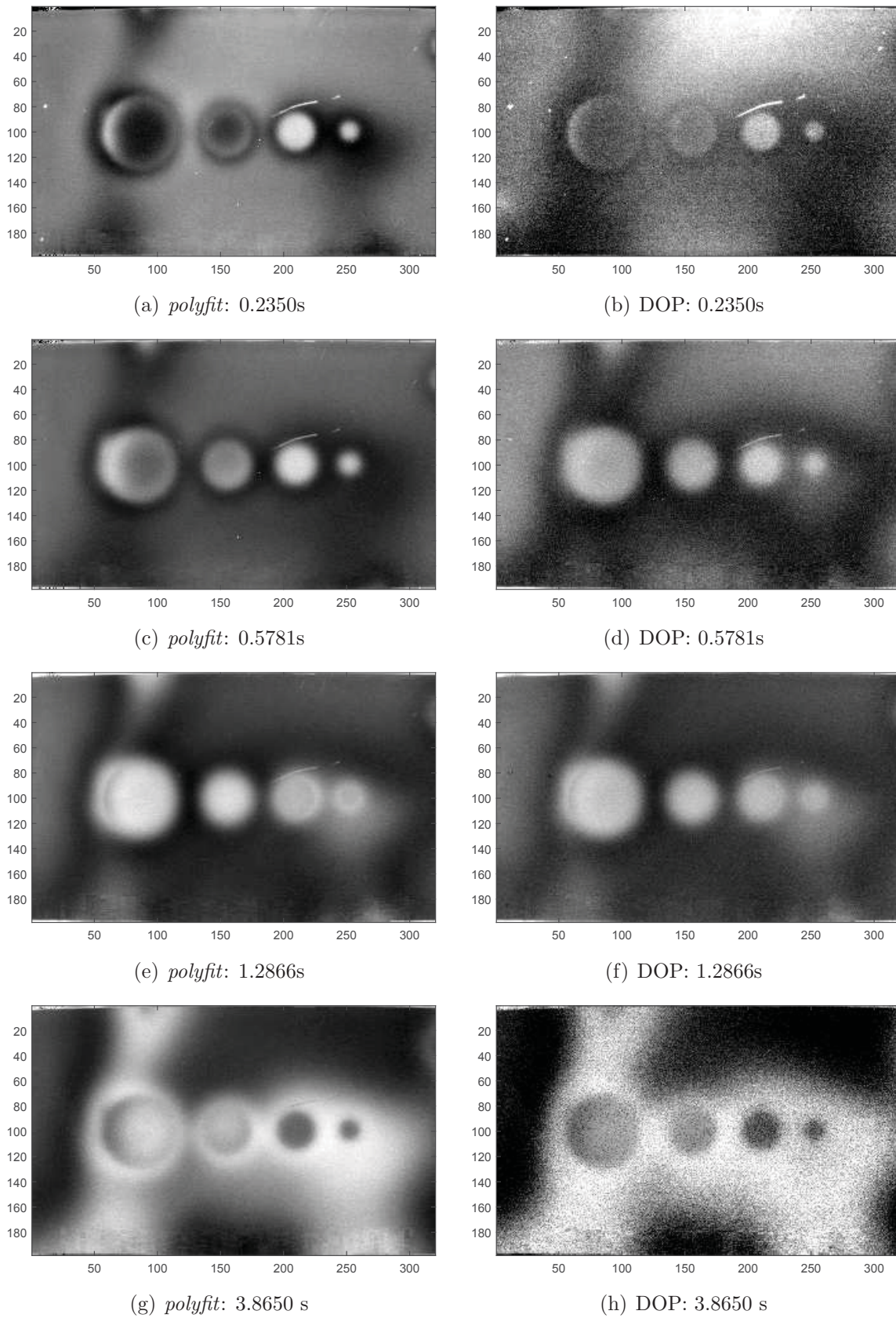
Figure 7.42: Second derivatives at certain points in time for *polyfit* and DOP polynomials

(a) 0.2350s

(b) 0.5781s

(c) 1.2866s

(d) 3.8650s
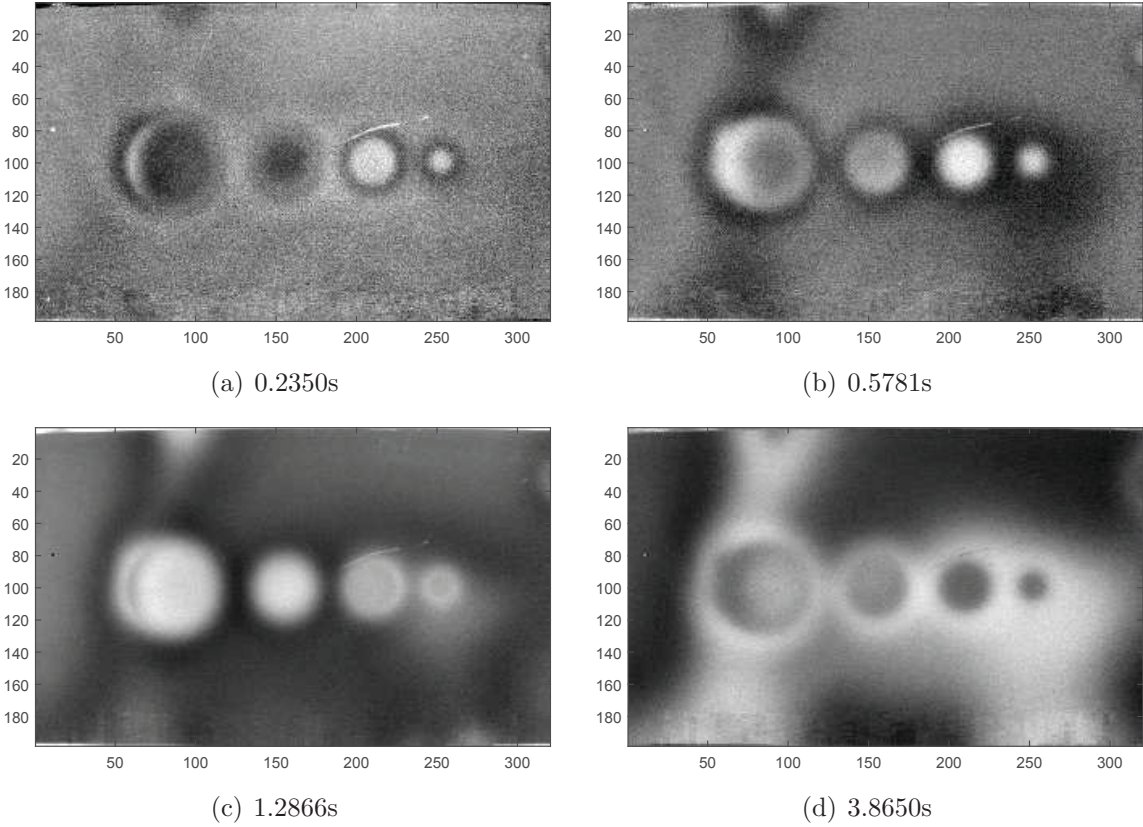
Figure 7.43: Second derivatives at certain points in time for DOP polynomials used for the representation of defects
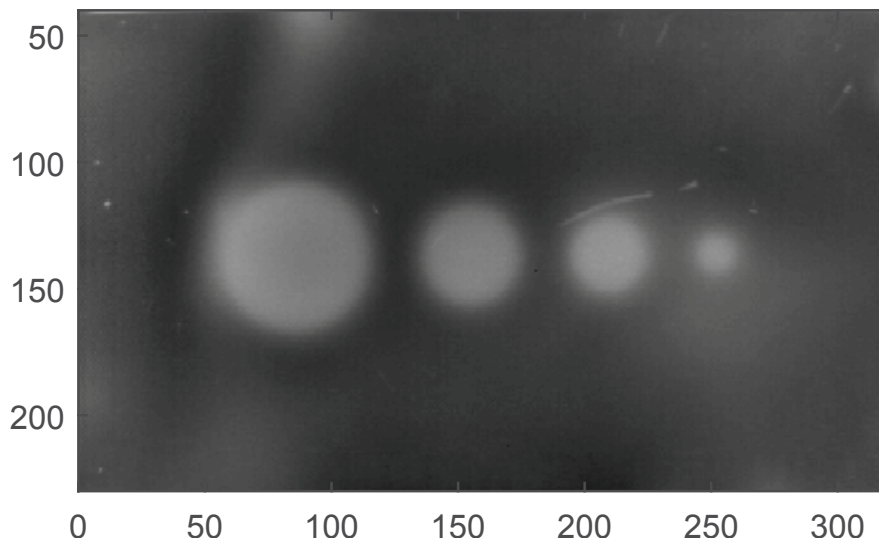
Figure 7.44: Phase image evaluated at a frequency of f = 0.191Hz

some problems regarding the flash influence described in the previous sections on the one hand and saves computational time on the other hand.

7.4.4 Comparison Transmission/Reflection

Comparing the evaluation results of the presented methods shows that all of them are suited to detect bond joints and air pockets, respectively. However, problems arise when executing TSR evaluations for such a specimen. As mentioned, this evaluation type is adversely affected by the necessary trade off between record frequency and duration, which does not influence transmission or PPT evaluations in such an extent.

7.5 Porosity Measurements

The Institute for Processing of Composites at the Montanuniversität Leoben is interested in measuring porosity in CFRP materials. Experiments have been performed to investigate the ability of thermographic measurements to determine the porosity of such specimens.

Therefore, the Institute produced two rectangular CFRP plates with a size of 315×320mm. One plate was produced in vacuum to reduce the porosity to zero. In the second plate, air was inserted to produce porosity on purpose. This led to different plate thickness of 1.3mm for the plate with no porosity and 4.5mm for the plate with porosity. Unfortunately, the used procedure does not allow to produce plates with a well-defined porosity. No statements about the exact specificity of the porosity can be made.

As experiments from the previous sections showed, the polynomial fitting of the TSR evaluations is unstable and in certain limit cases the received t_w value does not adequately

represent the inflection point which we seek (compare figure 4.7). Furthermore, due to the material properties of the CFRP specimen, we need very long recording durations. Thus, unfavorable effects of heat losses during the recording affect the results significantly (compare also section 7.3.2 and figure 7.31, as well as [6]). Since we are interested in an exact numerical (and absolute) value as a result we only use transmission mode for the following measurements (PPT evaluations are only for qualitative investigations anyway). Thus, both specimen have been measured in transmission mode.

The logarithmic method (chapter 4.2.2) was used to compute the thermal diffusivity α for every pixel of the specimen surface. Afterwards, the mean of all surface pixels was calculated.

This procedure yielded two different values for the thermal diffusivity of the two plates which are

$$\alpha_{non-porose} = 4.83 \cdot 10^{-7} m^2/s$$
$$\alpha_{porose} = 2.83 \cdot 10^{-7} m^2/s$$

for the non-porose plate and the porose plate, respectively.

Those results show that the porosity of a CFRP sample has influence on its thermal diffusivity. Those influences are measurable using a thermographic measurement in transmission mode. The results are in good agreement with [9, 33], but are higher than in [10]. It is again to note, that CFRP specimen are very homogeneous and their thermal properties highly depend on their internal structure. Direct comparison is therefore difficult.

7.6 Detecting Material Inhomogeneity

A number of steel plates have been welded together (always two plates) using butt welds. Therefore, rectangular plates with a weld somewhere in the middle of the plate could be investigated. To increase emissivity, both sides of the plates have been painted black. The microstructure of the welds are different from the microstructure of the plate. This results in a different thermal diffusivity. Using a thermographic measurement in transmission mode, those different thermal diffusivities can be determined and therefore the microstructure of the weld investigated. Figure 7.45 illustrates the thermal diffusivity of a welded steel plate, computed using the logarithmic method. Figure 7.45(a) represents the α values across the entire steel plate, including the weld. The figure shows very clearly, that the weld has a different thermal diffusivity than the plate. For better evaluation, pixels along a line over the weld as well as an area of pixels on the plate have been selected for further investigations. The extracted pixels are marked in figure 7.45(a). The values of those pixels are presented

in two histograms (for the weld and the plate separately) in figure 7.45(b). The mean values of the thermal diffusivity of the selected pixels are

$$\alpha_{plate} = 3.58 \cdot 10^{-6} m^2/s \tag{7.2a}$$

$$\alpha_{weld} = 3.41 \cdot 10^{-6} m^2/s \tag{7.2b}$$

which proves that a difference in thermal diffusivity of only 5% can be detected very well, using the presented technique.

Those results demonstrate that thermography is able to detect differences in the microstructure of steel (and other materials as long as those different microstructures have different thermal diffusivities). Therefore, those methods could, for example, be used for material testing after heat treatments.
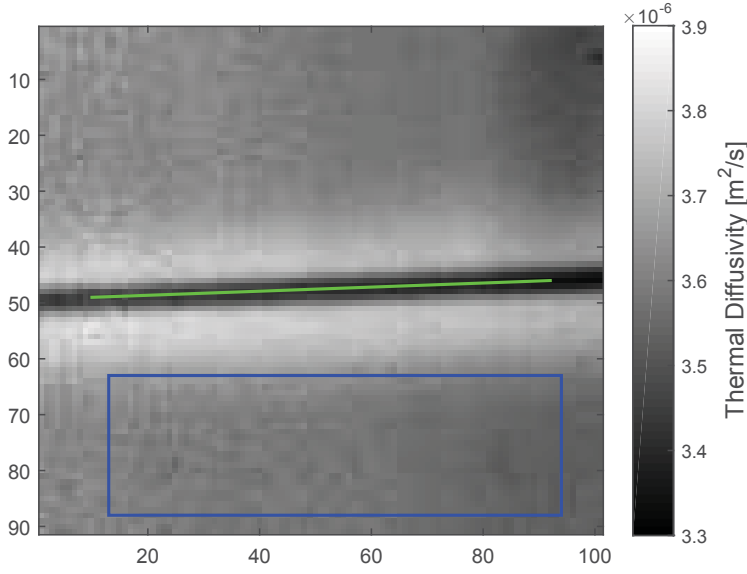
(a) α values across the steel plate, pixels for further investigations marked
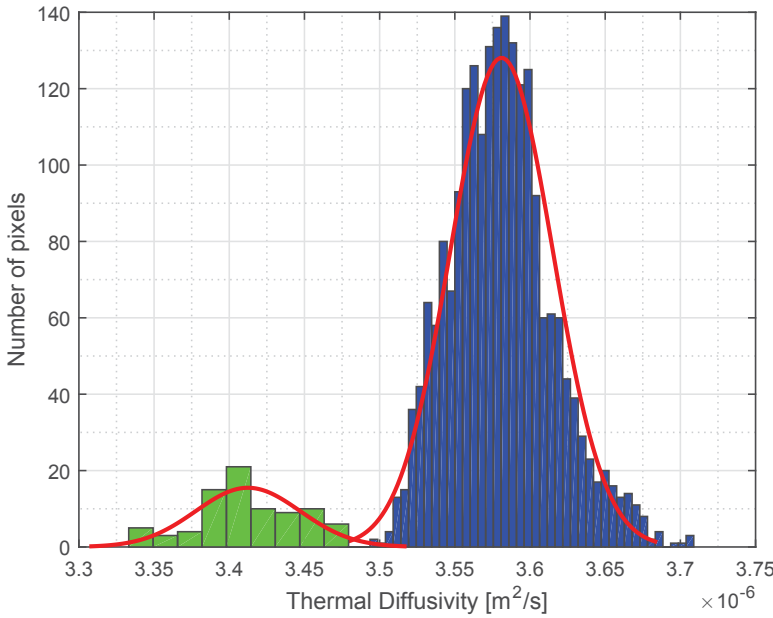
(b) Illustration of pixel values as histograms, colors according to marked pixels in (a)

Figure 7.45: Welded steel plate with different thermal diffusivities in weld and plate.

8 Discussion

8.1 Conclusion

The built experimental rig and the corresponding developed software proved to be capable of performing flash thermographic tests. The results gained with this setup seem promising for the most part.

Especially in transmission mode, the accuracy of the received information about the thickness of specimen is acceptable. The TSR technique provides mostly feasible quantitative (and therefore also qualitative) results for thickness/depth and thermal diffusivity values. The developed DOP fitting in reflection mode promises good results if it is optimized for certain applications. Although the PPT does not provide information about the depth of defects (at least as it concerns this thesis), the qualitative results are very suitable, especially when using the accumulation techniques. For deeper defects, the PPT yields slightly better results compared to the TSR in reflection mode.

Beside the depth detection, anomalies can be detected through the dependence of the thermal diffusivity on such inhomogeneities. This fact can be used to determine the porosity of CFRP elements (if further enhanced) or differences in material composition, such as differences in the microstructure, even if the impact on the thermal diffusivity is very small. Furthermore, air pockets in bonded joints can be detected.

This yields the following fields of application for transmission and reflection measurements:

- **Transmission:** A specimen must be accessible from both sides. The depth of defects is not determinable, thus this depth must not be relevant. The accuracy of determined properties is high.

- **Reflection:** Only one side of a specimen must be accessible. This provides the possibility of material tests on inbuilt specimen. Furthermore, the depth of defects is determinable to a certain extent. The accuracy of the results is not as high as for measurements in transmission mode.

The developed manual evaluations, inspection methods and assistant functions are suitable for testing new specimen which are unknown up to this point. They are also very useful in the

(software) engineering process regarding both, the modification and validation of evaluation methods and their physical accordance on the one hand and the software developing process (especially for the investigation of borderline cases for result values) on the other hand.

The image processing techniques proofed their principal operational capability. To provide reliable results in terms of an industrial application, those methods need to be further enhanced and adjusted. Nevertheless, it can be shown that such features are able to automatically find and determine defects in the result data from the evaluations. They could provide a summary of all defects such as number of defects, depth and size of every defect. This is an important step to a future, fully automated testing rig, because those outputs can be used to classify a test object as OK or NOT-OK.

8.2 Potential

The PPT seems to be able to gain significant and reliable information from a measurement within a very short time interval. Although not treated in this work, the phase shift which can be obtained by the PPT is adequate for defect depth determination, as literature ([14]) suggests.

The presented DOP evaluation represents a promising basis for future applications. It provides numerous possibilities to adapt it to specific applications.

The compactness of the components offers the possibility to create mobile testing rigs. Such a mobile platform could be useful in the aerospace industry, since modern air planes consist of a lot of CFRP elements which can not easily be dissembled and tested in a laboratory. A mobile testing rig could provide the possibility to screen such elements directly on the air plane.

Finally, the output of this thesis allows to conclude, that a flash thermographic testing rig should be able to perform in-line testing when integrated into a production line. Through this, a hundred percent component inspection, which is reliable, fast and cheap, is realizable.

Glossary

t_{Flash} The point in time when the energy emitted from the flash light can be observed by the IR-camera as intensity peak

t_{EoF} The point in time when the saturation of the IR-camera sensor due to the flash light thoroughly died away

t_{max} The point in time when the temperature of the rear surface of the specimen reaches its maximum after a flash light stimulation in transmission mode

$t_{1/2}$ The point in time when the temperature of the rear surface of the specimen reaches $T_{1/2}$ in transmission mode

t_w The point in time when the slope of the temperature of the front surface of the specimen and T_{end} intersect (in reflection mode)

T_{max} The maximum temperature of the rear surface of the specimen after a flash light stimulation in transmission mode. This temperature is equal to T_{end}

T_{end} The end temperature of the front surface of the specimen after a flash light stimulation in reflection mode. This temperature is equal to T_{max}

T_0 Initial surface temperature of the specimen before the flash stimulation

$T_{1/2}$ The temperature which represents half of the temperature increase of the rear surface of the specimen from T_0 to T_{max} in transmission mode

k_{EoF} Limit of the gradient of the temperature profile in reflection mode which defines t_{EoF}

n_{poly} Degree of the polynomial fitted to the data of measurements in reflection mode

n_{BF} Number of the polynomials in the basis functions of the DOP evaluation

x_{Frames} Vector with all time stamps of the frames within the recorded data of a measurement in reflection mode in logarithmic scale (and therefore all values on the x-axis of a temperature profile)

n_{Frames} Number of frames within a record

n_{std} Multiplier of the standard deviation, which is used in the limit definition to distinguish flawless material from defects in the DOP evaluation

$n_{min,FL}$ Minimum degree of a polynomial to approximate a temperature profile of flawless material

$n_{min,DF}$ Minimum degree of a polynomial to approximate a temperature profile of a defect

n_{FL} Actually chosen degree of a polynomial to approximate a temperature profile of flawless material

n_{DF} Actually chosen degree of a polynomial to approximate a temperature profile of a defect

PLA Polylactic Acid - Material used in 3D printers

DOP Discrete Orthogonal Polynomials

IR Infrared

UV Ultra Violet

GUI Graphical User Interface

PLC Programmable Logic Controller

OPC Open Platform Communications

PPT Pulsed Phase Thermography

TSR Thermographic Signal Reconstruction

$CFRP$ Carbon Fiber Reinforced Plastic

$PTFE$ Polytetrafluorethylen

US Ultrasonic

FPA Focal Plane Arrays

NUC Non-Uniformity Correction

$GigE$ Gigabit Ethernet, data connection between PC/PLC and PC/camera

RAM Random-Access Memory, main memory of the PC

HDD Hard Disk Drive, main data storage of the PC

List of Figures

List of Tables

Bibliography

[1] Oswald-Tranta B. *Automated Thermographic Non-destructive Testing*. Habilitation, Montanuniversität Leoben, 2012.

[2] Oswald-Tranta B. *Infrarot Thermographie*. Montanuniversität Leoben, Lecture Script, 2013.

[3] Oswald-Tranta B. *Automatic Surface Inspection*. Montanuniversität Leoben, Lecture Script, 2015.

[4] Oswald-Tranta B. and Shepard S. M. Comparison of pulse phase and thermographic signal reconstruction processing methods. In *SPIE Defense, Security, and Sensing*, pages 87050S–87050S. International Society for Optics and Photonics, 2013.

[5] Oswald-Tranta B., Maier A., and Schledjewski R. Defect depth determination in a CFRP structure using TSR technique. In *Proceedings of the 12th Conference on Quantitative InfraRed Thermography*, 2014.

[6] Oswald-Tranta B., Schmidt R., and Grandl T. Comparison of flat bottom holes and hidden inclusions using flash thermography. *Quantitative InfraRed Thermography Journal*, 2016. Submitted: Nov, 2016.

[7] Russ J. C. *The Image Processing Handbook*. CRC Press, Inc., 2000 Corporate Blvd., N.W., Boca Raton, Florida 33431, USA, second edition, 1994. ISBN 0-8493-2516-1.

[8] Gaussorgues G. *Infrared Thermography*. Chapman & Hall, third edition, 1994. ISBN 0-412-47900-1.

[9] Mayr G., Plank B., Gruber J., Sekelja J., and Hendorfer G. Thermal diffusivity measurements of porous CFRP specimens with different number of plies using pulsed thermography in transmission and reflection mode. In *12th International Conference on Quantitative InfraRed Thermography (QIRT 2014), Bordeaux, France*, 2014.

[10] Wróbel G., Pawlak S., and Mzuia G. Thermal diffusivity measurements of selected fiber reinforced polymer composites using heat pulse method. *International Science Journal*, 48:25–32, March 2011.

[11] TWI Global. Radiography testing. `http://www.twi-global.com/capabilities/integrity-management/non-destructive-testing/ndt-techniques/radiography-testing/`. Accessed: 2016-04-04.

[12] BÖHLER Edelstahl GmbH. Special steel manual. Document Number: AL 005 E - 01.2006 - 2.000 CD.

[13] Vogel H. *Gerthsen Physik*. Springer-Verlag Berlin Heidelberg, eigtheenth edition, 1995. ISBN 3-540-59278-4.

[14] Castanedo C. I. *Quantitative Subsurface Defect Evaluation by Pulsed Phase Thermography: Depth Retrieval with the Phase*. PhD thesis, Faculté des Sciences Et De Génie Université Laval Québec, October 2005.

[15] FLIR Systems Inc. Flir Titanium Datasheet, 2009. Document Number: I010909PL.

[16] Fraden J. *Handbook of Modern Sensors*. Springer Science+Business Media, 233 Springer Street, New York, NY 10013, USA, fourth edition, 2010. ISBN 978-1-4419-6465-6.

[17] Krautkrämer J. and Krautkrämer H. *Ultrasonic Testing of Materials*. Springer-Verlag Berlin Heidelberg GmbH, fourth edition, 1990. ISBN 978-3-662-10682-2.

[18] Parker W. J., Jenkins R. J., Butler C. P., and Abbott G. L. Flash method of determining thermal diffusivity, heat capacity, and thermal conductivity. *Journal of Applied Physics*, 32(9), September 1961.

[19] Meyberg K. and Vachenauer P. *Höhere Mathematik 2*. Springer-Verlag, Mathematisches Institut der Technischen Universität München, Arcisttrasse 21, W-8000 München 2, FRG, first edition, 1991. ISBN 3-540-52334-0.

[20] Trhlíková L., Zmeskal O., Psencik P., and Florian P. Study of the thermal properties of filaments for 3d printing. In *AIP Conference Proceedings*, volume 1752. AIP Publishing, 2016.

[21] Harker M. *Machine Vision*. Montanuniversität Leoben, Lecture Script, 2014.

[22] Neitzel M., Mitschnag P., and Breuer U. *Handbuch Verbundwerkstoffe - Werkstoffe, Verarbeitung, Anwendung*. Carl Hanser Verlag, München, second edition, 2014. ISBN 978-3-446-43696-1.

[23] Shepard S. M. Temporal noise reduction, compression and analysis of thermographic image data sequences, February 2003. US Patent 6,516,084.

[24] Shepard S. M. and Lhota J. R. Flash duration and timing effects in thermographic NDT. In *Defense and Security*, pages 352–358. International Society for Optics and Photonics, 2005.

[25] Shepard S. M. and Young T. Method and apparatus for thermographic imaging using flash pulse truncation, 2005. US Patent 7186981 B2.

[26] Shepard S. M., Lhota J. R., Rubadeux B. A., Wang D., and Ahmed T. Reconstruction and enhancement of active thermographic image sequences. *Optical Engineering*, 42(5): 1337–1342, 2003.

[27] Sonka M., Hlavac V., and Boyle R. *Image Processing, Analysis, and Machine Vision*. PWS Publishing, Pacific Grove, California 93950, USA, second edition, 1999. ISBN 0-534-95393-X.

[28] Thermitus M.-A. and Laurent M. New logarithmic technique in the flash method. *International Journal of Heat and Mass Transfer*, 40(17):4183–4190, 1997.

[29] Trinity NDT. Radiographic testing (rt). `http://www.trinityndt.com/services_rt.php`. Accessed: 2016-04-04.

[30] O'Leary P. and Harker M. An algebraic framework for discrete basis functions in computer vision. *Sixth Indian Conference on Computer Vision, Graphics and Image Processing*, pages 150–157, 2008.

[31] O'Leary P. and Harker M. A framework for the evaluation of inclinometer data in the measurement of structures. *IEEE Transactions on Instrumentation and Measurement*, 61(5):1237–1251, May 2012. ISSN 0018-9456. doi: 10.1109/TIM.2011.2180969.

[32] O'Leary P., Harker M., Schmidt R., and Ritt R. *Data Science for Mechnical Engineers*. Montanuniversität Leoben, Lecture Script, 2016.

[33] Joven R., Das R., Ahmed A., Roozbehjavan P., and Minaie B. Thermal properties of carbon fiber-epoxy composites with different fabric weaves. *SAMPE, Charleston, SC*, 2012.

[34] Schmidt R. *Automatisierte thermographische Rissprüfung bei komplexer Bauteilgeometrie*. Montanuniversität Leoben, Diploma Thesis, 2014.

[35] Carslaw H. S. and Jaeger J. C. *Conduction of Heat in Solids*. Oxford University Press, second edition, 1946. ISBN 0-19-853368-3.

[36] Angioni S.L., Ciampa F., Pinto F., Scarselli G., Almond D.P., and Meo M. An analytical model for defect depth estimation using pulsed thermography. *Experimental Mechanics*, 56:1111–1122, 2016.

[37] Elinchrom Elinca Sa Switzerland. The Elinchrom System, Power by Elinca. Data Sheet.

[38] Maldague X. P. V. *Theory and Practice of Infrared Thechnology for Nondestructive Testing.* John Wiley & Sons, Inc., first edition, 2001. ISBN 0-471-18190-0.

[39] MATLAB version 8.4.0 (R2014b). *Software Documentation.* The MathWorks Inc., Natick, Massachusetts, 2014.